PhD-FSTM-2021-045
The Faculty of Science, Technology and Medicine

DISSERTATION

Defence held on 14/07/2021 in Luxembourg

to obtain the degree of

DOCTEUR DE L'UNIVERSITÉ DU LUXEMBOURG

EN SCIENCES DE L'INGÉNIEUR

by

Adham AL-SAYYAD
Born on 21 December 1989 in Gharbeya (Egypt)

LASER WELDING OF METALS TO POLYMERS UNDER THE SPECIAL INFLUENCE OF SURFACE PRETREATMENT ON INTERFACIAL THERMAL TRANSFER

Dissertation defence committee

Dr Peter Plapper, dissertation supervisor
Professor, Université du Luxembourg

Dr Laurent Houssiau
Professor, Université de Namur

Dr Slawomir Kedziora, Chairman
Professor, Université du Luxembourg

Dr Jean Pierre Bergmann
Professor, Technische Universität Ilmenau

Dr Manfred Greger, Vice Chairman
Professor, Université du Luxembourg

Acknowledgement

Although a PhD title is a prestigious reward, I am fortunate to be granted with much more throughout the journey to earn it. This work is based on the contribution of many. First, I would like to express my sincere appreciation to my dear wife, Nirmeen Sallam, and our dear son, Awab, for the sacrifices they made and the support they provided to make this possible. I would also like to thank my mother, Hamida Donia, father, Ayman Al-Sayyad, and Nany, Zeinab Mohamed, for raising me to become capable, for encouraging me to achieve, and for the sacrifices they made to make this happen. In addition, many thanks to my elder sisters, Salma and Yasmine, and to my friends and mentors from all around the world for always being there to advice and support.

This work is in the framework of LaserSTAMP project which involves several European partners, those are: University of Luxembourg (UL) and Luxembourg Institute of Science and Technology (LIST) in Luxembourg, University of Namur (UNamur) and Optec laser systems in Belgium.

Indeed, special thanks to my doctoral father, Prof. Peter Plapper, for the opportunities he provided for me to grow, for the trust and liberty he gave me to manage the project, and for providing me with all the required tools and support to guarantee the project's success. His mentorship has been enriching on many personal, professional and academic levels. I would also like to thank my CET committee members, Prof. Manfred Greger, and Prof. Slawomir Kedziora, for their guidance throughout my PhD. This work is also based on the M.Sc. thesis work of several students. In this regard, I would like to thank Kevin Santos, Prashant Lama, and Farah Salah, for their dedication and hard work. Moreover, I am grateful to the support of all my colleagues at UL, from our research group, research laboratories, technical support, manufacturing workshop, and administration.

In addition to plasma pretreatments, sessile drop tests, SEM, EDX, LFA, and surface topography analysis were performed at LIST. For that, I would like to thank our colleagues at LIST, and to express my sincere appreciation to Mr. Julien Bardon for his dedication, coordination efforts, and very valuable contribution to this work. It was a great learning opportunity to work closely with a scientist like him, who is not only of high level of knowledge and skills, but also of generosity, morality and ethics. XPS analysis was performed at UNamur. In this regard, I would like to thank our colleagues at UNamur, specially Prof. Laurent Houssiau for his mentorship, and Dr. Pierre Hirchenhahn for his support in the analysis and his contribution to this work. I would also like to thank our colleagues at Optec laser systems and our partner, Mr. Alain Biernaux, for providing industrial insights, ensuring market validation, and demonstrating the developed technology by building a hybrid laser pretreatment and welding machine tailored for metal – polymer joining.

Last but not least, I would like to thank FNR in Luxembourg and DGO6 in Belgium for financially supporting the LaserSTAMP project.

Abstract

Joining of metals to polymers is increasing among various industries because of its ability to produce lightweight hybrid products with tailored properties. Common joining methods, such as adhesive bonding and mechanical fastening, require adding a third material which might involve hazardous chemicals or add extra weight and stress concentration points to the component. On the other hand, Laser-Assisted Metal – Polymer joining (LAMP) is a contactless, rapid, highly precise and energy-efficient technique, that produces autogenous and miniaturized joints. It was already demonstrated that surface pretreatment prior to the welding process has a significant impact on the joint performance by modifying surface chemistry and topography, promoting chemical bonding and mechanical interlocking. This research aims at expanding the understanding of the effects of surface properties on the joint's performance by investigating their influence on interfacial thermal transfer.

While increased surface roughness of metallic partner is expected to improve LAMP joint performance by promoting mechanical interlocking, it is hypothesized that a smoother surface would improve the joint quality by enhancing the interfacial thermal transfer during the welding process, resulting in a larger area of molten polymer at the interface and a better joint performance.

In this research, aluminum (Al1050) and titanium (Ti64) were joined with polyamide (PA6.6). Initially, laser welding parameters were optimized and kept constant during all surface pretreatments' investigations. Preliminary surface pretreatments, using short-pulsed laser ablation and atmospheric plasma pretreatment, were conducted on Al1050 – PA6.6 to analyze the effects of surface composition and topography on joint quality and performance, and to optimize interfacial adhesion. Results show a correlation between increased surface oxidation and surface energy with improved interfacial adhesion and joint resistance to shear failure. Compared to plasma pretreated surfaces, laser ablation of metals results in a very rough surface which exhibits perfect wettability to both water and diiodomethane. This promotes mechanical interlocking and interfacial adhesion, resulting in a relatively stronger joint failing in a cohesive failure mode. Results confirm that an improvement of the assembly's shear resistance to failure can certainly be achieved without an increase in surface roughness and interfacial interlocking, as observed in case of plasma pretreatment.

Design of Experiments (DoE) techniques were utilized for both material combinations in order to optimize laser ablation process and to investigate the effects of pretreatment parameters on surface properties, interfacial thermal transfer, joint quality and resistance to failure. Laser ablation parameters influenced the surface topography with no significant effect on the surface composition, and all laser-ablated surfaces showed perfect wettability to both water and diiodomethane. While all ablated surfaces demonstrate cohesive failure mode, smoother ablated surfaces results in a better interfacial thermal transfer as indicated by the Thermal Contact Resistance (TCR) calculations and measurements, based on Cooper–Mikic–Yovanovich (CMY) model and layered Laser Flash Analysis (LFA) investigations, respectively. Results show that a smoother ablated surface results in better interfacial thermal transfer, melting a larger area of polymer which increases the joint quality and resistance to shear load.

Table of Contents

Chapter 1

1. Introduction

This chapter introduces the significance of the addressed research topic, and its related challenges. It illustrates the importance of joining metals to polymers, with a focus on the material combinations used in this study. It summarizes the methods used to join metals to polymers, and highlights the appeal of laser welding process.

1.1. Motivation

Environmental protection and climate change have become major concerns particularly in the last few decades. As technological advancements grow, new requirements for engineered materials, products, and processes that are reliable, robust, sustainable and environmentally friendly arise. In a dynamic globalized economy, transportation of goods and individuals have become more rapid. From economic and environmental aspects, reducing the weight of vehicles and/or products would certainly have its positive impact on the energy efficiency of the transportation procedure, and the reduction of greenhouse gas emissions.

The joining of dissimilar materials with complementary properties, like metals and polymers, provide noteworthy potential for innovation in many industries. On one side, metals have a high strength-toughness ratio along with high thermal and/or electrical conductivity. On the other side, polymers commonly have lower densities, higher chemical resistance, deformability, and relatively low cost, compared to metals. Combining such distinct material properties allows for weight reduction, and to create customized products with tailored properties. This improves fuel efficiency in transportation industries, and opens new areas of development, such as in biomedical applications, where the elasticity of polymers and toughness of metals can be integrated to resemble biological characteristics.

1.2. Applications

Automotive industry

The implementation of hybrid, lightweight, engineered materials in transportation vehicles provides a reliable approach to increase fuel efficiency while keeping robust and intact structures. This has increased the demand of automotive industry on joining dissimilar materials [1]. A recent study [2] shows that a mix of materials is needed to provide an optimal lightweight vehicle at a minimal cost. Table 1 shows the mass reduction potential of optimized designs using different material strategies. Multi-material designs approach is considered to reach an optimal design at a minimal cost. Using multiple materials does not only provide high potential in reducing the vehicle weight, it also takes advantage of the best properties of materials in use.

Table 1: mass reduction potential of various vehicle material design strategies [2]

Design strategy	Mass reduction
Multi-Material	30 – 60%
Carbon Fiber-Intensive	40 – 60%
Aluminum-Intensive	30 – 45%
Steel-Intensive	15 – 40%

Utilizing metal-polymer assemblies in automotive industries has expanded to reach several body parts, ranging from front-end structures to seating and more. By adopting injection-molding technology, plastic ribbing and bracing are molded onto the metal parts. These plastic structures not only enhance the capacity of the metal construction through optimal transmission and distribution of the forces in the component, but also reduce the overall weight and cost of the component. As an example, company LANXESS has implemented such technology in the front-end construction of the Ford Focus as shown in Figure 1, yielding 20 % part costs reduction, 50 % investment cost reduction, and 40 % weight reduction [3]. Other parts of the vehicle, such as cross-car beams and spare wheel well, have also adopted metal-polymer hybrid structures to help reduce the overall weight and cost of products. The growth in electric mobility market led to innovations in utilizing hybrid metal-polymer joints. This is clearly demonstrated in the ONSERT multipurpose joining system, shown in Figure 1, which is developed by DELO and Böllhoff and implemented in the BMW i3 and BMW i8 vehicles.

Joining aluminum to polyamide is of high industrial relevance to automotive industries. While aluminum accounts for second only to steel as the most used material in vehicles, the use of thermoplastics has grown significantly over the last 25 years in automotive industry. Due to its oil resistance, thermal stability, mechanical strength and toughness, polyamide has been used for under-the-hood applications, including air intake manifolds, rocket covers, fuel rails, radiator end tanks and electrical connections. Hybrid aluminum – polyamide assemblies can be found in automobile parts such as heat exchangers. However, they are currently being joined with either injection molding or adhesive bonding which requires relatively big flange size and long curing time respectively.

Figure 1: (left) Ford Focus front-end plastic-metal hybrid construction developed by LANXESS [3]*; (right) ONSERT bolt applied in BMW i3* [4]

Aerospace industry

For the aerospace sector, efforts in reducing the weight of the aircraft and manufacturing cost by replacing metallic structural materials with polymers and/or reinforced polymer composites have been ongoing since more than forty years. Bell helicopters (Dallas Fort Worth, USA) have been using composites since the 1980s allowing them to achieve a 20% reduction in weight on metallic airframes. A 2005 study [5] reported that the aerospace market accounts for 20% of carbon fiber reinforced polymer production.

Joining titanium alloy (Ti64) to polyamide (PA6.6) is of high relevance to aerospace industries. More than half of titanium production is being used in the aerospace sector [6]. Because of its high strength-to-weight ratio, Ti64 is used for engine parts and airframe structures applications such as bolts, wing box, cockpit window frame, and seat rails [7]. Polyamide (PA6.6) matrix is commonly used in fiber reinforced composites in aerospace industries [8]. It is used in compartments, exterior applications, and assembly components due to its sealing and vibration damping properties. Figure 2 shows an example of hybrid components in Boeing 787. Developing a robust and rapid joining process for joining metals to polymers will enhance design flexibility in aerospace industries.

Figure 2: examples of materials used in Boeing 787 [9].

Biomedical industry

Hybrid metal-polymer components are utilized to create assemblies with tailored properties. The use of metal-polymer hybrid assemblies in biomedical implants has gained attention for their ability to combine the polymer's modulus of elasticity and density, which are close to the cartilage bone composite, with the high compression and tensile strength of metals. This provides valuable damping for the transmission of shock forces.

The high strength-to-weight ratio of some polymers makes them especially attractive as a material for the socket half of the implant's joint [10]. The socket shape can be easily molded or machined at a low cost when made out of polymeric material. However, the chosen polymer should have sufficient wear and creep resistance for a lifetime of cyclic loading and sliding. The chosen material must be biologically compatible, and the joint components should not degrade to prevent possible health risks.

Both Ti64 and PA6.6 are biocompatible and are widely used for biomedical implants replacing failed hard tissue. Examples of Ti64 applications include artificial hip and knee joints, bone plates and screws for fracture fixation, cardiac valve prostheses, and

pacemakers [11]. Ti64 is also commonly used in dentistry devices such as implants, crowns, bridges, overdentures, and dental implant prosthesis components [12]. On the other hand, PA6.6 have been reported promising for denture base materials of dental implants [13]. It is also being used in tracheal tubes, pacemakers, gastrointestinal segments, and facial prostheses [14]. Figure 3 shows some biomedical applications of both titanium and polyamide.

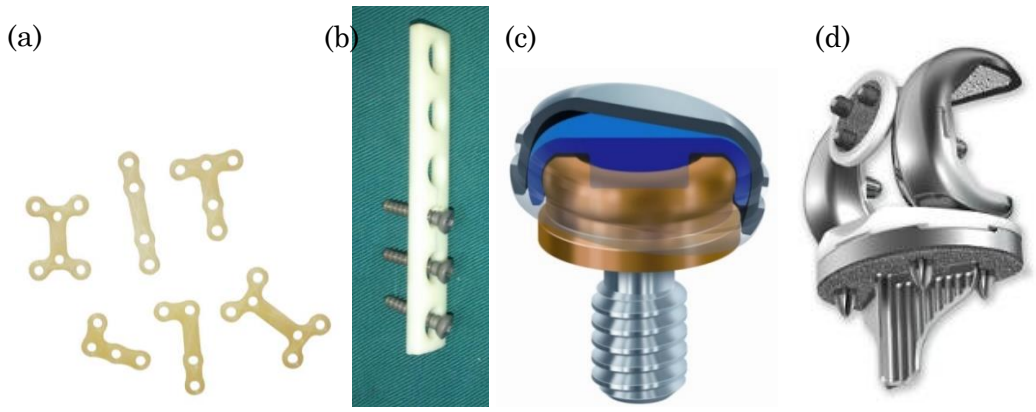

Figure 3: examples of polyamide and titanium use in biomedical applications. (a) polyamide implants [15]*; (b) polyamide based composite bone plate and titanium screws* [16]*; (c) polyamide denture caps on titanium implant* [17]*; (d) titanium knee implant* [18]

1.3. Joining methods

Nowadays, metals and polymers are mostly joined either by adhesive bonding, injection-molding, or mechanical fastening [19]–[22]. However, adhesive bonding generally requires extra curing time and includes some health hazards, injection-molding requires large flange size, and mechanical fastening adds extra weight, geometrical constraints, and stress concentration points to the assembly. This limits the design flexibility and weight reduction capabilities, and hinders the applicability of such joining methods for certain industries such as the biomedical sector. Other techniques are also being exploited, such as plastic injection over molding in metallic perforated parts and hybrid joining methods (combining adhesive bonding with mechanical fastening or welding) [23], [24]. Figure 4 illustrates different joining methods used for metal-polymer assemblies, and Table 2 illustrates the limitations of welding techniques and highlights the significance of laser welding process.

Thermal joining of metals to polymers is challenging because of the significant difference of the thermal properties and melting temperatures of both materials [25]. This process can be performed by different energy sources such as laser irradiation, resistance heating, or friction joining [26]–[29]. However, focused laser beam energy provides a non-contact thermal joining solution for joining metals to polymers by allowing a finely controlled energy introduction into the materials, yielding a high-temperature gradient in a limited volume. This precise control over the heat input provides the opportunity to create miniaturized joints by thoroughly melting the polymer at the interface of the joint while, at the same time, avoiding its degradation. This encouraged several research groups to investigate Laser-Assisted Metal to Polymer (LAMP) joining.

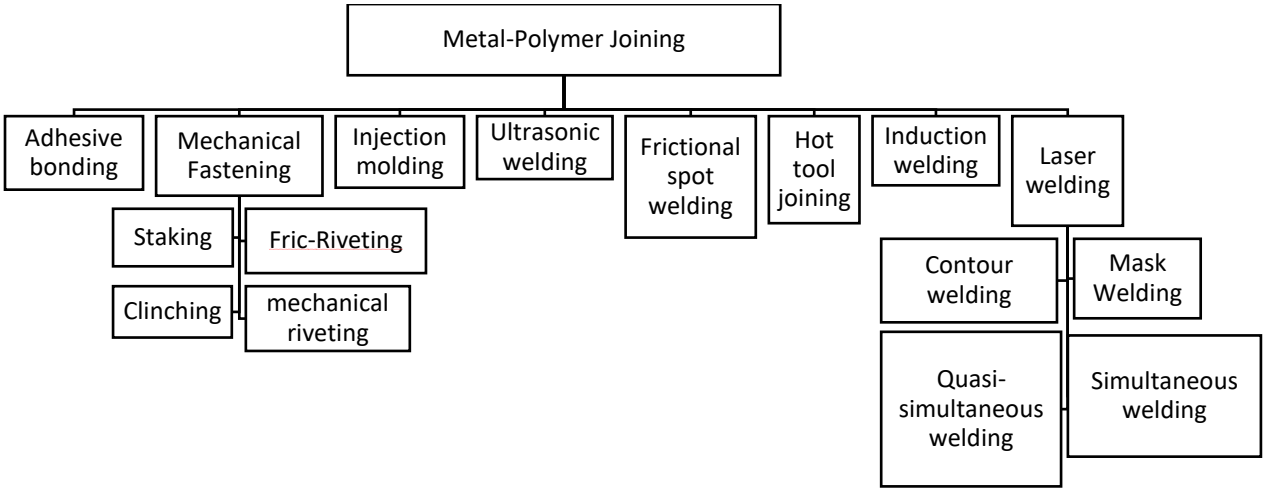

Figure 4: examples of methods used for joining metal-polymer joint

Table 2: drawbacks of metal-polymer joining techniques

Joining technique	Limitations and drawbacks
Adhesive bonding	Environmental hazards Biocompatibility challenges Required curing time Large bonded area
Mechanical fastening	Additional joint weight and cost Not leak-tight Stress concentration points
Injection molding	Geometrical constraints Wide flange Suitable only for mass production
Conventional welding	Not applicable due to differences in melting and decomposition temperatures of materials to be joined
Ultrasonic welding	Contact between tool and work piece is required Results in indentation on the joint Localized welding Process
Frictional spot joining	Contact between tool and work piece is required Suitable only for ductile metal – polymer joints Results in indentation on the joint Localized welding Process
Hot tool joining	Difficult to industrialize Requires relatively long heating time
Induction welding	Wide flange High set-up efforts
Laser welding	Large initial investment Technology under development

Chapter 2

2. State of the art

This chapter reviews relevant state-of-the-art literature on laser welding of metals to polymers, presents the adhesion mechanisms, and discusses several surface pre-treatment methods used to promote adhesion and improve joint performance. It outlines effects of surface roughness on mechanical interlocking and interfacial thermal transfer, and illustrates relevant Design of Experiments methods.

2.1. Laser welding of metals to polymers

Laser, an acronym for Light Amplification by Stimulated Emission of Radiation, is a coherent, convergent and monochromatic beam of electromagnetic radiation. The wavelength of a laser can range from ultra-violet to infrared. Lasers can deliver a wide range of focused power (~mW to 100kW) with a precise spot size, and a pulse duration that can reach to as low as femtoseconds, on any kind of substrate through any medium [30]. Because of its unique coherence property, spectral purity and ability to propagate in a straight line, lasers have been involved in a variety of applications ranging from bar code scanning and printing devices to biomedical, manufacturing, and military applications [30].

Lasers have been used in welding a variety of material combinations up to several thicknesses with different joint configurations [31]–[35]. The choice of laser source and welding parameters depends on several factors including type and thickness of materials to be joined, welding configuration, desired joint properties, etc. LAMP joining is an innovative technology which utilizes the precession and high-power density of the laser beam to create miniaturized joints without causing the polymer to degrade.

The process of LAMP generally consists of two variations as shown in Figure 5, one of which is laser transmission welding, and the other is direct laser welding [36]. Laser transmission joining can be used for joining laser-transparent polymers with metals, where a laser beam has to be carefully selected with a wavelength that would not be absorbed by the chosen polymer. In this process, the laser beam is passed through the polymer and is absorbed by the metallic joining partner, leading to an increase in temperature at the interface between plastic and metal, consequently causing the polymer to melt and bond to the metallic surface. However, in most cases, industrially applicable polymers include additives and colorants making it difficult to find a polymer that is completely transparent to a laser beam. This partial transparency causes absorption, reflection, and scattering of laser beam, decreasing the process control and limiting the process to low thicknesses of the chosen polymer.

In the case of direct laser welding, the laser beam is irradiated directly on the metallic joining partner. The introduced heat is then conducted through the metal plate which leads to melting the polymer at the joint interface. There are two fundamental laser welding modes which depend on the power density and its interaction with the irradiated surface. Those are conduction welding, and key hole welding. In conduction welding, the laser parameters are set so that the vaporization of the workpiece is minimal [37]. This mode occurs with a defocused beam at a relatively low power density. In an overlap

configuration, the laser beam is first targeted on the surface causing a small surface area to be heated, sometimes above the melting point and forming a melt pool. Then, the generated heat at the metal surface is transferred by conduction to the joint interface. The resulting molten pool is relatively wide and shallow, with a wider heat-affected zone, compared to that produced by keyhole welding. In deep penetration or keyhole welding, laser parameters are set to introduce sufficient energy density to the material resulting in boiling in the melt pool and the formation of a column of vapor with a diameter of approximately the size of the focused laser beam. This 'keyhole' behaves like an optical black body subjecting the laser radiation which enters the hole to multiple reflections before being able to exit. An increase in the applied laser irradiance above 10^6 W/cm^2 causes the transition from conduction mode to deep penetration mode [30].

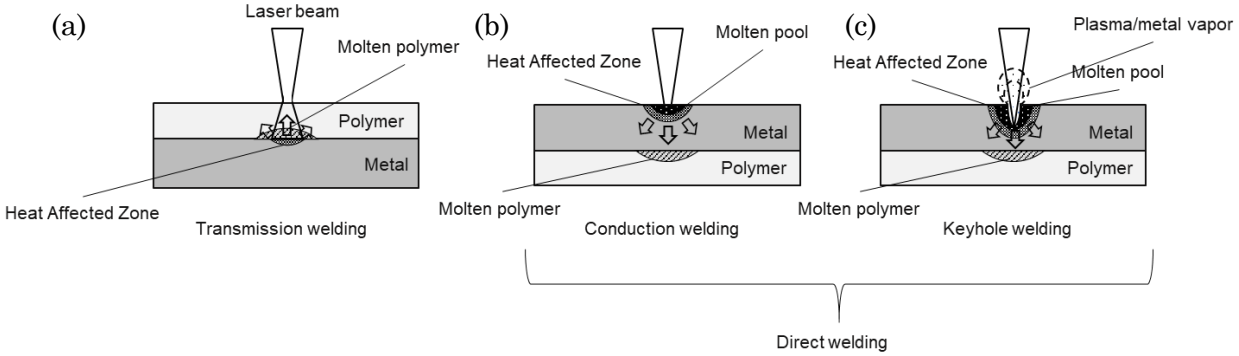

Figure 5: variations of LAMP; (a) transmission welding; (b) conduction welding; (c) keyhole welding; (b, c) direct welding

2.1.1. Welding parameters

LAMP process can be categorized into three interdependent stages which influence joint properties and performance, those are laser beam material interaction, interfacial thermal transfer, and polymers' melting thermodynamics. Careful consideration of process parameters such as laser power, beam guidance speed, focal position, pulsing mode, shielding gas type and flow-rate, etc., is essential to guarantee the success of the laser welding process [38]–[41]. Because of its complexity, researchers [42], [43] utilized statistical Design of Experiments (DoE) in order to simplify the laser welding process and understand effects of parameters on joint properties. DoE, and its use in LAMP, is further elaborated in §2.6.

Laser systems are flexible in terms of adjusting power density and total energy delivered to a workpiece. Depth of penetration is considered as a key parameter in keyhole laser welding. Different combinations of welding parameters, such as power and beam guidance speed, can produce the same depth of penetration and keyhole morphology, making the parameters selection complicated. However, it is not clear which laser parameter determines the depth of penetration despite several research efforts investigating absorption conditions, melt flow, and keyhole formation [44]–[51].

In order to simplify laser processing parameters, Steen [52] and Ion [53] describe parametric conditions required to achieve a principal thermal mechanism of Continuous Wave (CW) laser processing. Several investigations [54]–[57] show that power density and interaction time are the most significant factors in various laser processing techniques. However, Suder and Williams [58] show that power density and interaction time are not sufficient to characterize the laser welding process. Thus, they introduced the specific point energy parameter, which corresponds to the product of laser output power and

interaction time. They showed that the depth of penetration is mainly controlled by the power density and specific point energy, while the weld width is controlled by the interaction time.

Considering LAMP, researchers have been working to understand the influence of laser processing parameters on the joint properties and performance. Bergmann and Stambke [36] investigated effects of laser power in both transmission and direct joining setups on the joint properties and performance. Results indicate that increasing laser power leads to a wider joint seam and better wetting of molten polymer on a metal surface, resulting in a stronger joint. However, extensive increase in laser power leads to the formation of pores indicating degradation of polymer at the interface. Lambiase and Genna [59] investigated effects of laser power and energy on performance of laser textured aluminum – PEEK joints. Similarly, increasing welding energy enlarged the joint area with consequent increase in joint's resistance to failure. However, such increase in thermal energy caused degradation of PEEK at the interface and the formation of bubbles. Wang et al. [60] concluded the same when investigating laser transmission joining of PET and titanium for biomedical applications.

Schricker et al. [61] studied time- and temperature-dependent penetration of surface structures in laser welding, indicating penetration of surface structures as an important parameter for achieving high joint strength. Results excluded joining time to be an influencing factor. In a separate study [62], researchers examined the sensitivity of polymer's melting layer to process parameters, material properties and geometric attributes using experimental and numerical methods. Results show a strong influence of increased energy input and absorbed beam power on increasing melting layer thickness, and a large effect of metal sheet thickness on thermal efficiency in heat conduction joining.

Weld quality is a critical feature that limits robustness of welded joint. Weld defects, such as lack of fusion, blow-out holes, pores, cracks or undercuts are well investigated in laser welding of metal-metal joints [63]. However, weld defects in LAMP are poorly investigated, and formation of bubbles at the interface is solely acknowledged in literature [26], [41], [64], [65]. The influence of bubble formation on joint quality and performance remains debatable. Katayama et al. [26] and Tamrin et al. [41] claim that bubbles formation is essential for improved joint performance as it generates pressure pushing the molten polymer towards the metallic partner resulting in an increase in bonding strength. However, researchers [64], [65] identified the formation of bubbles as a weld defect that can strongly deteriorate joint quality and performance.

Given the hygroscopic nature of some polymers, Lamberti and Plapper [65] studied the influence of moisture content in polyamide (PA6.6) on the stability of joining process. Results show a strong effect of moisture content on the stability of the laser joining process and resulted joint quality. Humidity inside the polymer evaporates during laser welding process, creating gas with high pressure and possibly leading to a hollow gas channel along the weld line. This can cause the metal weld pool to break destroying the tight sealing. Schricker et al. [64] utilized high-speed recording to monitor evolution of bubbles during laser welding process. Three different types of bubbles were identified. A bubble can form either at the boundary layer between joining partners, at artificial nucleuses, or at gas particles resulting from vaporization of moisture inside polymer. Bubbles formed at the boundary layer adhere to the metal surface and fluctuate due to combined effects of formation, merging, and degassing processes. When the melting layer reaches an

artificial nucleus (e.g. carbon particles), bubbles are formed around the nucleus and starts to grow. Moisture based bubbles are formed randomly within the melting layer with larger size and an unsteady behavior. All bubbles travel towards the boundary layer regardless of the configuration of the joint. Thus, buoyancy force was identified not to be the primary cause of bubble movement.

2.1.2. Failure modes

Overlap welding has been by far the most studied welding configuration in LAMP. Three types of failure modes can result from such configuration as shown in Figure 6; those are (a) adhesive failure mode, (b, c) cohesive failure mode, and (d) mixed failure mode. Those failure modes have been reported both in adhesive bonding and LAMP [66]–[70]. Adhesive failure is an interfacial failure that is governed by interfacial bonding strength between joining partners. Cohesive failure occurs in the weaker joint partner and can happen at one of two regions; either at the joint zone, or in the base material far from the welded joint. Mixed failure mode is when both adhesive and cohesive failures occur simultaneously.

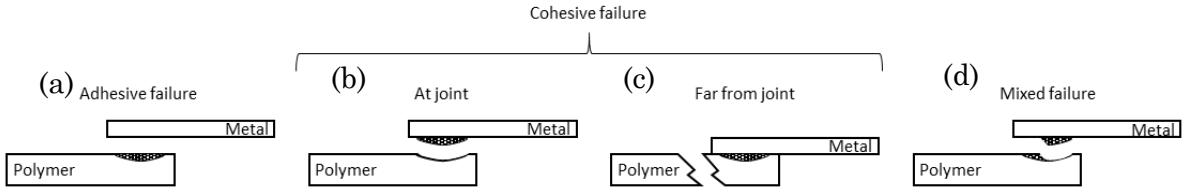

Figure 6: failure modes in LAMP; (a) adhesive failure; (b, c) cohesive failure where (b) is at joint and (c)is far from joint; (d) mixed failure

All mentioned types of failure modes have been reported in LAMP [36], [68]–[72]. While mixed failure mode indicates a mixture between cohesive and adhesive failure mechanisms, cohesive failure in base material far from welded joint indicates lower mechanical strength of joining partner compared to joint strength. Adhesive failure is governed by interfacial bonding strength which can be explained by adhesion mechanisms in §2.2. On the other hand, joint mechanical performance in cohesive failure mode is reported to correlate with changes in crystalline structure and morphology of laser welded polymers' molten zone as a result of thermal stresses [73]–[75]. Schricker et al. [76] identified four different zones at the thermoplastic's joint region as shown in Figure 7; the molten zone (1), transition area of fine microstructure (2), and heat-affected zone (3). 2a shows a partially melted or deformed area. Microstructural investigations of polymer showed no changes in its original semi-crystalline structure and no indication of amorphous layer at the boundary between joining partners. Transition area (2) illustrated fine spherulitic zone due to effects of polyamides' functional groups and resulting hydrogen bonds on nucleation during solidification. The deformation of partially molten spherulites of zone (2a) indicates effects of melt flow on polymers' morphology [77].

As shown in Figure 7, the hardness within the heat-affected zone and the melted zone was reported with an increase by 18% and 32% respectively indicating changes in polymers' microstructure/morphology [76]. XRD analysis confirmed changes in crystalline structures of PA6 weld zone [77]. Generally, peak intensities decreased moving from region 1 to 3. In the molten zone (1), results indicate an increased presence of γ-PA 6 compared to the base material. The partially molten zone (2a) shows a mixture of α- and γ-modification. In this zone, some crystallites are partially molten, others are remaining

in solid-state. In the heat affected zone (3), an increase in peak intensity compared to base material indicates secondary crystallization. Schricker et al. [75] reported cohesive failure to occur always in the heat-affected zone of the polymer material. Cohesive failure is positively influenced and joint quality increased by reducing energy per unit length during the laser welding process.

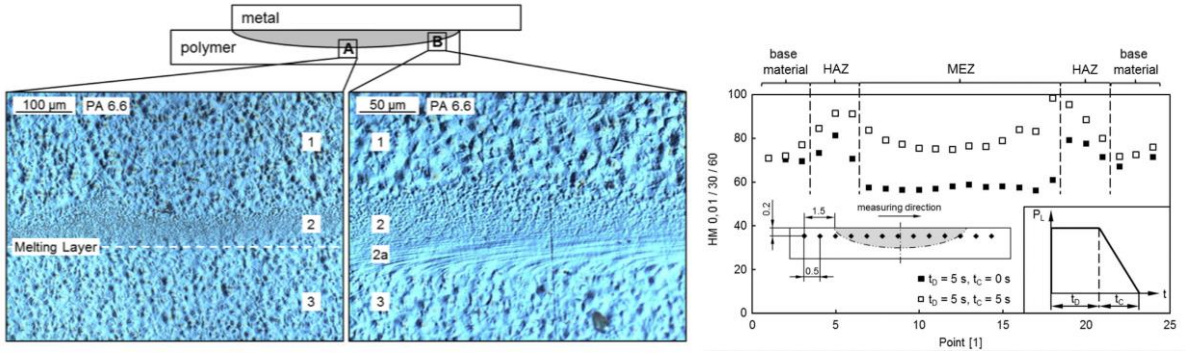

Figure 7: (left) microstructure of polymer joint area; (right) hardness profile of polymer joint area [76].

2.2. Adhesion mechanisms

Adhesion mechanisms are responsible for interfacial bonding strength between joined partners, and govern adhesive failure mode. The adhesion phenomenon is applicable to many scientific and technological fields and has become in recent years a very important field of study. In addition to adhesive bonding, adhesion theories are involved in coatings, paints, varnishes, composite materials, and LAMP. Since the final performance of these multicomponent materials depends significantly on the quality of the joint interface, a better understanding of the adhesion phenomenon is required for practical applications.

One of the main challenges in the study of adhesion mechanisms is that the subject is at the boundary of multidisciplinary scientific fields, including macromolecular science, physical chemistry of surfaces and interfaces, materials science, mechanics and micromechanics of fracture, and rheology. Thus, several theoretical models of adhesion have been proposed:

- Mechanical interlocking
- Adsorption (thermodynamic) theory
- Chemical bonding theory.
- Diffusion theory
- Electronic theory
- Weak boundary layers

The validity of those theories depends on the nature of materials in contact, in addition to the joining process and conditions. Therefore, their respective importance depends largely on the chosen system. However, the adsorption, or thermodynamic theory, exhibits the widest applicability. It describes the achievement of intimate contact and the development of physical forces at the interface, which is necessary for interlocking and chemical bonding mechanisms to occur favoring an increase in the bonding strength [78]. The energy of adhesion, which corresponds to the energy required to remove adhering partners, sums up energy of each individual theory, e.g. mechanical interlocking energy, chemical and physical bonding energy, diffusion energy, and electrostatic energy.

Regarding LAMP, researchers have been mostly focusing on the effects of mechanical interlocking and chemical bonding.

2.2.1. Mechanical interlocking

The mechanical interlocking model was proposed by MacBain and Hopkins in 1925 [79]. It claims that mechanical keying, or interlocking, of the adhesive into pores and cavities on the solid surface to be the major factor in determining adhesive strength. The enhancement of adhesion by mechanical interlocking can also be attributed to the increase in interfacial area due to surface roughness, which adds to the complexity of interactions at the interface. However, since good adhesion can be established between smooth surfaces, the theory of mechanical interlocking cannot be considered universal. Several studies investigated the effects of metallic surface pretreatment on surface roughness and mechanical interlocking in LAMP [35], [80]–[83], and are elaborated in §2.3.

2.2.2. Adsorption (thermodynamic) theory

Adsorption theory, composed of chemical and physical bonding, was the second explanation for bonding after mechanical interlocking theory and is attributed to Sharpe and Schonhorn [84]. This theory is concerned with the effect of interatomic and intermolecular forces, established at the interface between the adhesive and substrate, on the adhesion strength. The most common interfacial forces result from van der Waals and Lewis acid – base interactions. The magnitude of such forces can generally be related to fundamental thermodynamic properties, such as surface free energies of both adhesive and substrate [78]. This theory has resulted in the development of adhesive materials which have a lower surface tension as compared to the substrate surfaces, in order to ensure sufficient wetting, and acceptable bonding strength. The term wetting can be described as the phenomenon which ensures continuous contact between the adhesive and substrate surfaces. According to Young's equation (Equation 1), there is a relationship between the contact angle θ, the surface tension of the liquid σ_{lg}, the interfacial tension σ_{sl} between liquid and solid, and the surface free energy σ_{sg} (mN/m) of the solid:

$$\sigma_{sg} = \sigma_{sl} + \sigma_{lg} \cos\theta \quad \text{(1)}$$

Where:

σ_{sg}	surface free energy (mN/m)
σ_{sl}	interfacial tension (mN/m)
σ_{lg}	liquid surface tension (N/m)
θ	contact angle (°)

Generally, for the adherent to be able to wet a substrate, the adherent should have a lower surface tension than the substrate [78]. Figure 8 shows the characteristics of both good and poor wetting of an adhesive over a substrate. Good wetting is achieved when the liquid/adhesive is spread on top of the substrate surface with a relatively low contact angle, flowing into its crevices and valleys. On the other hand, a poor wetting is obtained if the liquid/adhesive bridges the gaps on substrate surface with a relatively high contact angle [85]. However, besides the sample's surface roughness, adhesive's viscosity is another important factor to consider.

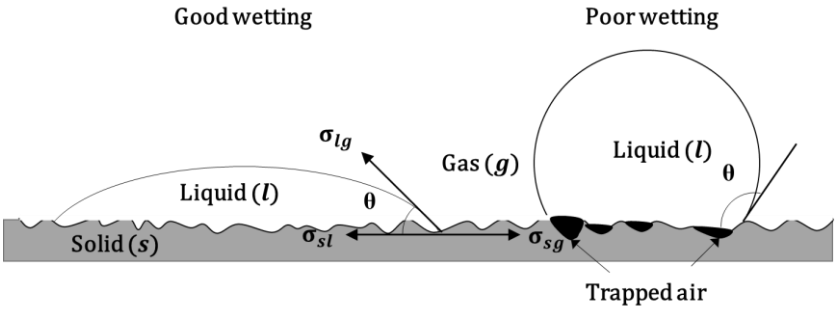

Figure 8: (left) good wetting; (right) poor wetting showing contact angle with relative surface tension components

Calculating the surface energy of a substrate has been a common way to predict the adhesion behavior particularly in adhesive bonding [78]. However, few researchers have considered the effect of surface energy on LAMP joints. Arai et al. [34], and Zhang et al. [86] reported a correlation between the increase in surface energy and enhanced LAMP joint strength. The use of surface pre-treatments, which increases the surface energy of the substrate, is required to enhance bonding quality. This is discussed in more detail in the later sections (§2.3 and §2.4) of this thesis.

2.2.3. Chemical bonding theory.

Chemical bonds formed across the adhesive–substrate interface can greatly influence the adhesion strength. These bonds, such as ionic and covalent bonds, are generally considered as primary bonds with respect to their high strength, while physical interactions, such as van der Waals, are referred to as secondary force interactions [78]. The use of adhesion promoter molecules, referred to as coupling agents, to improve the joint strength between adhesive and substrate highlights the significance of such bonding mechanism. These species are able to react chemically on both ends with the substrate and the polymer, creating a chemical bridge at the interface.

For adhesive bonding, the influence of chemical bonds on the joint strength has been analyzed in several studies. Gent and Ahagon [87], examined the effect of chemical bonding on the adhesion of polybutadiene to glass by using silane coupling agents. The authors varied the surface density of interfacial covalent bonds between the glass substrate and the cross-linked elastomer by treating the glass plates using several mixtures of vinyl terminated and ethyl terminated silanes. Both species form siloxane bonds on the glass surface. Moreover, vinylsilane can react chemically with the polybutadiene during the cross-linking treatment of this rubber where a radical reaction is involved, while the ethyl group of ethylsilane is unlikely to react with the elastomer and was used as a control. Therefore, intrinsic peel energy increased linearly with the surface concentration of vinylsilane, in good agreement with their hypothesis, proving the important effect of primary bonds on adhesive strength.

The theory of chemical bonding in LAMP has already been addressed [26], [34], [35], [60], [82]. Using X-ray photoelectron spectroscopy (XPS) and Time-of-Flight Secondary Ion Mass Spectrometry (ToF-SIMS) analysis, Katayama and Kawahito [26] were among the first to conclude that a stable metallic or covalent bond can be formed between metal and plastic. Zhang et al. [86] investigated the effect of UV grafting modification on the joining of CFRP (PA6) to A6061 using fiber laser. UV grafting introduced more active functional groups including C=O and O–C=O onto CFRP surface. Introduction of active functional groups on CFRP surface has increased the surface energy and stimulated better wetting of CFRP on the aluminum. The authors suspect that the active functional groups on the

grafted CFRP reacted with aluminum and two new kinds of chemical bonds ('Al–C' and 'Al–O–C') are formed at interface as shown in Figure 9. Lamberti et al. [88] identified hydrogen bonds between laser welded aluminum and polyamide joints, that is strongly influenced by aluminum oxide layer.

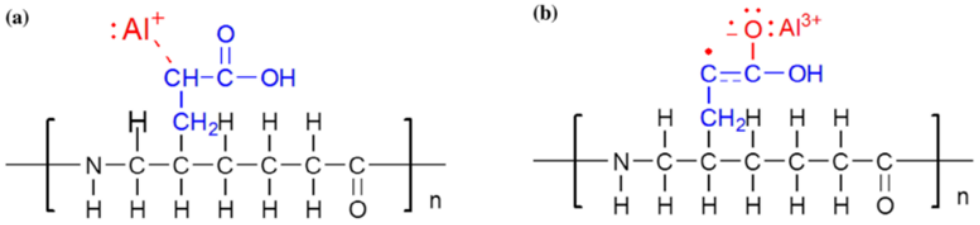

Figure 9: hypothetical bonding between grafted CFRP and A6061: (a) Al-C; (b) Al-O-C [86]

Hirchenhahn [89] used XPS and ToF-SIMS to investigate physicochemical bonding at the interface of PA6.6 laser welded to both aluminum (Al-1050) and titanium (Ti64) joints. His work defines a new methodology to access the interface of joined partners. After welding metal to polymer using direct joining in an overlap configuration, partners are peeled to reveal the fractured joint and polymeric residues on metal side. These residues are then dissolved subsequently by 2,2,2-trifluoroethanol. In the case of aluminum – polyamide joints, extremely thin polymer film was detected in the weld zone but not outside of it after polymer's dissolution, indicating strong chemical bonding between aluminum oxide and PA6.6 [90]. Different reactive sites on polyamide had been identified with potential to react with aluminum surface. Surface chemistry analysis excluded C-Al bond, marked Al-N-C insignificant, and highlighted that C-O-Al bond is formed at the interface as shown in Figure 10. These C-O-Al bonds are most likely formed by a reaction between the aluminum hydroxide groups and the polymer amide groups.

In case of laser welded titanium (Ti64) – polyamide (PA6.6), the polymer dissolution step after welding and failure was avoided and regions with adhesive failure mode was directly analyzed in Ti64 using XPS and ToF-SIMS. ToF-SIMS results conclude formation of C-O-Ti bond at the interface. Ti64 samples were spin coated with thin PA layer before welding and dissolution. Using XPS, PA6.6 was detected in higher amount inside the weld zone, indicating strong chemical bonding. High resolution spectra showed no formation of titanium carbide and titanium nitride. However, a reaction with oxygen site remained unclear. An imine bond was observed only in the weld's N 1s region. Results indicate type of bonding as shown in Figure 10. Principle Components Analysis (PCA) of the ToF-SIMS data shows that C-O-Ti bond is formed at the Interface as a result of laser welding.

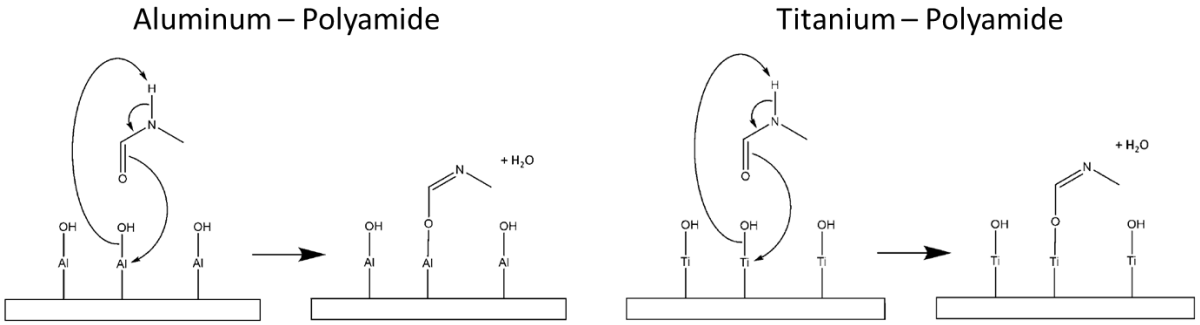

Figure 10: schematic of: (left) aluminum polyamide chemical bonding; (right) titanium - polyamide chemical bonding [89].

2.2.4. Diffusion theory

Diffusion theory was proposed in the 1960s by Voyutski and Vakula [91]. This theory is based on the assumption that the adhesion is promoted via interdiffusion of molecules between the adhesive and the substrate across the interface [78]. This theory generally requires that both the adhesive and substrate are polymeric and miscible with each other to be able to promote interdiffusion of long chain molecules.

For LAMP, Zhang et al. [92] investigated the interface of laser welded Al – PA6 assemblies using XPS. Authors concluded strong influence of chemical reaction at the interface on joint's shear strength. However, considering a rough surface, one cannot interpret the existence of diffusion between the two materials, as the coexistence of both materials at the interference plane, due to the rough surface, might be aliased with possible diffusion. To eliminate effects of roughness, Hirchenhahn [89] performed ToF-SIMS depth profiling on joint area of mirror polished aluminum after laser welding to polyamide (PA6.6). Beyond a certain depth (31 nm), depth profiling results showed lower reduction rate of polymeric ions (CNO^- and $C_2H_4NO^-$) inside the weld zone of the aluminum surface than outside the weld zone. Prior to reaching the same depth point, the intensity of metal oxide ions (Al^- and AlO_2^-) were increasing at a higher rate outside the weld zone than inside it. Results indicate possible presence of diffusion effect, estimated to be 25 ± 10 nm, due to LAMP process. However, those results are suspicious and have to be replicated for validity, and verified using another testing method, i.e. XPS, in particular as diffusion of polymer into the metal is very unlikely because of their reptation [91].

2.2.5. Electronic theory

The electronic theory of adhesion was proposed primarily by Derjaguin and co-workers in 1967 [93]. The authors have proposed that, as the substrate and adhesive have different electronic band structure, an electron transfer mechanism can occur to equalize the Fermi levels. This phenomenon could induce the formation of a double electrical layer at the interface, resulting in electrostatic forces, which can contribute significantly to the adhesive strength. The relevance of this theory has not been investigated for LAMP joints.

2.2.6. Weak boundary layers

Bikerman [94] suggested that failure of adhesive joints at the joint interface is doubtful and that the presence of a weak boundary layer promotes failure adjacent to the interface. Moreover, the diffusion of lower molecular weight fractions to the outer polymer surface can lead to the formation of weak surface layers. This is discussed in more depth in §2.4. To remove possible surface contaminants, promote interfacial adhesion, and prevent adhesive failure in LAMP, researchers have been investigating the effects of several surface pretreatments to increase chemical affinity and mechanical interlocking between joining partners, as elaborated in the next chapter.

2.3. Metal surface pre-treatments

An untreated metal surface, as it comes from the mill, has a surface topography resulting from the rolling operations, which might not be suitable for adhesive bonding or laser welding to polymeric materials. Moreover, a layer of adsorbed organic molecules is commonly present on top of the metal oxide as shown in Figure 11. These organic molecules are a result of contamination, from the atmosphere or manufacturing and handling conditions, resulting in an undefined surface chemistry. The presence of such

organic layer would limit the chemical interaction between the joining partner and metallic surface causing a reduced strength.

Due to similarities in bonding mechanisms between adhesive bonding and LAMP, and considering the fact that most of adhesives are polymeric in nature, researchers have been investigating similar surface preparation methods for both joining techniques. This section discusses some surface pretreatment techniques used in LAMP, and other prospective techniques that can be adopted from surface preparations relevant for adhesive bonding.

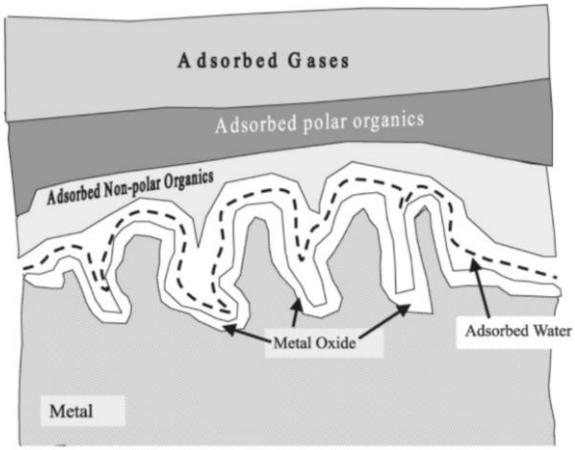

Figure 11: schematic diagram showing layered, rough structure expected from unprepared metal surface [95].

2.3.1. Mechanical pre-treatments

Bergmann et al. [36] investigated the effects of stamping and sandblasting, in order to create regular and irregular surface structures, on the joint strength of laser welded DC01 and PA6.6 sheets. Stamping was done by pressing a metallic die with protruding peaks on the metal plates resulting in an imbedded structure. Sand plating was performed using different bead sizes and fixed working pressure. The metal is then welded using a fiber-coupled diode laser, in single-lap joint configuration, before it was tested for shear strength. Sandblasting showed slight difference in surface roughness, but separation forces varies strongly. This suggests that other factors are influencing the joint performance besides the surface topography. Stamping resulted in high surface roughness which correlates to lower separation forces. However, surface topography of stamped samples showed no undercuts along the indentation, and the distribution density of structures was relatively low compared to sandblasted samples.

Schricker et al. [80] utilized aluminum surface machining to study effects of several geometric patterns on joint performance when welded to polyamide (PA6.6), using heat conduction laser joining. Several surface factors were investigated, such as groove width and depth, alignment, and structure density, using statistical DoE techniques. Results show the significance of depth and number of grooves, which highlights influence of total surface contact area between metal and molten polymer during welding process. This was further confirmed by strong correlation between volume and surface area of grooves with joint resistance to failure. Insignificant impact of width shows negligible influence of theoretical loadable area. In addition, drilled holes showed higher structural density and achieved higher shear forces than grooves.

While temperature distribution in the polymeric melting layer demonstrated strong influence on structural filling [61], the polymer's molten layer thickness showed insignificant effect on joint performance given that sufficient quantity of molten polymer fills the metallic surface structures [75]. Moreover, applying mechanical force to push joining partners together illustrated a positive effect on joint performance as it pushes molten polymer inside the grooves in the metal. Cenigaonaindia et al. [96] studied the effects of AISI 304 stainless steel surface structuring by milling process on joint performance when welded with polyamide (PA6) by laser transmission technique. Pressure was applied to the joining partners during and after laser beam irradiation to ensure proper filling of surface structures. Results favored an increased distribution density of surface structures to improve joint performance.

2.3.2. Chemical and electrochemical pre-treatments

Chemical surface treatments, such as chromic acid etching, have shown to produce higher adhesive joint strengths than solvent degreasing and grit blasting [97]. Regarding aluminum, common acid treatment involves chromic acid etching, chromic acid anodizing and phosphoric acid anodizing [98]. Anodizing process involves suspending the workpiece in an acid bath while applying a positive potential, causing growth in surface oxide thickness as well as changes in morphology depending on the used acid type and concentration, the current density and voltage applied, and on the time and temperature conditions [98]. Venables [99] concluded, for aluminum and titanium, that etching and anodization process produce porous oxide films leading to a mechanical interlocking effect with the polymer and stronger bonds.

Effects of metallic oxide layers when laser welded with thermoplastics were discussed by several authors [88], [92], [100]. Depending on thermoplastic properties and polarity, metallic surface properties result in significant influence on joint strength and performance. Jung et al. [100] investigated influence of steel zinc-coating on joint behavior when laser welded to carbon fiber reinforced plastics. Results showed that the thickness of zinc oxide layer on steel is correlated with joint strength when laser welded to ABS.

Zhang et al. [92] studied the effect of anodizing pretreatment on CFRP (PA6) to A6061 joined using fiber laser. Anodizing pretreatment showed to enhance the laser joining quality along with formation of porous nanostructure of oxidized layer on anodized aluminum surface, while the un-treated surface is relatively smooth. It is claimed that these structures can enhance the wettability of CFRP on A6061, as well as the mechanical anchoring effect. According to the result of the XPS analysis, it can be concluded that the increase in shear strength, relating to anodizing pre-treatment, is attributed to strong chemical bonding at the interface.

Lamberti et al. [88] investigated effects of aluminum anodization pretreatment on joint performance when laser welded to polyamide (PA6.6). Anodization resulted in a strong increase in joint resistance to failure with insignificant aging effect. Hino et al. [101] tested alkaline and acid dipping of mirror polished 1050 aluminum sheets on assembly performance when laser welded to polypropylene, having 50 μm styrene block copolymer (SBC) thermoplastic elastomer as an interfacial insert material. Surface of the insert material was polarized by a carboxyl group in order to improve the joining ability with aluminum. Results showed that an increase in surface area of aluminum resulted in an improved joint strength. However, extensive increase in surface roughness resulted in lower joint resistance to shear load and joining defects such as non-joined areas and

bubbles were detected at the concavity at the cavities. The joint strength changed considerably with chemical treatment of aluminum surface and insert materials. A correlation between joint strength improvement and -COOH group or an $-NH_2$ group highlights the possible formation of hydrogen bond between aluminum and insert material.

2.3.3. Primers

A primer is a coating which is used as an adhesive promoter. Primers are applied to substrate surface before the application of adhesive in order to promote wetting and develop strong interfacial forces between the adhesive and substrate. Primers are typically polymer solutions with good wetting capabilities and can act as surface treatments for removing impurities and protecting surface until adhesive is applied. Introduction of primers on substrate surface results in the formation of a new organic layer at the interface. This layer can be defined as bi-functional, it adheres well to both the adherent and the adhesive and provides improved interfacial bonding [78]. Silane is a typical example and the mostly used primer in adhesive bonding. Silanes are used to enhance adhesion between inorganic and polymeric materials as they contain a bifunctional molecule [78]. Regarding metal – polymer adhesive bonding, some other useful organometallic primers, such as those based on organotitanes, organozirconates and chrome complexes, have been utilized with varying degrees of success [102].

The use of primers for thermal joining, using hotplates and laser welding, has been recently reported to significantly increase shear strength of several metal polymer combinations (metals being mild steel, stainless steel, and aluminum and the polymer being a PA6 glass fiber reinforced polymer) [72]. It can be concluded from this study that the use of primers significantly increases the shear strength of the welded joint, even compared to sandblasting. Moreover, an innovative process of using primers in LAMP was recently patented [103]. Prior to laser welding, the method comprises attaching a primer to a metal surface, then polymerizing the primer so that the metal surface is at least partly covered with surface immobilized polymer brushes.

2.3.4. Laser surface pretreatments related to metal – polymer joining

Laser surface pretreatments are widely used to functionalize a surface for better performance in a certain application. Depending on the material in process, laser system, and processing parameters used, a variety of surface properties can be achieved, e.g. ranging from super hydrophobic to super hydrophilic surfaces. High level of power densities ($>10^7$ W/cm^2) are usually obtained with pulsed lasers, and used for metallic surface ablation. The process relies on short and powerful bursts of light to create a rapid increase in pressure to break bonds at the material surface. High Peak Pulse Power (PPP) causes effective material removal by pressure gradients between the interaction zone and surrounding atmosphere. Liquid and vapor metal are expelled upwards from the irradiated spot by an energetic plume of evaporated particles.

Amend et al. [104] investigated aluminum-polycarbonate (Al-PC), aluminum-glass-fiber reinforced polyamide (Al-PA66-GF30), and aluminum-polyamide (Al-PA6) joints by both transmission joining and direct joining. Connected grid and disconnected crater structures were formed at the aluminum surface using Nd:YAG laser. In the case of Al-PC transmission joining, deep craters in the aluminum surface lead to high tensile shear strength in comparison with small craters. Laser structuring has formed undercuts, which enhanced the mechanical interlocking between plastic and metal. Adhesive failure

was reported for all PC-Al joints. However, laser structuring causes a different absorption behavior of laser radiation at the metal surface, which leads to a variable temperature distribution. In the case of direct laser welding, and for grid surface structure, all Al-PA6 and Al-PA66-GF30 joints have nearly similar tensile shear strength regardless of the laser structuring parameters. However, measurements of joint area were not reported. Concerning the crater structure, air voids are observed at the valleys of the structure, and was assumed as a result of lack of venting.

Holtkamp et al. [83] inspected the effect of laser surface structure density (per unit area) on stainless steel before laser joining with polycarbonate (PC), polyoxymethylene (POM), and polyamide (PA PACM)). While a joining process cannot be expected without any pretreatment, results show a linear increase of the shear strength correlating with an increase in structural density. Roesner et al. [81] studied the effect of several surface treatments on the thermal joining of stainless steel to different polymer combinations. The stainless-steel surface was structured using a µs-pulsed Nd:YAG disc laser. The created structure allowed for mechanical interlocking which was reported to be one of the main causes behind such increase in joint performance. An increase of structural density had a linear relation with increase in shear strength. However, those studies lacked the assessment of the surface composition and chemistry, which might have a significant contribution to the joint strength.

Lamberti et al. [88] studied effects of short pulsed laser ablation (causing natural oxidization) and anodization on laser welded aluminum-polyamide joints. Surface roughness analysis showed that anodization smoothed the surface, while ablation increased average surface roughness. Both surface pretreatments have shown a significant increase on the joint quality regarding shear strength. However, effects of laser ablation and anodization pretreatment parameters on joint properties were not investigated. After fracture, FTIR-spectroscopic analysis of the polyamide was performed. The spectra from the joined samples were compared with a reference spectrum, which was taken on the polyamide base material, in order to detect a possible physicochemical interaction at the joint interface and to show the effect of the surface treatments. The FTIR spectroscopic analysis showed that laser-ablated and anodized samples showed rearrangement of extra molecular structure. N-H stretch, C=O stretch and N-H bending + C-N stretch. This indicates the relevance of surface chemistry of materials on the joint's strength. However, effects of laser ablation parameters on surface topography and joint performance were not investigated in this article.

Wahba et al. [70] studied the effect of surface treatment and bubble morphology on joint strength between laser welded thixomolded Mg-alloy (AZ91D) and amorphous polyethylene terephthalate (PET). Laser beam was irradiated onto the AZ91D specimens to induce porosities near the metal surface. Then, the metallic surface was ground to expose these premade pores to the surface. Transmission laser welding was performed using a diode laser beam and compared with direct irradiation from the metal side. The laser melting pretreatment of metal surfaces was effective in improving the strength of plastic side laser irradiated joints. SEM imaging showed that the adequate morphology of the generated gas bubble is very critical to the joint quality – compared with networked wormhole morphology produced by plastic-side laser irradiation, discrete bubbles morphology obtained by metal side laser irradiation achieved higher joint strength. It is supposed that the expanding bubble pressure during welding has pushed the molten PET into the pores on the metal creating a mechanical anchoring effect. Although there was

no bonding at the interface on both sides of the bore, energy dispersive X-ray spectrometer (EDX) analysis confirmed that the molten plastic, filling the pore, was activated enough to achieve tight bonding with the metal surface and to completely mix with some metal fragment.

2.3.5. Summary

Surface pretreatments of metals prior to laser joining with polymers have shown to enhance joint performance and interfacial adhesion by promoting chemical bonding and mechanical interlocking. While primers influence the surface chemistry promoting chemical bonding, mechanical and chemical pretreatments, in addition to laser surface structuring, alter both surface chemistry and topography promoting surface wettability and mechanical interlocking. However, effects of surface topography on the interfacial thermal transfer during the laser welding process remain uninvestigated, and their influence on the joint properties and performance remain unknown.

2.4. Polymer surface pre-treatments

In the case of polymeric materials, most industrially useful polymeric materials found in a compounded state rather than in the pure chemical state. In addition, most polymers are not of a single molecular weight. Free radically polymerized materials can have a rather broad molecular weight distribution. The low molecular weight materials often rise to the surface, especially in semi-crystalline plastics as shown in Figure 12. Here, prospective pretreatments for polymers, that are commonly used to promote adhesive bonding adhesion, are introduced for their relevance to LAMP.

In order to enhance adhesion of polymers, Kinloch [95] advises the following:

1. The weak boundary layer of low molecular weight should be
    a. Removed (results in increase of surface energy).
    b. Chemically modified to provide a cohesively strong layer well bonded to the polymer surface.
2. The surface energy of the weak boundary layer needs to be increased to a higher value of the surface tension of the adhesive to be used.
3. The polymer surface topography should be improved to enable capillary action by the adhesive.

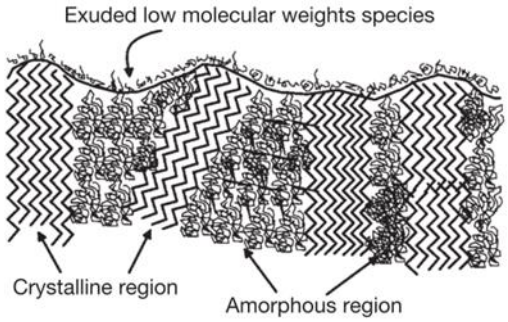

Figure 12: representation of semicrystalline polymer surface showing extruded low molecular weights species[95].

2.4.1. Corona discharge pretreatment

Corona discharge treatment CDT is essentially an unstable plasma operated at atmospheric pressure. Corona discharge is powered by a high frequency high voltage power supply. A dielectric layer must cover either the powered electrode or the grounded

electrode in corona discharge treatment. The gas in the apparatus is ionized by the discharged plasma causing ionization of the gas molecules in the gap between the powered and grounded electrodes. Corona pretreatment has been reported to have a significant effect on improving adhesive bonding strength in many articles [105]–[107].

2.4.2. Flame treatment

The concept and the equipment for flame surface treatment are simple. Like the corona treatment apparatus, flame treatment equipment involves central drum which is used as the base for the plastic sheeting. The plastic goes over the drum and under a series of burners with a controlled natural gas/air mix ratio. The flame can have considerably different characteristics depending upon the level of gas in the mix. Central drum is usually cooled, and the distance of the burners from the film is controlled to ensure proper treatment and protect the film from degradation. Flame treatment hand-held equipment are also commercially available, although uniform treatment is more difficult. Flame treatment has been reported to enhance the adhesion bonding [108], [109]. However, the use of flame treatment was not investigated in LAMP.

2.4.3. Plasma activation

Plasma activation and plasma polymerization are methods of surface modification employing plasma processing. Plasma activation only involves processing gas, generated from plasma source. Surface polymer functional groups are replaced with different atoms from ions in a plasma leading to an increase in surface energy. On the other hand, plasma polymerization uses plasma source to generate a gas discharge to activate or fragment gaseous or liquid monomer, often containing a vinyl group, in order to initiate polymerization. This allows the injection and control of various precursors in the plasma enabling desired functionalization of the treated surface.

Plasma activation can be used to promote adhesion. However, modified surface properties deteriorate over time and the surface energies return to their initial state [110]. Moreover, compared to plasma polymerization, this method has a limitation in determining the introduced surface functionalities. Plasma discharges, rich with highly reactive chemical species, initiates a multitude chemical processes upon contact with the surface. It efficiently removes organic surface contaminants, and deposits functional chemical groups with minimal changes to surface topography [111]. One of the common configurations used for plasma surface treatment is the dielectric barrier discharge (DBD) reactor. The concept of DBD involves electrical discharge between two electrodes separated by an insulating dielectric barrier.

Sperandio et al. [112] reported the influence of plasma surface treatment of an aluminum surface on its adherence in an aluminum-epoxy-aluminum assembly, in a single lap configuration. Plasma treatment has been reported to significantly increase bearable load of the assembly. Results show increased surface energy and altered surface chemistry of the treated samples. The reported optimum conditions were favorable to the creation of – OH and/or – O(OH) groups leading to improve the surface energy of the aluminum. Moreno-Couranjou et al. [113] investigated the effect of plasma polymerization, using several precursors, on the adherence of different polymer-polymer as well as metal-polymer joints assembled using adhesive bonding. Allyl alcohol plasma polymer coatings resulted in a significant increase in peel strength of natural vulcanized rubber to silicon adhesive. This can be explained by the increase in the total oxygen content in the

deposited layer with the formation of C-O bonds (as confirmed by XPS analysis), enhancing chemical adhesion between the treated rubber surface and the silicone adhesive. Functionalized Al surface coated with a DBD deposited 10 nm thick APTMS layer resulted in a significant increase in peel strength and a cohesive failure mode when joined with heat-sealed polyethylene films. It is supposed that APTMS layer deposition presented various oxygen-containing functional groups, predominantly carboxylic acids, aldehydes, and ketones. The reaction between primary amines and aldehyde groups resulted in imine development and an increase in the adhesion strength.

In LAMP, Aria et al. [34] examined the effects of plasma pretreatment, of both metal and polymer surfaces, on the strength of laser joined Cyclic Olefin Polymer COP (nonpolar polymer) and SUS304 (stainless steel) using high output power semiconductor laser. No joint could be obtained between both materials without pretreatment of COP, either using UV ozone pretreatment or plasma surface activation. XPS analysis has shown that UV–ozone pretreatment increased C-O and C=O bonds on the COP surface, and COO bonds were newly generated. As a consequence, fraction of oxygen functional groups increased considerably, increasing surface energy. It is supposed that the increase in joint strength is due to the increase of the interfacial interaction between the oxygen functional groups (generated by the surface-modification pretreatment of COP) and the Cr2O3 oxide film of SUS304 (generated from Reactive Ion Etching (RIE)). However, excessive surface-modification pretreatment caused joint strength to weaken. This might be due to presence of a weak boundary layer that accompanies the degradation of plastic surfaces.

2.4.4. UV Ozone lamp

UV ozone preparation method is effective in removing a variety of surface contaminations [114]. The cleaning mechanism is a photosensitized oxidation process. UV light excites and/or dislocates the contaminant molecules via chemical reaction with ozone molecule. UV radiation with a wavelength less than 200 nm dislocates the molecular oxygen O_2 present within the system, resulting in two free oxygen radicals. Each of those free radicals reacts subsequently with O_2 forming ozone O_3 molecule. UV radiation above 200nm is exclusively absorbed by organic chemical bonds present on the substrate surface, causing the creation of excited states or organic radicals. The reactive organic species react with the unstable ozone molecule resulting in the formation of volatile species such as CO_2, H_2O, N_2, and short chain organic compounds, which can easily desorb from the surface leaving it clean. The UV ozone treatment has been reported to significantly increase the LAMP joint strength, when performed on the polymer, as elaborated in §2.4.3 [34].

2.4.5. Summary

Studies proved UV ozone and plasma pretreatments of polymers in LAMP to improve joint performance by altering surface chemistry and improving surface energy. This enhances the wettability of molten polymer on the metallic surface during the laser welding process, and promotes interfacial adhesion.

2.5. Thermal Contact Resistance (TCR)

Increased surface roughness of metal has shown a positive effect on enhancing mechanical interlocking and LAMP joint strength (as mentioned in §2.2.1 and elaborated in §2.3) [81], [83], [104]. Increased surface roughness might also enhance surface wettability allowing for a better wetting of the molten polymer on the metal surface during laser welding

process. However, it is well known that an increase in surface roughness results in an increase in Thermal Contact Resistance (TCR) across the interface of two solid materials in contact [115], [116]. The flow of heat across the interface of two solid surfaces in contact is mainly governed by solid-to-solid conduction at points of contact and conduction through the fluid occupying the non-contact area restricting the heat flow [117]. Although direct laser welding of metals to polymers involves interfacial thermal transfer, effects of surface pretreatments and surface topography on TCR during welding process remain uninvestigated in literature.

Yovanovich [118] summarizes forty years of research in the field of TCR, and introduces the development of a geometric–mechanical–thermal model called the Cooper–Mikic–Yovanovich (CMY) model in order to predict the TCR of conforming rough surfaces. Factors which influences TCR are represented in the triad shown in Figure 13. The intersection of geometrical and mechanical attributes constitutes contact mechanics problem. The intersection of geometrical and thermal constitutes constriction (spreading) resistance problem, and that of mechanical and thermal constitutes thermal elestoplasticity problem. The intersection of the three attributes constitutes the TCR problem.

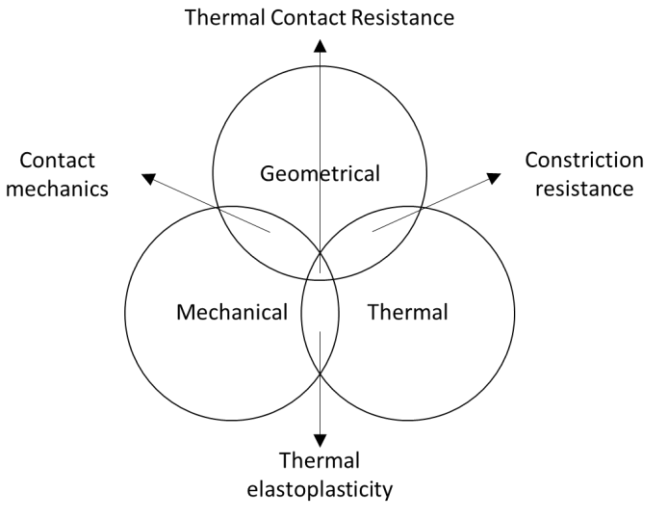

Figure 13: TCR triad [118]

Researchers [119]–[124] developed several models to calculate TCR. Three mechanical models; elastic, plastic, or elastic-plastic deformation of surface asperities were considered. In those models, surface asperities were assumed to be randomly distributed over apparent contact area and to follow Gaussian height distribution about a mean plane passing through each surface. Figure 14 shows schematic of joint formed between two nominally flat 'conforming' rough surfaces under a mechanical load.

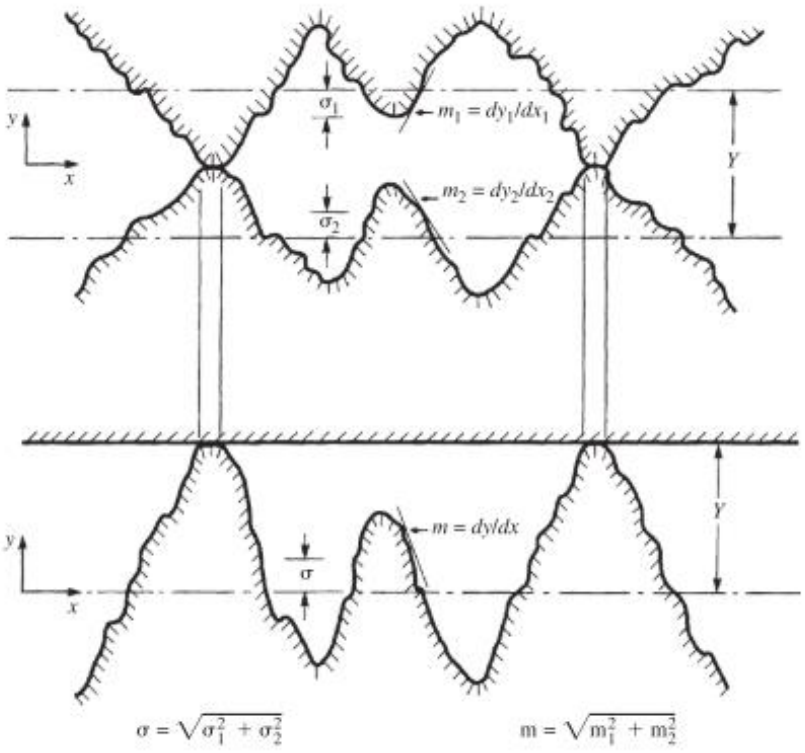

Figure 14: (above) illustration of joint formed between two conforming rough surfaces; (below) effective root mean square roughness (σ) and effective mean asperity slope (m) [118]

Based on the TCR model developed by Cooper et al. [122], Yovanovich [125] proposed a compact expression to calculate TCR between two nominally flat solid surfaces (1 and 2) in contact, assuming plastic deformation of surface asperities as shown in Equation 2. σ_1, m_1, k_1 are surface properties of material 1, and σ_2, m_2, k_2 are surface properties of material 2. $\sigma = (\sigma_1^2 + \sigma_2^2)^{0.5}$ is the effective root mean square roughness (RMS) so that $\sigma_{1,2} = \sqrt{\frac{1}{L}\int_0^L y^2(x)\mathrm{d}x}$, where L is the profile traced length. $m = (m_1^2 + m_2^2)^{0.5}$ is the effective mean asperity slope, where $m_{1,2} = \frac{1}{L}\int_0^L \left|\frac{\mathrm{d}y(x)}{\mathrm{d}x}\right| \mathrm{d}x$ is the mean absolute asperity slope. H represents microhardness of the softer material and P is the applied pressure. k_h is the harmonic mean thermal conductivity at the interface where $k_h = 2k_1k_2/(k_1 + k_2)$. Equation 2 shows that TCR is proportional to the ratio of root mean square roughness σ, also called Rq, to the average quadratic slope of asperities m, also called Rdq.

$$TCR = \frac{0.8\sigma}{mk_h}\left(\frac{H}{P}\right)^{0.95} \quad \text{..... (2)}$$

Where:

TCR	Thermal Contact Resistance (m^2K/W)
σ	effective root mean square roughness (μm)
m	effective mean asperity slope
k_h	harmonic mean thermal conductivity (W/mK)
H	hardness of the softer material (MPa)
P	applied pressure (MPa)

2.6. Design of Experiments (DoE)

This chapter already illustrated that LAMP process and surface pretreatments involve several interrelated parameters highlighting the processes' complexity. Statistical DoE is a powerful tool for screening significant parameters and optimizing processes. DoE utilizes statistical methodology to analyze data and predict performance under all possible parametric conditions within the limits selected in the experimental design.

In contrast to the One Factor at A Time (OFAT) approach, where all variables are kept constant and only the factor being studied is varied, DoE approach varies several factors simultaneously to develop a deeper understanding of the process window, and determine influence of a particular parameter on performance. DoE method investigates possible interactions between different parameters and models the process mathematically, generating the required information with the minimum amount of experimentation.

A DoE methodology was first proposed by Sir Ronald Fisher in the 1920s [126], and further elaborated in his book titled "The Design of Experiments" (1935) [127]. His pioneering work initially dealt with agricultural applications of statistical methods, and his methods were later transferred to include several fields of research. The process involved in DoE can be categorized into five steps:

1. Problem definition
2. Experimental planning
3. Running experiments
4. Data analysis using statistical methods
5. Reporting results

The problem definition stage is critical to clearly define challenges and desired output. After the problem is clearly defined, factors (independent variables) which might influence the desired output (dependent variable) have to be identified. Independent variables, e.g. laser power, beam speed, welding geometry, can either be quantitative or qualitative. However, their parametric levels have to be conveniently identified to set up the experimental space and process window under investigation. While responses (dependent variables) are commonly quantitative, e.g. strength of joint, joint deflection, etc., in some situations, responses can be qualitative, e.g. pass/fail, yes/no. However, qualitative responses do not provide a good response to model, and a procedure must be developed to quantify such qualitative responses. Since conclusions are based on statistical analysis and confidence intervals, the number of data points needed to be collected is defined by the desired statistical power and effect size.

The third step is to conduct experiments to collect the data. In this step, randomization is key to avoid introducing inherent errors which can lead to biased conclusions. The third step is data analysis. This can be done either manually or with the aid of a computer software. Based on this step, further experiments might be required to expand the process window and identify the optimal parametric setup. Based on a specific confidence level (e.g. 95%), the effect of each parameter is evaluated and a mathematical model is generated. The final step is to report and summarize the obtained results.

Response Surface Method (RSM) was introduced by E. P. Box and K. B. Wilson [128] in 1951 to explore the relationships between several variables and one or more response (outcome). RSM utilizes DoE in a series of experiments to obtain optimal response. It

generally includes two design steps: screening and optimization. The aim of screening experiments is to identify the most significant factors that influence the response. Some statistical methods have been utilized for this purpose such as definitive screening designs, Plackett-Burman designs, and fractional factorial designs [129], [130]. While Plackett-Burman and fractional factorial designs screen linear terms, definitive screening designs provide information about square terms and 2-way interactions between variables. However, fractional factorial and Plackett-Burman designs often have the lowest number of runs in a single replicate for a given number of variables, and more experimental runs can be added to model quadratic terms. A design matrix is generated where two levels, low (-) and high (+) are given to each factor. With 8-run Plackett-Burman design, the significance of up to 7 factors can be investigated as shown in Table 3. With 12-run, 16-run, and 20-run designs, up to 11, 15, and 19 factors can be investigated respectively. A folded design doubles combination in order to reduce confounding and increase resolution of design.

Table 3: Plackett-Burman 8-run matrix

		Factors						
		A	B	C	D	E	F	G
Treatment Combinations	1	+	-	-	+	-	+	+
	2	+	+	-	-	+	-	+
	3	+	+	+	-	-	+	-
	4	-	+	+	+	-	-	+
	5	+	-	+	+	+	-	-
	6	-	+	-	+	+	+	-
	7	-	-	+	-	+	+	+
	8	-	-	_	-	-	-	-

Once important and influential factors are identified, optimization process takes place in a sequential process. First, the experimenter develops the experimental design, such as Central Composite Design (CCD) shown in Figure 15, conducts the experiments, collects the data, and identifies if the experimental space under investigation contains the optimal parameters for maximizing positive response. If not, method of steepest ascent is followed by relocating experimental space in the direction towards increasing positive response by adjusting levels of factors. Second, when the process is near optimum, experimenter investigates this process window for possible curvatures and non-linearities in the response in order to obtain a second-order mathematical model. Then, this model is analyzed to determine optimal conditions. In RSM, the experimental planning and design are mostly based on factorial designs, e.g. full factorial, general 2^k factorial, fractional factorial design. A regression model describing the relation between process variables and response is generated [131]. Statistical method such as Analysis of Variance (ANOVA) is used to analyze the results.

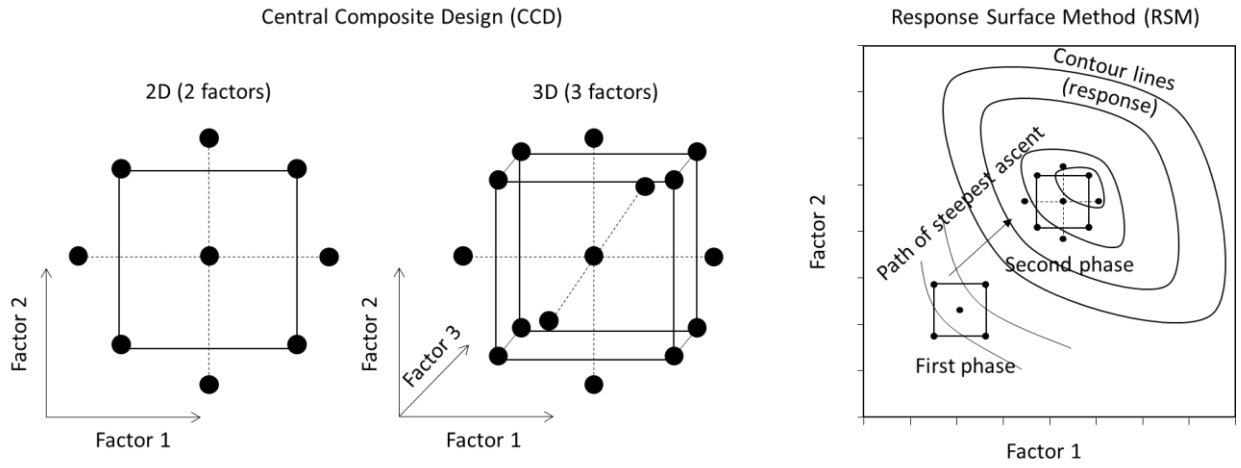

Figure 15: schematics of Central Composite Design and Response Surface Method optimization phases; black dots represents parametric setup

In reviewing the literature that uses DoE for LAMP processes, Cai et al. [42] utilized RSM to investigate influence of laser welding parameters in performance of titanium alloy (Ti64) – carbon fiber reinforced nylon (PA66CF20) joint. However, influence of processing parameters on joint quality and factors affecting joint performance were not reported. Schricker et al. [80] utilized DoE to identify important mechanical surface structuring parameters of metallic surface on performance of laser welded metal – polymer joint. Results indicate that the shear force could be correlated to the surface of the grooves and drilled holes, independent of geometry or alignment angle. However, influence of surface topography on interfacial thermal transfer during the laser welding process was not investigated.

2.7. State of the art summary

Laser welding of metals to polymers is a complicated process that involves many processing parameters, e.g. laser power, beam guidance speed, pulsing mode, etc. So far, research in LAMP has shown the reliability of the laser welding process in a variety of material combinations. While joining of titanium alloy (Ti64) to polyamide (PA6.6) is relevant for biomedical and aerospace industries, influence of laser welding parameters on quality and performance of laser welded Ti64 – PA6.6 joints is poorly understood. Weld defects such as lack of fusion, blow-out holes, pores, cracks or undercuts have been thoroughly investigated in laser welding of metals – metals. Yet, only bubbles formation was identified as a welding defect in LAMP while other defects are hardly recognized (gap 1). This research aims at investigating influence of Ti64 – PA6.6 laser welding parameters on joint quality and performance using DoE techniques. It models the impact of laser welding parameters on the joint strength and the evolution of critical weld defect, particularly laser induced deflection (§5.1).

The ability of surface pretreatments to improve interfacial adhesion in LAMP was already proven. Two main factors were reported to affect the joint performance; those are mechanical interlocking and physicochemical bonding. However, the combined nature of surface pretreatment outcomes makes it difficult to understand the factors affecting joint properties and performance (gap 2). Aluminum laser ablation was proven to improve performance of laser welded aluminum – PA6.6 joint [88]. Yet, it has an influence on both surface chemistry and topography, promoting both chemical bonding and mechanical

interlocking. On the other hand, plasma pretreatment mostly influences surface composition and chemistry not topography, eliminating its influence on mechanical interlocking. Effects of plasma pretreatment on LAMP joint properties are poorly investigated in the literature, and factors promoting interfacial adhesion, e.g. adsorption mechanism, are poorly investigated in LAMP. This research provides deeper understanding of the factors promoting interfacial adhesion towards a fully cohesive failure mode, by investigating laser ablation and atmospheric plasma pretreatment (§4.4).

While laser ablation pretreatment significantly improves LAMP joint performance, the influence of laser ablation parameters on joint strength and quality remains unclear (gap 3). This research utilizes DoE techniques to determine the impact of laser ablation pretreatment parameters on properties of laser welded metal – polymer joints. It identifies the most significant ablation parameters, and optimizes the laser ablation process in order to maximize joint performance (§4.5). Whereas the surface roughness of laser-ablated metals is expected to promote mechanical interlocking and interfacial adhesion, its effect on interfacial thermal transfer in LAMP and the resulted joint properties remains unknown (gap 4). This PhD thesis describes a new explanation to the influence of surface properties, which are related to interfacial thermal transfer, on the joint area and quality, and establishes the criterion for correlating the influence of topographic features on TCR and the joint resistance to failure (§5.5).

Chapter 3

3. Scientific hypothesis and strategy

3.1. Scientific hypothesis

It is well known that increased surface roughness of metals has a positive impact on LAMP joint performance by enhancing mechanical interlocking. However, increased surface roughness increases TCR between interfaces of two materials in contact limiting transfer of thermal energy.

It is hypothesized that, in case of direct laser welding of metals to polymers, increased surface roughness at interface increases TCR, limiting transfer of thermal energy to polymer, resulting in a decline in joint area and overall joint quality. It is claimed that, assuming relatively strong interfacial bonding, smoother surfaces at the interface of joining partners promote interfacial thermal transfer resulting in a broader joint area and improved joint performance.

In direct laser welding of metals to polymers, laser beam energy is irradiated on the metallic surface, gets absorbed, transfers into thermal energy, and the energy is conducted through the metal to the joint interface causing the polymer to melt and the joint to form. The hypothesis is based on TCR theory. Thermal transfer across interface takes place mostly by conduction at the solid-to-solid contact points and through the fluid (typically atmospheric air) between the surface asperities. Increasing surface roughness increases TCR causing less polymer to melt. Consequently, this reduces joint area, quality, and performance. Figure 16 shows a schematic of the hypothesis statement.

Based on the abovementioned hypothesis, a smoother metallic surface is preferable over a rougher alternative, given that both surfaces maintain relatively strong interfacial adhesion, i.e. fail with cohesive failure mode. A smoother surface promotes interfacial thermal transfer and increases joint area and performance (e.g. resistance to shear failure (N)). In order to test the hypothesis, cohesive failure mode has to be guaranteed to ensure interfacial adhesion does not affect the results. A constant joint strength (MPa) indicates nonsignificant changes in polymer's crystalline and morphological properties at the zone of cohesive failure. Given similar joint strength (MPa), changes in joint area (quality) and resistance to shear load (performance), correlating with changes in surface topography, indicate effects of surface topography on interfacial thermal transfer.

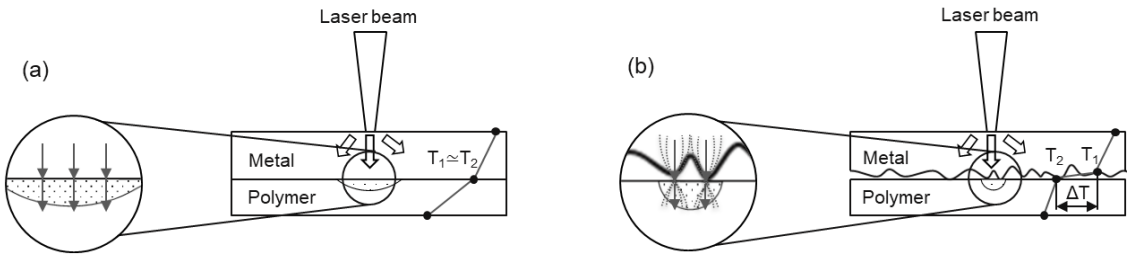

Figure 16: thermal transfer between ideally smooth interface (a); and rough surfaces (b).

3.2. Method to prove hypothesis.

Experiments were conducted on two material combinations; those are aluminum (Al1050) – polyamide (PA6.6), and titanium alloy (Ti64) – polyamide (PA6.6). Alongside the industrial relevance of those material combinations, aluminum and titanium are chosen because of their significantly different thermophysical properties. This will strengthen the hypothesis testing and proof reproducibility of results. To prove scientific hypothesis (gap 4), gap 1, gap 2, and gap 3 in §2.7 have to be filled at first.

Laser welding optimization DoE

To remove the impact of defects related to laser welding process on joint performance, optimum laser welding parameters were utilized for the material combinations in use and kept constant across all hypothesis-testing experiments. Laser welding parameters of Al1050 – PA6.6 were previously optimized [132]. This research utilizes DoE methods to optimize laser welding parameters of Ti64 – PA6.6, and investigate their influence on joint quality and performance (gap 1, §4.2.3).

Surface pretreatments preliminary investigations

In order to solely examine the impacts of interfacial thermal transfer on LAMP joint, the effects of interfacial chemical bonding and mechanical interlocking must be eliminated. Thus, a surface pretreatment method that alters surface topography while ensuring cohesive failure mode should be identified. Literature research showed potential of laser ablation and atmospheric plasma pretreatment in promoting interfacial adhesion in LAMP. While laser ablation influences surface chemistry and topography of the treated metallic surface, plasma pretreatment alters only surface chemistry with no significant topographic changes. It is important to benchmark factors promoting interfacial adhesion in order to prevent their influence on interfacial thermal transfer evaluation. Preliminary investigations were conducted for this step on Al1050 – PA6.6 assemblies to assess the effects of both pretreatment methods on surface characteristics and joint properties (gap 2, §4.4).

Hypothesis testing

After gaining a better understanding of the factors influencing interfacial adhesion, DoE techniques were adopted for both material combinations (Al1050 – PA6.6 and Ti64 – PA6.6) to investigate the influence of laser ablation parameters on joint performance and to optimize the process (gap 3, §4.5). Parameters which resulted in a broad range of high to low levels of joint resistance to failure were identified, and their effects on surface properties and resulted joint strength and quality were investigated. Effects of laser ablation parameters on surface topography and TCR are quantified, compared with theoretical CMY model, and correlated with joint quality and performance (gap 4, §5.5, §5.6). Figure 17 illustrates the scheme of the research methodology.

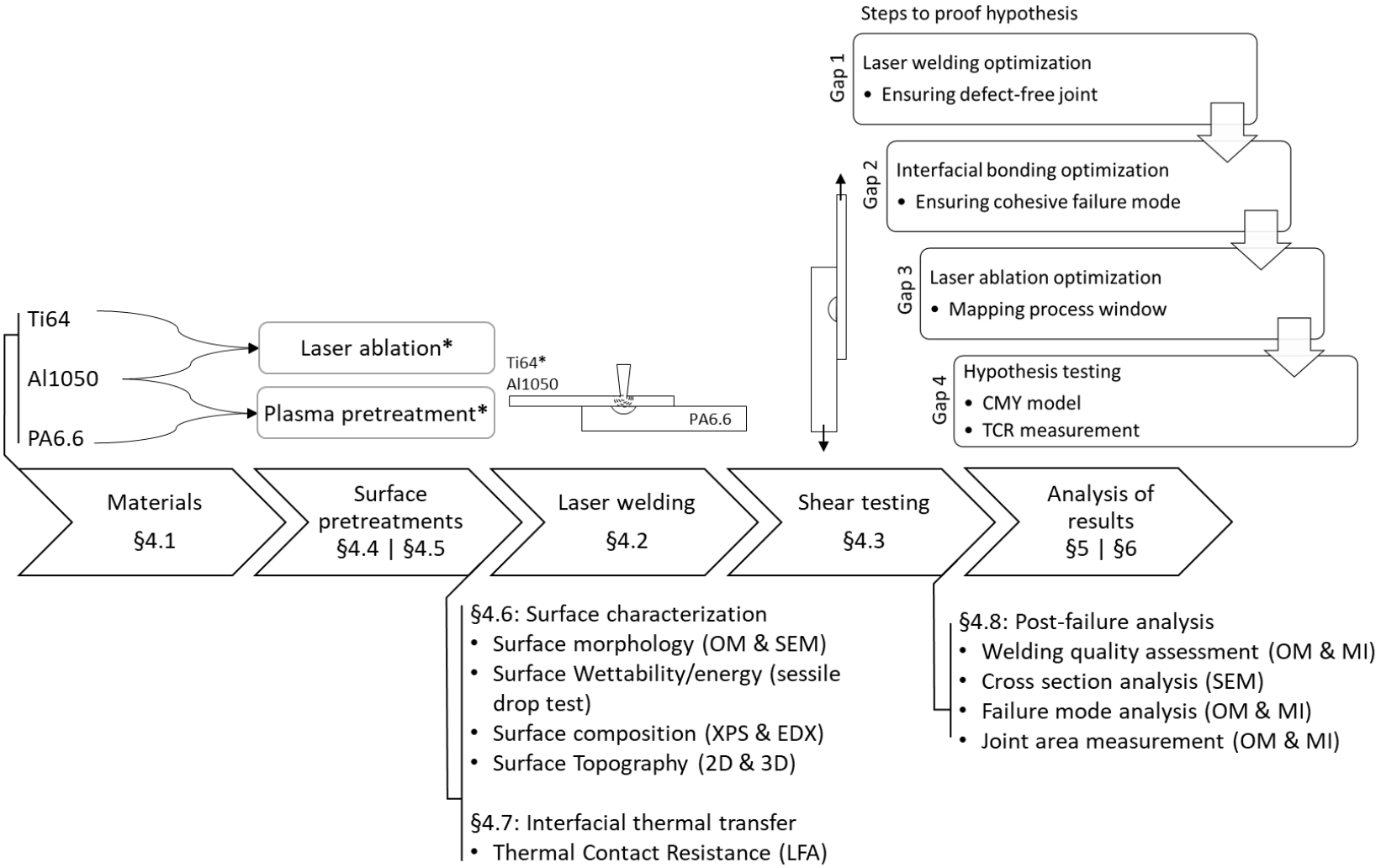

*Figure 17: research methodology scheme representing flow of materials, experimental steps, and utilized assessment tools and methods; optical microscopy (OM), sessile drop test, Scanning Electron Microscope (SEM), X-Ray Photoelectron Spectroscopy (XPS), 2D and 3D profilometry, Laser Flash Analysis (LFA), macroscopic investigations (MI); Design of Experiments (DoE); Cooper–Mikic–Yovanovich (CMY) model; Thermal Contact Resistance (TCR); ***** DoE investigations*

Chapter 4

4. Materials and Methods

This chapter illustrates materials and methods used in this research. It elaborates the used equipment and parameters, and describes the DoE approach utilized to optimize laser welding and to investigate the effects of laser ablation and plasma pretreatments on surface properties and interfacial adhesion. In addition, this chapter describes the process and equipment used to investigate the effects of surface properties on interfacial thermal transfer, joint properties, and performance.

4.1. Materials

To strengthen the hypothesis testing and generalize the findings, two metallic materials were used in combination with polyamide (PA6.6): Aluminum (Al1050) and titanium (Ti64).

4.1.1. Metals

Al1050 has very distinct properties in comparison to Ti64. Al1050 is a commercially pure aluminum alloy with more than 99.50% purity, while Ti64 is an alpha – beta alloy. It contains 6% Aluminum (alpha-stabilizer) and 4% vanadium (beta-stabilizer) alloying elements by weight. Table 4 and Table 5 show the elemental composition of Al1050 and Ti64 respectively. The physical and mechanical properties of Al1050 are distinctively different from that of Ti64. For example, Ti64 has roughly 3% of the thermal conductivity of Al-1050 [133], [134]. Table 6 show the comparison of thermophysical properties of both materials. Having such distinctive material properties (chemical elements, crystalline structure, thermal properties, etc.) between both metals has its advantage in generalizing the research findings, and in avoiding confounding bias [135].

Table 4: elemental composition of Al1050 [133]

Element	Mn	Fe	Cu	Mg	Si	Zn	Ti	Al
Atomic weight %	< 0.05	< 0.40	< 0.05	< 0.05	< 0.25	< 0.07	< 0.05	< 99.5

Table 5: elemental composition of Ti64 as provided by supplier (E. WAGENER, Weissach, Germany)

Element	Fe	C	N	H	O	Al	V	Ti
Atomic weight %	0.18	0.014	0.009	0.0094	0.132	6.12	4.28	rest

Table 6: Metallic material properties [133], [134]

Material property	Al1050	Ti64
Melting temperature (°C)	650	1878
Density (g/cm^3)	2.71	4.429
Thermal conductivity (W/m.K)	222	7.1
Thermal expansion (10^{-6}/K)	24	8.7
Tensile strength (MPa)	100	862
Shear strength (MPa)	60	760
Modulus of elasticity (GPa)	71	104

4.1.2. Polymer

Alongside its industrial relevance (see §1.2), polyamide (PA6.6) was used in those experiments because of its strong polar properties. The strong polarity of PA6.6 is expected to promote its wetting on a metallic surface when melting during the laser welding process. PA6.6 is a semicrystalline polymer. Differential scanning calorimetry (DSC) investigation for the PA6.6 in use illustrates 20.18% crystallinity as shown in Figure 18. The number 6.6 stands for the number of carbon atoms in its basic building blocks. DSC analysis identified a glass transition temperature of 53.64 °C, and a melting temperature of 258.59 °C. Given its hygroscopic nature, PA6.6 tends to absorb water from atmospheric moisture, which can lead to the formation of bubbles and impact mechanical properties. Thus, drying in a high vacuum chamber is occasionally used to reduce moisture in stored samples. Table 7 shows the properties of PA6.6 in use as received from supplier (Dutec, Ahaus, Germany).

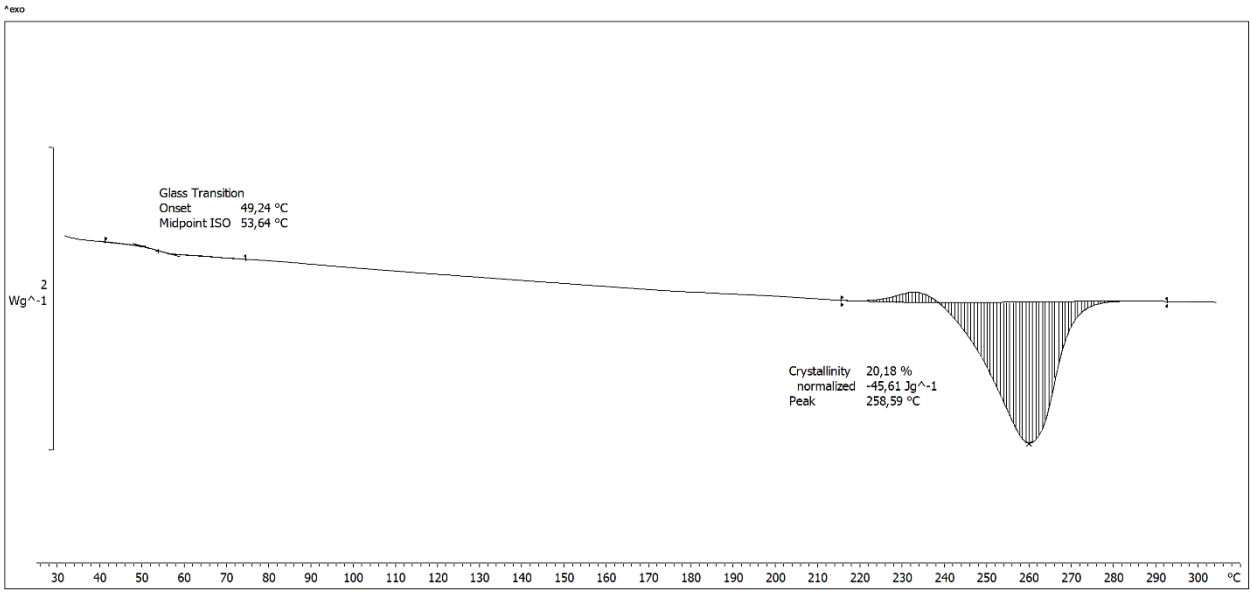

Figure 18: DSC of polyamide (PA6.6)

Table 7: properties of polyamide (PA6.6) (Dutec, Ahaus, Germany) [132]

Material property	Testing method	Value
Melting temperature (°C)	ISO 11357-3	260
Density (g/cm^3)	DIN EN ISO 1183-1	1.15
Moisture absorption (%)	DIN EN ISO 62	2.8
Yield strength (MPa)	DIN EN ISO 527	85
Elongation at failure	DIN EN ISO 527	50%
Thermal conductivity (W/m.K)	-	0.23
Thermal expansion (10^{-6}/K)	DIN 533752	80
Shear strength (MPa)	-	47.8
Modulus of elasticity (GPa)	DIN EN ISO 527	3.3

4.2. Laser welding

In these experiments, 0.5 mm thick metal plates (Ti64 and Al1050) were used together with 4 mm thick PA6.6. Samples had a geometry of 30 mm x 60 mm and 25 x 75 mm for metal and PA6.6 respectively. During the laser welding process, samples are clamped in an overlap configuration as shown in Figure 19 (a).

Laser welding is performed using a fiber laser (TruFiber 400) from TRUMPF. The laser beam has a wavelength of 1070 nm, a spot size of 31 µm, Rayleigh length of 0.649 mm, and peak power of 400 W. The laser beam is irradiated on the metal surface, where it is partially absorbed, transferred into thermal energy, and conducted to the joint interface causing the polymer to melt and the joint to form. In order to widen the weld, the laser beam followed either a zigzag or spiral wobble trajectory. Figure 19 (b) shows the welding setup with an example of a wobble trajectory. Beam guidance speed (V_f) is referring to the resulted feed velocity in the weld direction. Shielding gas was only used in the case of laser joining Ti64 – PA6.6, and not for Al1050 – PA6.6, to prevent an interaction of Ti64 with atmosphere during the laser welding process.

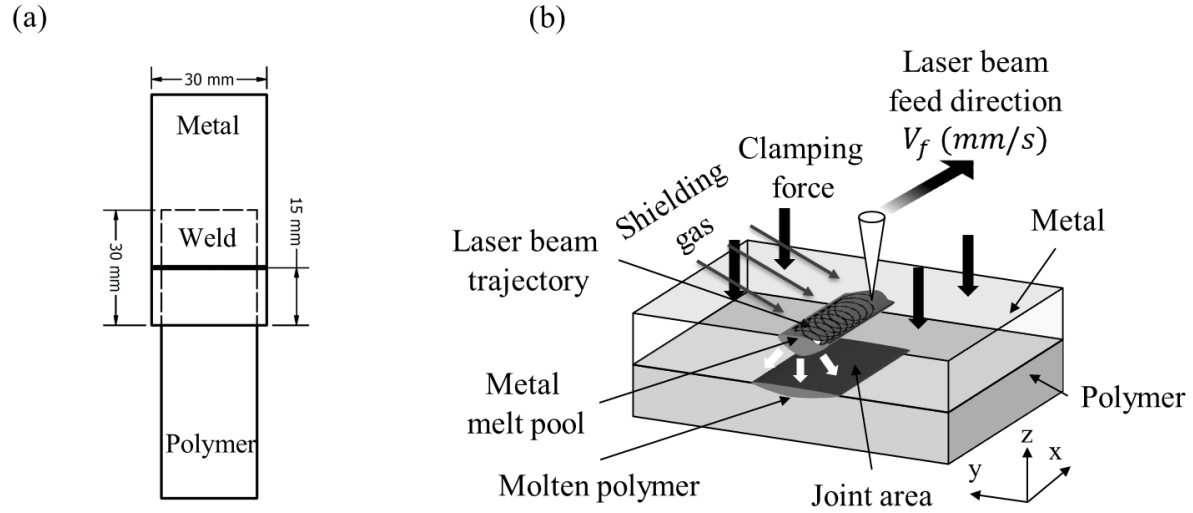

Figure 19: metal- polymer configuration (a); laser welding configuration (b)

4.2.1. Aluminum (Al1050) – Polyamide (PA6.6)

Laser welding of Al1050 – PA6.6 was previously optimized to obtain a robust weld while avoiding polymer degradation at the joint interface [132]. The laser beam is irradiated on the aluminum surface with a calculated spot diameter of 58 µm. In order to obtain a key hole and for the laser energy to pierce through the native aluminum oxide layer while protecting the polymer from degradation due to excessive thermal input, a laser power of 400 W was modulated with a pulse frequency of 25 kHz, and a pulse duration of 35 µs, as shown in Figure 20 (a). This results in an average power of 350 W, as described by Equation 3. The laser beam followed a spiral wobble trajectory, as shown in Figure 20 (b), with a corresponding feed velocity V_f = 88.8 mm/s. V refers to tangential velocity of the wobble trajectory. Wobble repetition rate was defined by the distance parameter λ. The laser beam spatial modulation guidance along the weld seam is described by Equation 4. No shielding gas is used in this welding process.

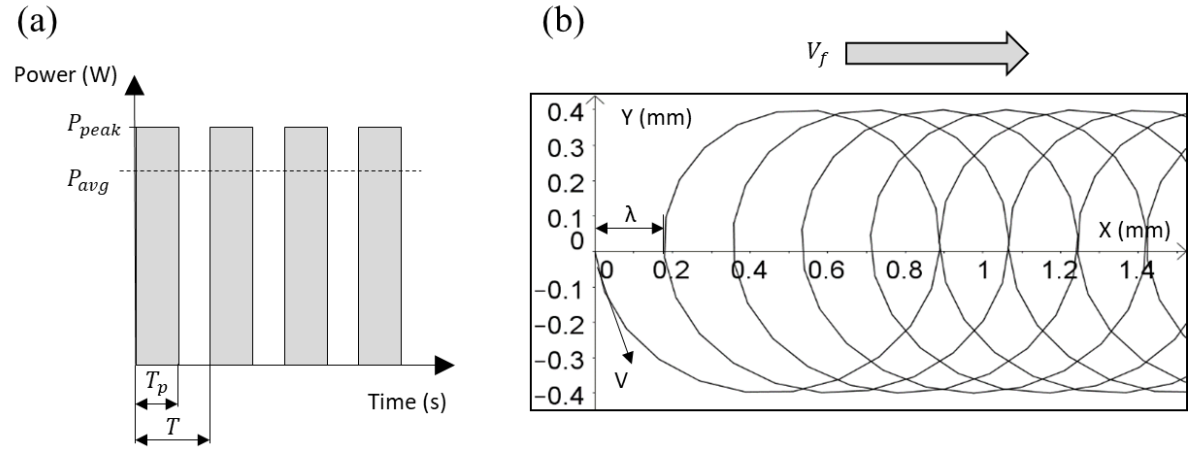

Figure 20: schematic of pulse modulation (a); and laser beam spiral wobble trajectory (b)

$$P_{avg} = \frac{T_p}{T} \times P_{peak} \quad \text{(3)}$$

Where:

P_{peak}	peak power (W)
P_{avg}	average power (W)
T_p	pulse modulation time (s)
$f_p = 1/T$	pulse modulation frequency (Hz)

$$\begin{pmatrix} x_{(t)} \\ y_{(t)} \end{pmatrix} = \begin{pmatrix} a\cos(2\pi ft+\pi)+v_f t+a \\ -a\sin(2\pi ft) \end{pmatrix} \quad \text{(4)}$$

Where:

a	wobble amplitude (mm)
f	wobble frequency (Hz)
V_f	feed rate (mm/s)

4.2.2. Titanium (Ti64) – Polyamide (PA6.6)

Ti64 was joined with PA6.6 with the optimized process parameters based on the DoE investigations described in §4.2.3. CW laser beam was focused and irradiated on Ti64 surface with 60 W following wobble trajectory shown in Figure 20 (b), having wobble distance parameter (λ) of 0.2 and a beam guidance speed (V) of 900 mm/s. In those experiments, shielding gas was used to prevent interaction between titanium and the atmosphere. Argon shielding gas was targeted at the weld zone, with a flow rate of 10 L/min and 20° inclination angle below the horizontal.

4.2.3. Laser welding optimization DoE

While the laser welding parameters of Al1050 – PA6.6 were already optimized (§4.2.1), this chapter illustrates DoE techniques used to outline the influence of laser welding parameters on the joint strength and quality of laser welded Ti64 – PA6.6, and to optimize the joining process (gap 1). Among other parameters, effects of laser power, beam speed, pulse modulation, and shielding gas type on joint resistance to failure was investigated.

One Factor at A Time (OFAT)

In order to simplify the DoE and reduce number of factors, preliminary OFAT investigations were executed. First, effects of pulsing mode verses CW mode on joint resistance to failure were tested. Peak power (P_{peak}), pulse duration (T_p), and pulse frequency (f_p) were varied while keeping a constant average power ($P_{avg} = 144\ W$). Argon shielding gas with a flowrate of 25 L/min was used in those investigations, and delivered on the titanium surface using vitrines he nozzle configuration shown in Figure 21.

The influence of the shielding gas type on joint resistance to failure was evaluated using CW laser power output of 144 W and gas flowrate of 25 L/min. Here, argon and carbon dioxide shielding gases were tested for several reasons: their relatively low cost, wide availability, and high density compared to helium. This high density allows lower flowrates and reduces turbulence to the plasma formed during a keyhole welding operation. Wobble trajectory having 8 mm width, repetition distance λ = 0.2 mm, and beam guidance speed V = 900 mm/s, was used in all OFAT experiments. Afterwards, DoE was performed with the aid of Minitab software.

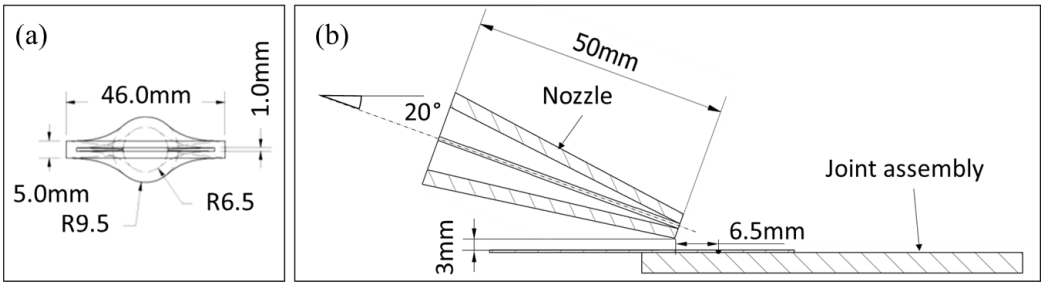

Figure 21: shielding gas nozzle dimensions (a); and configuration (b)

Screening DoE

Plackett-Burmann screening design [130] was used to highlight significant laser welding parameters out of six tested factors. Based on preliminary experiments, two levels per factor were adjusted conveniently so that different parametric combinations yield a reliable joint while avoiding severe burn-through or insufficient bonding. 24 runs design was set to yield 80% chance of detecting effect size of 1.06 standard deviations. This placket Burmann design does not effectively show the interactions between variables as interactions are confounded with all main effects. However, it is effective in determining significance of each parameter.

Table 8 shows tested parameters (factors) and their corresponding levels. Laser power is the output power delivered in CW mode. Beam guidance speed (V) is the velocity of the laser beam trajectory on the metal surface (Figure 20 (b)). The focal position is referenced on top of the titanium surface – a negative value is relative to the z-axis and indicates downward motion of the beam waist into the titanium surface. A z value of −1.33 mm and −2.33 mm results in a spot size of 65 µm and 114 µm on the titanium surface, respectively. Argon shielding gas was used with the indicated volumetric gas flow rate. Spiral and zigzag trajectories of the laser beam on top of the titanium surface are tested and described by categorical factor "beam trajectory." λ represents repetition distance between two consequent wobbles as shown in Figure 22. This parameter affects heat distribution density on the titanium surface during the laser welding process.

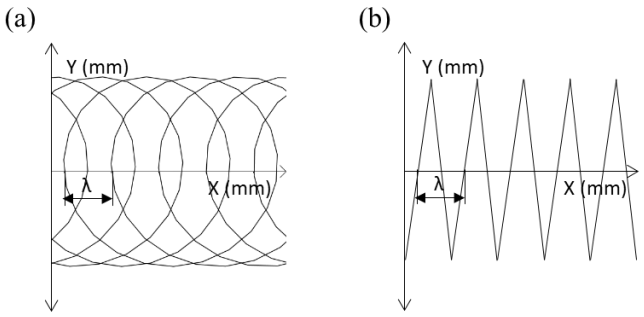

Figure 22: laser beam wobble trajectory of spiral (a); and zigzag (b) geometries.

Table 8: Factors screened in Plackett-Burman design of laser welding Ti64 - PA6.6.

Factors	Type	Low value	High value
Laser power (W)	Continuous	120	200
Beam guidance speed (mm/s)	Continuous	700	800
Focal position (mm)	Continuous	-1.33	-2.33
Gas flow rate (L/min)	Continuous	10	20
Beam trajectory	Categorical	Spiral	Zigzag
Wobble distance parameter "λ" (mm)	Continuous	0.2	0.4

Optimization DoE

After identifying significant parameters affecting joint resistance to failure, RSM was used to optimize the laser welding process and maximize th shear strength of welded joints. Parameters were simultaneously varied to determine possible interactions, and a predictive model was generated to describe response within investigated process window. Two consequent optimization experiments were conducted as shown in Figure 23. First, effects of laser power and focal position on joint strength were investigated using rotatable CCD (RSM 1) with two runs per cube point, two runs per axial point, twelve runs at center point, and a coded distance of $\alpha = 1.414$ from design center to axial star. A first regression model was generated to describe the response.

The optimal focal position was identified in this first RSM and kept fixed in the second RSM (RSM 2) where the effects of the laser power and beam guidance speed are studied. Fifteen parametric combinations, each with five samples, were tested in order to investigate broad process window. A second regression model was generated to predict strength at region with optimal welding parameters (RSM 2a). In order to verify predicted optimum, a final CCD (RMS 3) with 4 cube points, 4 axial points, a total of 6 center points, and $\alpha = 1.414$, was designed at the region of predicted optimal conditions. Effects of laser power and beam guidance speed on joint quality were analyzed and a regression model was generated to predict their influence on welding induced deflection (RSM 2b). ANOVA analysis was employed to test reliability of the developed models and significance of their coefficients.

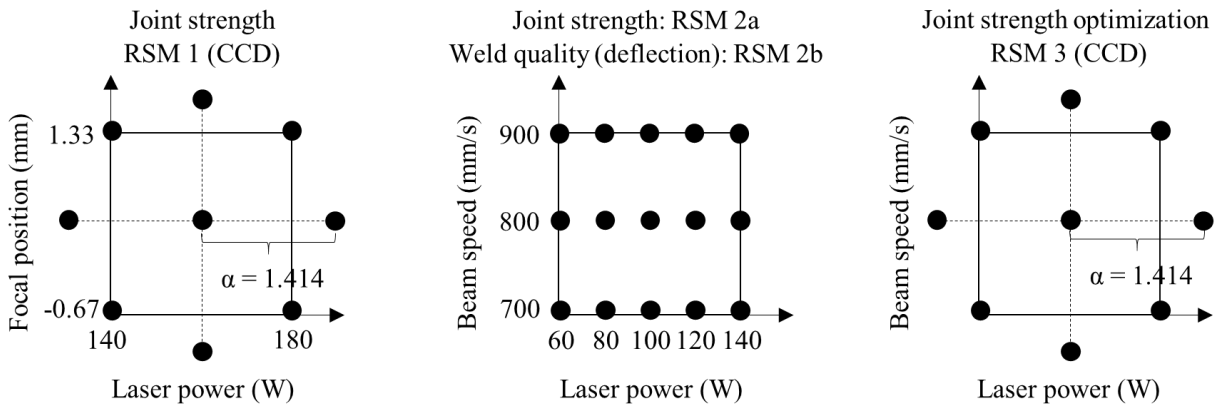

Figure 23: RSM designs for optimizing laser welding of Ti64 – PA6.6.

4.3. Shear-load testing

A single lap shear test was performed to quantify welded joint resistance to failure using Z010 from Zwick/Roell having a maximum load of 10KN. Samples were clamped in a vertical alignment with a jaw to jaw distance of 75 mm. It is expected for this testing configuration to impose bending moments and peeling forces on the welded joint during pulling test as shown in Figure 24 (a). Thus, a bending prevention devise was positioned close to the flat sides of the samples, as shown in Figure 24 (b), and is fixed to the ground. A gap of 0.4 mm ± 0.1mm is left between the bending prevention device and the samples being tested to prevent effect of clamping forces and its induced friction on shear testing results. Crosshead pulling speed was set at 2.21 mm/min.

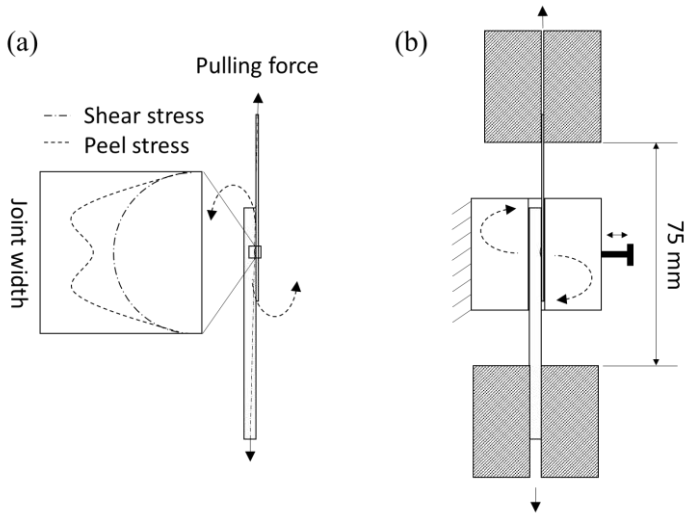

Figure 24: schematic of (a) simplified stress distribution on joint width during single lap shear test; (b) shear test configuration with bending prevention device

4.4. Surface pretreatments preliminary investigations

In order to understand factors influencing interfacial bonding and optimize interfacial adhesion, two surface pretreatments were investigated. In particular, two types of surface pretreatments of aluminum (Al1050), plasma surface modification and laser ablation, in combination with plasma surface pretreatment of polyamide (PA6.6), were explored. While laser ablation affects both surface chemistry and topography, promoting both chemical bonding and mechanical interlocking, plasma pretreatment affects only surface

chemistry and does not affect mechanical interlocking. Full-factorial DoE was used to model the influence of plasma surface pretreatment of aluminum and polyamide on the joint's resistance to failure. Effects of surface pretreatments on surface energy, surface chemical composition, and roughness characteristics were evaluated by sessile drop tests, XPS, and 3D profilometry respectively. Effects of surface pretreatments on joint resistance to failure were analyzed and failure mode was identified using SEM.

4.4.1. Plasma pretreatment DoE

Plasma pretreatment was performed in an open DBD reactor operating at atmospheric pressure as shown in Figure 25 (a). DBD reactor includes an earthed aluminum plate at the bottom, and two high-voltage aluminum plates at the top. DBD discharge is ignited between the top and bottom electrodes, that are separated by 3.25 mm thick glass plate to act as a dielectric barrier. Samples are positioned inside premade grooves at the bottom electrode and are adjusted so that their surface is levelled with that of bottom electrodes. 450 W plasma discharge resulting in a peak-to-peak voltage of 30 kV was ignited in a 3 mm gap. The top electrodes moved over samples to determine treatment time. Working gas used in the treatment had a total flow rate of 20 L/min and was a mixture of 20% vol. oxygen gas and 80% vol. nitrogen gas to represent atmospheric air. Based on the influence of plasma treatment time on Water Contact Angle (WCA), total treatment time was chosen as 3 s and 96 s for Al1050 samples, and 12 s and 60 s for PA6.6 samples, resulting in full-factorial design shown in Figure 25 (b). Since the medium value of the treatment time (3s, 12s) was not chosen to be exactly in the middle between the high (96, 60) and low values (0,0), for (Al, PA) respectively, care was taken when assigning the coded units used for generating the model relative to its "real world unit" value as shown in Table 9.

Prior to plasma pretreatment, Al1050 samples were prepared by submerging in ethanol ultrasonic path for 5 min, and polyamide was submerged in 10 min isopropanol ultrasonic path to remove surface contaminants, and to avoid the influence of any carbon-based contamination on the reference sample surface state. Isopropanol was preferred for PA6.6, in comparison to ethanol, because of its larger molecular size resulting in a lower probability of being absorbed by the polymer.

Table 9: coded units of plasma surface pretreatments' DoE

Level	Al (coded unit)	PA (coded unit)
Low	-1.00	-1.00
Medium	-0.94	-0.60
High	1.00	1.00

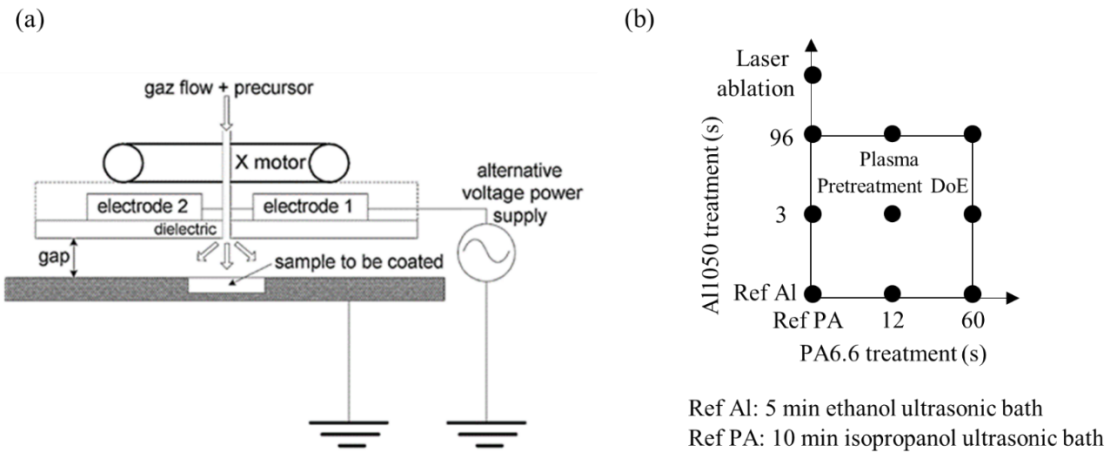

Figure 25: schematic of (a) DBD reactor [112]*; (b) full- factorial DoE design of plasma pretreatment (un-coded).*

4.4.2. Laser ablation

All laser ablation pretreatments were conducted by means of a short-pulsed laser beam using TruMark 6130 laser from TRUMPF with a wavelength of 1064 nm, forming a naturally oxidized layer at the top of the metal surface. The pulsing technique of the short-pulsed laser used in laser ablation is different from that of the fiber laser used for welding. The short-pulses (pulse duration in the Nano-seconds range) utilize Q-switching technique resulting in significantly higher PPP compared to the average power used in the process. In this method, the energy source is applied continuously, and the laser radiation, not the energy source, is emitted in the form of short laser pulses. The pauses between the short laser pulses under the condition of constantly pumped laser medium, helps in saving the energy required for amplification of the laser pulses. This results in high emitted PPP sufficient for vaporizing the already present oxide layer on the metal surface and melting metallic material beneath the vaporized oxide layer. The molten metal is exposed to atmospheric air. This triggers a rapid reaction with atmospheric oxygen, thereby, forming a fresh naturally oxidized layer. Inversely proportional relation between pulse frequency and PPP for pulsed laser can be described by Equation 5 below, and is illustrated in Figure 26.

$$PPP = \frac{P_{avg}}{T_{pulse} \times f_p} \quad \text{..........} \quad (5)$$

Where:

PPP	Peak Pulse Power (W)
P_{avg}	average power (W)
T_{pulse}	pulse duration (s)
f_p	pulse frequency (Hz)

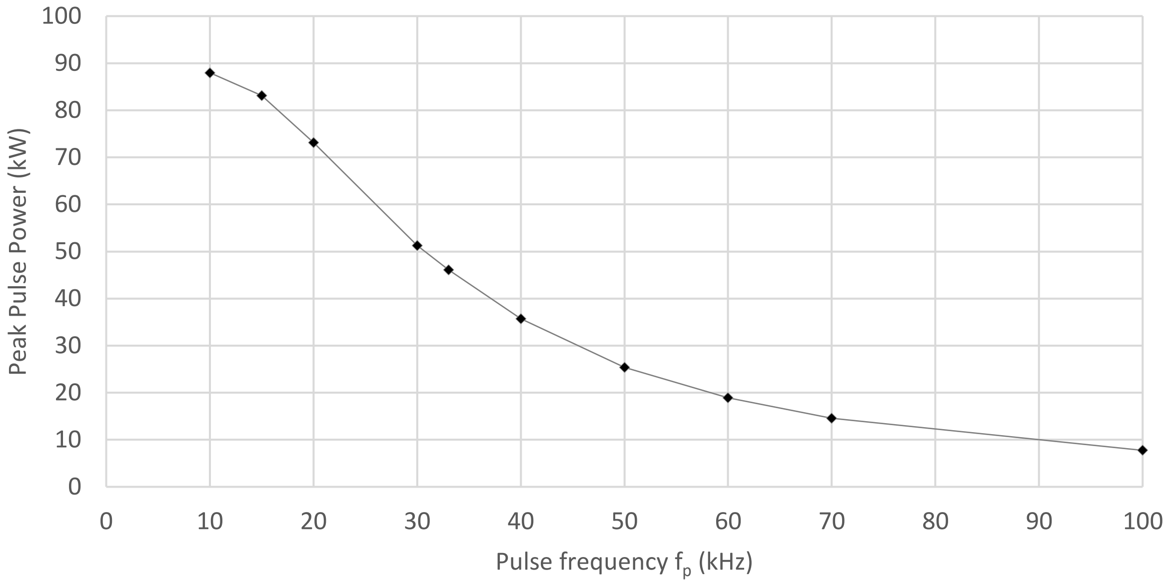

Figure 26: relation between Pulse frequency (kHz) and Peal Pulse Power (kW) for TruMark 6130 short-pulsed laser as provided by supplier (TRUMPF)

Laser pulses are irradiated on metal surface with the path shown in Figure 27 forming consecutive craters. Track width of 50 µm was kept between the centers of each ablation path. Pulses overlap ratio (OL) is influenced by beam diameter (∅), beam guidance speed (V) and pulse frequency f_p as shown in Figure 27 (a) and described by Equation 6. Keeping a constant beam diameter, independently decreasing the pulse frequency or increasing the beam speed results in a decrease in the overlap ratio. A negative overlap ratio indicates non-overlapping pulses, and usually results in patterned surface structure. An overlapping pulse ratio results in a stochastic surface structure. However, it is important to note that the theoretically calculated pulse overlap ratio might be different from resulted craters' overlap ratio as the latter depends on laser beam material interaction and its effects on crater diameter and morphology.

$$OL = \left(1 - \frac{V}{\emptyset \times f_p}\right) \times 100 \quad \text{.......} \quad (6)$$

Where:

OL	overlap ratio (%)
V	beam speed (mm/s)
$\emptyset$	beam diameter (mm)
f_p	pulse frequency (Hz)

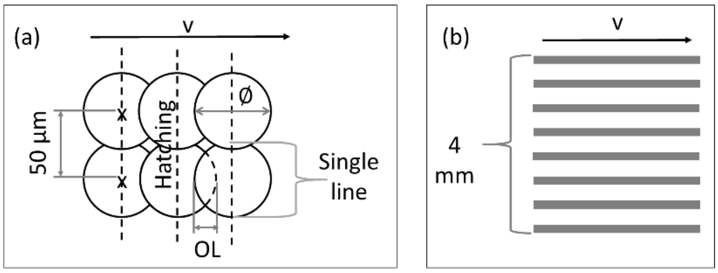

Figure 27: (a) schematic of overlapped pulses; (b) geometric repetition per single line when applying "lines" DoE variable

In the preliminary surface pretreatment investigations (§5.2), Al1050 surface was ablated with a laser beam spot size of 45 µm, beam guidance speed of 1776 mm/s, in combination with a pulse frequency of 88.8 kHz and pulse duration of 26 ns. This corresponds to a PPP of around 9 kW, and a pulse overlap ratio (OL) of 56%.

4.5. Laser ablation DoE

In order to optimize laser ablation pretreatment of metals for increasing LAMP joint resistance to failure, and to investigate effects of laser ablation parameters on surface properties, interfacial thermal transfer and joint performance, DoE techniques were used for both material combinations (Al1050 – PA6.6 and Ti64 – PA6.6). First, screening DoE is conducted for each material combination to determine the most significant ablation parameters. Next, RSM was used to model the effects of significant parameters on joint's resistance to shear failure. Effects of laser ablation parameters on surface properties, such as surface wettability, chemical composition, morphology, topography, and interfacial thermal transfer were investigated using sessile drop test, XPS and EDX, Scanning Electron Microscope (SEM), 2d profilometry, and Laser Flash Analysis (LFA). The effects of laser ablation parameters on joint strength and quality were outlined by measuring the joint area on both joining partners and investigating the joint cross-section.

4.5.1. Aluminum (Al1050) – Polyamide (PA6.6)

Screening DoE

Plackett-Burman screening design was set, with the aid of Minitab software, to highlight significant laser ablation parameters affecting the joint resistance to failure. Seven parameters were investigated using twenty-four experimental runs, resulting in a relatively high statistical power with 80% chance of detecting a small effect size (shift in mean value) of 1.06 standard deviation. Two levels were chosen per parameter. In addition to power percentage, which controls PPP, both beam guidance speed and pulse frequency were included in the design in order to be able to adjust PPP and overlap ratio separately and gain better control over the process window. At 100% power percentage, 15 kHz yields an approximately calculated PPP of 85 kW, while 40 kHz yields 35 kW, as shown in Figure 26 that was obtained from the machine manufacturer (TRUMPF).

Parameters included in the screening design are shown in Table 10. The focal position was varied from focusing on the Al surface (spot size of 45 µm) to a downward offset of 2.5 mm (spot size of 102 µm). Categorical factor "lines" refers to laser a scanning geometry. With this variable, the laser scans the geometry of a single line eight times with an equidistantly arranged offset within 4 mm wide geometry as shown in Figure 27 (b). Overlapping lines result in repetitive ablation of the treated area. The factor "rolling" corresponds to rolling grooves observed on Al1050 sheets that result from rolling process during sheet manufacturing. The factor "hatch" represents the alignment of parallel laser beam structuring groves as illustrated by the dashed lines in Figure 27 (a). Overlap ratio controls the distance between hatching lines. Axial and perpendicular orientations are referenced to the direction of the applied shear load.

Table 10: Al1050 laser ablation parameters investigated for significance in screening DoE

Variables	Type	Low value	High value
Pulse frequency (kHz)	Continuous	15	40
Beam speed (mm/s)	Continuous	1776	3776
Lines	Categorical	Off	On
Spot size (μm)	Continuous	45	102
Rolling direction	Categorical	Axial	Perpendicular
Hatching orientation	Categorical	Axial	Perpendicular
Power percentage (%)	Continuous	50	75

Optimization DoE

After identifying important factors, RSM was used to identify optimal parametric setup to maximize the joint's resistance to failure, and generate a predictive model to describe response. Four successive full-factorial experimental designs, with a total of 140 welded sample, were used to fit the model and outline process window as shown in Figure 28. While the first design is a full-factorial design with a center point, Face Centered Design (FCD) was used in the three following full-factorials to model curvature. ANOVA was utilized to determine reliability of developed predictive model and the significance of its coefficients at 0.05 level of significance. Levels of factors in consecutive designs were determined along the direction of increased resistance to failure. In order to efficiently investigate a large process window, some design points were common among full-factorial experiments. Process window was further expanded at optimal overlap ratio, beyond maximum pulse frequency of laser system in use, by lowering power percentage, thus decreasing the PPP.

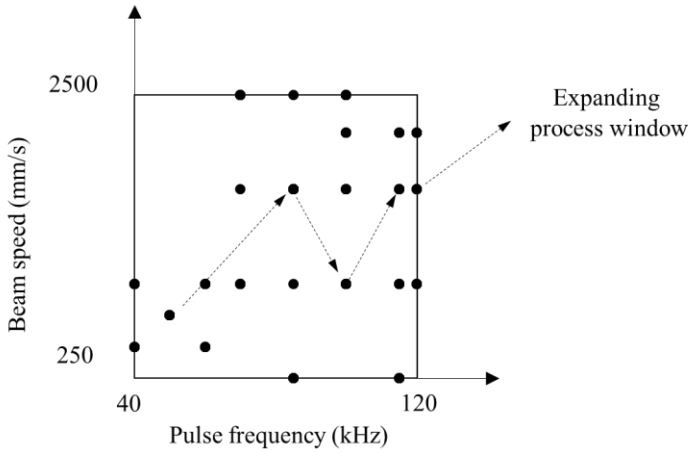

Figure 28: Al1050 laser ablation optimization design

4.5.2. Titanium (Ti64) – Polyamide (PA6.6)

Screening DoE

Plackett-Burman method was also used in this screening design with the aid of Minitab software. Six factors were tested as shown in Table 11. Two levels were chosen per factor and were determined based on results of preliminary investigations, in order to ensure adequate weld for all parametric combinations. Twenty-four experimental runs were designed resulting in a relatively high statistical power of 80% chance detecting standard deviation of 1.06.

Some of the tested parameters, in particular spot size, power percentage, pulse frequency, beam speed, and hatching, were commonly investigated in case of laser ablation DoE of Al1050 – PA6.6 experiments. However, because of the relatively higher hardness of Ti64 compared to Al1050, rollers do not induce deep indentations during Ti64 sheets manufacturing. Thus, the rolling direction was excluded due to their insignificance in Ti64 sheets. Parameter "lines" was also excluded to reduce thermal input on titanium and avoid possible deformation and geometrical distortion of the treated sample, specially that the thermal conductivity of titanium is considerably lower than that of aluminum. However, due to the high reactivity of titanium with atmosphere during laser processing, the effects of shielding the treated region with Argon shielding gas during the laser ablation process was investigated using a volumetric flow rate of 10 L/min and a nozzle tilt angle of 20° below horizontal. After the ablation, the welding process took place as described in §4.2.2.

Table 11: Ti64 laser ablation parameters investigated for significance in screening DoE

Factors	Type	Low level	High level
Spot size (µm)	Continuous	45	102
Pulse frequency (kHz)	Continuous	15	120
Beam speed (mm/s)	Continuous	1000	2500
Power percentage (%)	Continuous	10	70
Hatching orientation	Categorical	Parallel	Perpendicular
Shielding gas	Categorical	Off	On

Optimization DoE

After determining the significant parameters influencing joint performance, preliminary tests were conducted to determine a process window that covers variations in joint resistance to failure while resulting in a robust joint. An adequate process window was found between pulse frequency of 40 – 43.89 kHz and beam speed of 160 – 395.01 mm/s. FCD with a total of 8 cube points, 5 center points, and 8 axial points as shown in Figure 29, was used to model the effects of significant parameters on the joint's resistance to failure using RSM. ANOVA technique was used to determine significance of model coefficients and interactions between factors. In order to expand the process window under investigation and optimize the factors' setting for maximum joint performance, further tests were conducted along the path of steepest ascent as well as the path of optimal overlap ratio. Path of steepest ascent included four steps, having pulse frequency as a base factor and a step size of two coded units between the first three steps, and four coded units between third and fourth step. One coded unit represents half domain of variation of RSM design. Relatively large step size was used in following the path of steepest ascent in order to detect significant differences in the joint's resistance to failure as indicated by preliminary investigations. Fifty-six samples in total were tested for the complete optimization process.

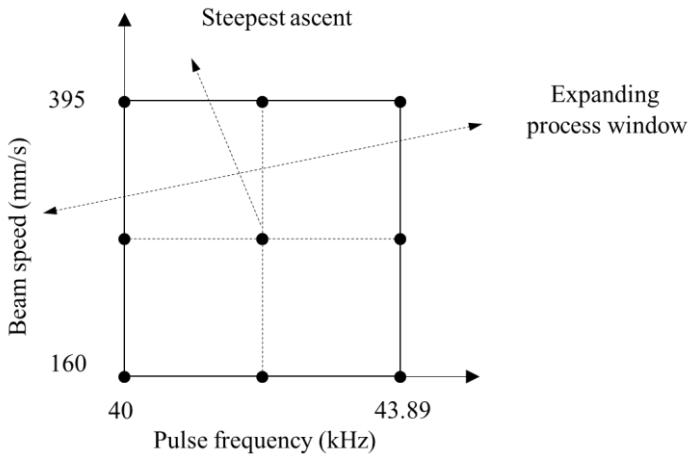

Figure 29: Ti64 laser ablation optimization design.

4.6. Surface characterization

4.6.1. Surface morphology

In order to investigate the effects of surface pretreatments on the morphology of treated surface, optical microscopy and SEM were utilized. Leica DM4000 microscope from FEI Company was used for optical microscopy, and a pressure-controlled FEI Quanta FEG 200 SEM was used for SEM. In case of laser ablation DoE experiments, secondary electron mode was used in SEM in order to get information about the samples' morphology. Six regions of 1 cm^2 area were ablated on an Al1050 sample and five regions of 1 cm^2 area were ablated on a Ti64 sample with several parametric combinations that resulted in a wide range of joint resistance to failure. When analyzing ablated Al1050, SEM analysis was performed at pressure of 3.27^{-4} Pa with 15 kV acceleration voltage. Ti64 SEM analysis was performed at a pressure of 1.10^{-3} Pa (in water vapor) and with a 20 KV acceleration voltage. A fine layer of conductive lacquer was deposited in contact with the untreated part of the metal samples to enhance conductivity. The area that was coated by this lacquer was not observed.

4.6.2. Surface energy and wettability

In order to investigate the effects of surface pretreatments on surface energy, the wettability of materials surface to water (polar) and diiodomethane (non-polar) was measured from static contact angle measurements using sessile drop test. Goniometer (OCA15+ from Dataphysics), driven by SCA 20 software, with a B. Braun (1mL) syringe was used to conduct experiments. A measurement with two liquids was performed for pretreated and solvent cleaned surfaces. An average and standard deviation values were calculated by performing 3 sessile drop experiments. The volume of liquid droplets was set to 2 µL.

Young's equation (Equation 1, §2.2.2) describes the relation between contact angle θ, the surface tension of the liquid σ_{lg}, the interfacial tension σ_{sl} between liquid and solid, and the surface free energy σ_{sg} (mN/m) of a liquid in contact with a solid surface. Surface energy was then calculated using Owens–Wendt–Rabel–Kaelble (OWRK) as shown in Equation 7, where the surface energy is split into two components, namely a polar and a dispersive part. Water and diiodomethane polar and dispersive part of the surface energy are given in Table 12 according to values from Strohm et al. [136].

$$\sigma_{sl} = \sigma_{sg} + \sigma_{lg} - 2\sqrt{\sigma_{sg}^{d}\sigma_{lg}^{d}} - 2\sqrt{\sigma_{sg}^{p}\sigma_{lg}^{p}} \quad \text{(7)}$$

Where:

σ_{sl}	interfacial tension (mN/m)
σ_{sg}	surface free energy (mN/m)
σ_{lg}	liquid surface tension (N/m)
σ_{sg}^{d}	dispersive part of solid surface energy (mN/m)
σ_{lg}^{d}	dispersive part of liquid surface energy (mN/m)
σ_{sg}^{p}	polar part of solid surface energy (mN/m)
σ_{lg}^{p}	polar part of liquid surface energy (mN/m)

Table 12: water and diiodomethane polar and dispersive surface energies [136]

Liquid	σ_{lg}(mN/m)	σ_{lg}^{p}(mN/m)	σ_{lg}^{d}(mN/m)
Water	72.80	51.00	21.80
Diiodomethane	50.80	0	50.80

In case of laser ablation, both water and diiodomethane showed perfect wettability behavior on the treated surfaces, i.e. contact angle below 5° and therefore not measurable. Thus, an innovative approach was conducted in efforts to analyze the evolution of contact angle on ablated aluminum over time. Five differently ablated aluminum samples were subjected to this test. A series of sessile glycerol droplet of 4 µl was deposited on the surface of each sample by means of a syringe pump. One droplet was deposited on each of the ablated aluminum surfaces and the value of the contact angle was extracted from the droplet shape using a numerical fit based on an elliptic model.

4.6.3. Surface composition

In order to investigate effects of surface pretreatments on the chemical composition of treated metallic surfaces, XPS and EDX tests were performed. While XPS analysis has a relatively shallow depth of penetration (20 nm maximum in aluminum), EDX analysis investigates a deeper depth of penetration (1-2µm) depending on the materials being tested and the parameters used in the tests.

Surface pretreatments preliminary investigations

In the preliminary investigations of surface pretreatments (§4.4), the chemical composition of aluminum surface was investigated using XPS (Specs Phoibos 150). Sample transfer into the XPS chamber was performed in ambient air, immediately after surface preparation (cleaning and plasma treatment). During the analysis, the sample was placed in an ultra-high vacuum environment (5×10^{-9} mbar) and exposed to a monochromatic Al Kα (1486.7 eV) source operating at 200 W with an anode voltage of 12kV. All measurements were carried out with an emission angle of 0° from the normal surface. A survey spectrum taken between 0 and 1250 eV and narrow scans in the C1s, N1s, O1s and Al2p regions were acquired. The pass energies were set to 80 and 20 eV for survey and narrow scans, respectively.

Laser ablation DoE

With reference to the laser ablation DoE experiments (§4.5), chemical composition of selected ablated aluminum surfaces was investigated using a K-alpha from Thermo Scientific (Waltham, MA, USA). An X-ray beam (Al Kα, 1486.6 eV) with a spot size of 30

μm was used in the analysis. When analyzing ablated Al1050, six points per ablation condition were investigated by measuring a survey spectrum (3 scans, 200 eV energy pass) and high-resolution spectra for the regions of Al 2p, O 1s, and C 1s (20 scans, 20 eV pass energy) atoms.

When analyzing ablated Ti64, three points per treated surface were investigated by measuring a survey spectrum (3 scans, 200eV pass energy) and high-resolution spectra for the Ti 2p, C 1s, O 1s, N 1s, Al 2p, V 2p regions (20 scans, 20 eV pass energy). A flood gun was used to avoid any charging effect. The calibration was done by setting the C-C / C-H bond at 284.8 eV.

EDAX GENESIS XM 4i EDX was used to obtain EDX spectra during SEM analysis. The analytical distance used for X-ray measurement was 10 mm corresponding to a take-off angle of 35°. An area of 0.15 x 0.13 mm^2 was scanned for each sample and the average spectrum was collected over the whole area. The surface composition is calculated from this spectrum, assuming that Al1050 sample is only composed of aluminum, oxygen, and carbon, and that Ti64 sample is only composed of titanium, aluminum, vanadium, oxygen and carbon. Those assumptions were made based on the peaks exhibiting a significant height throughout the whole EDX spectra.

4.6.4. Surface topography

3D surface topography

Surface topography was measured by a Tencor P17 3D profilometer by scanning a 100 x 200 μm^2 area, with a pixel size of 1 x 1 μm^2. Two measurements performed at different locations of the sample surface were carried out on each ablated surface to be able to assess the homogeneity of the topography. 3D unfiltered parameter Sa (arithmetical mean surface height) values were then calculated for each sample. Scanning force of 0.5 mg was used for Al and 0.05 mg for PA with a scanning speed of 100 μm/s.

2D surface topography

Effects of metallic laser ablation on surface topography was obtained for the ablated metal by means of a P17 (KLA Tencor, Milpitas, CA, USA) mechanical profilometer equipment using a scanning load of 0.5 mg. Measurements were performed by using acquisition rate of 50 Hz, a scanning speed of 20 μm/s, and a scanning length of 2 mm. This results in 5000 measured points and a scanning time of 100 s. The roughness profile was calculated with a cut-off length of 0.25 mm.

Six regions of 1 cm^2 area were ablated with different parameters on Al1050 sample, and five regions on the Ti64 sample. Four measurements were performed on each region; two along the axis of applied pulling forces during shear testing, and two perpendicular to it. Roughness parameters, with a focus on Rq (average quadratic height or "root-mean-square" roughness) and Rdq (average quadratic slope), were calculated following ISO 4287 [137]. Average values are reported. Similar measurements performed on PA sample show that its average quadratic height (Rq) is close to 40 nm, which is close to that of reference Ti64 (Rq ≈ 60 nm) and more than 25 times that of ablated Ti64 with Rq in the range of 1 – 6.5 μm. Raw (solvent cleaned) aluminum exhibited Rq values close to 400 nm, and ablated aluminum showed Rq values in the range of 0.9–6 μm. This shows that the PA is

very smooth compared to ablated metals and that the schematic drawing in Figure 16 (§3.1) is a reasonable representation of "real life" conditions.

4.7. Interfacial thermal transfer

Effects of ablated surface properties on interfacial thermal transfer was examined using LFA method. LFA is a method that dates back to studies by Parker et al. in 1961 to analyze thermophysical properties such as thermal diffusivity across workpiece [138]. During LFA measurement, the lower surface of a flat sample is heated by a short energy laser pulse. The resulting changes in temperature on the upper surface of the sample are measured with an infrared (IR) detector, resulting in the signal shown in Figure 30. An increase in the sample's thermal diffusivity results in a steeper signal. In a one-dimensional, adiabatic case, time value at half signal height (half time: $t_{1/2}$) and sample thickness (d), can be used to determine thermal diffusivity (a_{diff}) using Equation 8. Given specific heat (c_p) and density (ρ) of material being tested, thermal conductivity (λ_{cond}) at a certain temperature (T) can be calculated by means of Equation 9. Specific heat (c_p) can be determined by comparing the signal height (ΔT_{max}) of the tested sample with that of a reference material.

$$a_{diff} = 0.1388 \frac{d^2}{t_{1/2}} \quad \text{.....} \quad (8)$$

Where:

a_{diff} thermal diffusivity (m^2/s)
d sample thickness (m)
$t_{1/2}$ half time (s)

$$\lambda_{cond} = a_{diff}(T) \times c_P(T) \times \rho\,(T) \quad \text{.....} \quad (9)$$

Where :

λ_{cond} thermal conductivity (W/m·K)
a_{diff} thermal diffusivity (m^2/s)
c_P specific heat (J/kg·K)
ρ density (kg/m^3)

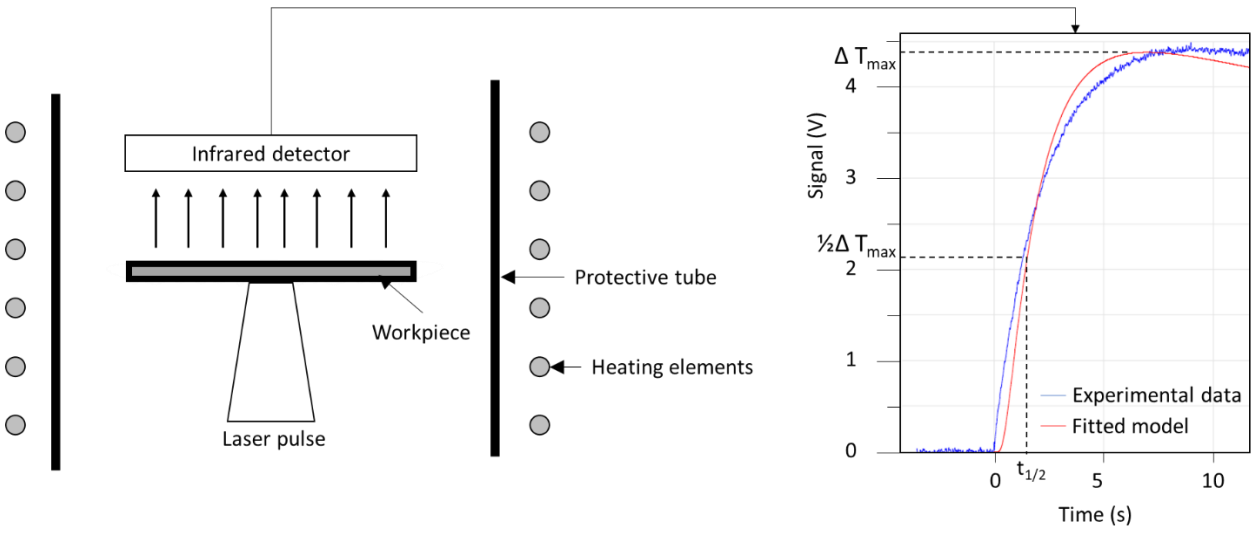

Figure 30: LFA setup for measuring diffusivity with an example of detected signal

In order to calculate effects of metallic laser ablation parameters on TCR, the layered configuration was used as shown in Figure 31. 0.5 mm thick Al1050 and Ti64 samples ablated with different parameters were cut to 1 cm^2 squared geometry using an Accutom 50 dicing tool from Struers. Then, ablated samples were arranged in layered configuration by being placed at the bottom with its ablated surface facing an untreated reference sample of the same material and dimensions. However, in the case of Al1050, 1 mm thick reference sample was used on top of ablated one to maintain more stiffness. Samples were coated on both external faces using Graphit 33 spray from Kontakt Chemie (Iffezheim, Germany) containing 1–5 w/w % of graphite powder, in order to have a consistent absorbance to the laser beam and consistent emissivity to the IR detector. Layered configuration was used instead of using a single ablated metal sheet, in order to avoid possible confounding of the surface topography on the assessment of the thermal diffusivity [139]. It is difficult to directly calculate the exact TCR between PA6.6 and the metal using LFA with such layered configuration due to experimental challenges resulting from the relatively high ductility and low thermal conductance of PA6.6. However, the calculated TCR value serves as a reliable assessment technique for comparing TCR across differently ablated surfaces of similar metal.

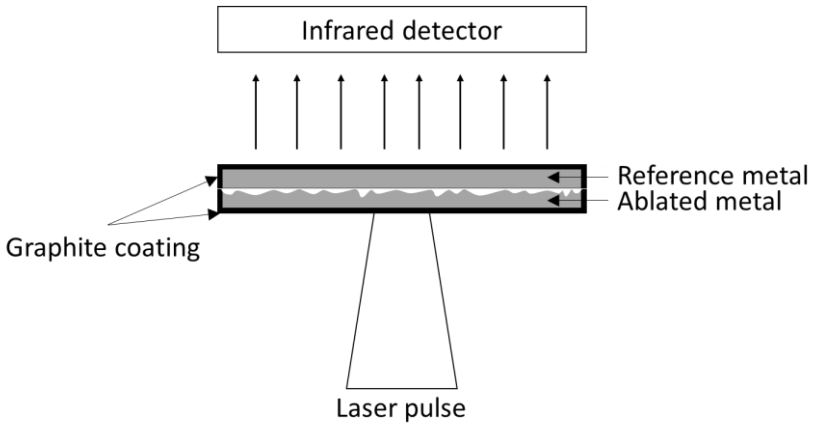

Figure 31: layered configuration in LFA for measuring TCR

LFA test was performed by a Netzsch LFA 457 Microflash machine (Selb, Germany). A single 0.5 ms flash from Nd-Yag laser was irradiated on the untreated side of the ablated sample, as illustrated in Figure 31. The LFA chamber was filled with dry argon gas at room temperature during the experimentation in order to reduce the influence of moisture on the measurement of the thermal properties. The temperature changes on the back face of layered samples were monitored by an infrared detector (InSb photodiode). The output voltage of the laser was fixed at 1922 V for all aluminum samples, and 2498 V for titanium samples. A duration of 60 ms was used for the acquisition time of the IR detector.

Thermal diffusivity of the layered system is calculated by measuring the increase in temperature at the back face of the reference metal, i.e., the side of the layered system facing the IR sensor, as a function of time. Next, TCR was calculated based on the algorithm developed by Hartmann et al. [140] by using predefined data on the density, thickness, thermal diffusivity, and specific heat of metallic materials in both layers for all tested samples.

4.8. Joint quality assessment

4.8.1. Welding quality assessment

To evaluate effects of Ti64 – PA6.6 welding parameters on joint quality, regions of the assembly were optically evaluated before and after failure as shown in Figure 32. Microscopic images were obtained using Leica DM4000 microscope, and macroscopic images were obtained using digital FUJIFILM X-Pro2 camera.

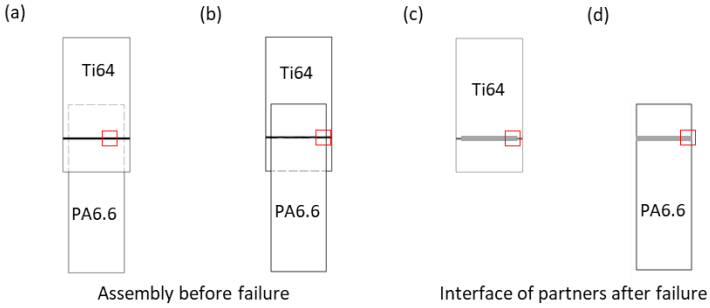

Figure 32: regions for investigating defects: (a) weld pool cavities; (b) flash; (c) excessive penetration; (d); bubbles and voids

Welding induced deflection was identified as a weld defect and investigated in depth. The deflection angle of the welded samples was measured by a developed coordinate system technique. First, samples were held uptight as shown in Figure 33 at a constant distance to the camera lens. Then, two lines (short end and long end) with fixed, but different, lengths are set to connect two points on the short and long terminals of the welded joint to the ends of the terminal. This method was used to avoid any calculation bias due to the induced curvature in the deformed titanium. It is very critical to account for the welding induced deflection as it can yield in a complete failure of the joint by peeling during handling or cooling down of the welded joint.

Figure 33: deflection measurement

4.8.2. Cross-section analysis

Cross-sections of welded samples were prepared to analyze quality of joint interface in different surface pretreatment conditions, and to investigate effects of laser welding parameters on microstructure and morphology of Ti64 – PA6.6 joints. Welded samples were cut in a perpendicular direction to the weld path, and mounted in epoxy resin (epofix from Struers). Hot mounting was avoided to prevent any thermal effects that might influence the polymer's morphology. Mounted samples were then grinded and polished with up to 1 µm diamond suspension. Cross-sections of welded joints were analyzed by SEM.

4.8.3. Failure mode analysis

To analyze the failure mechanism, a pressure-controlled FEI Quanta FEG 200 SEM from FEI Company was used in secondary electron mode and backscattering mode to get information about the failure mechanisms. SEM analysis was performed at pressure of

1.5 mbar, with 15 kV acceleration voltage in back scattering mode. In preliminary surface pretreatment investigations (§4.4), SEM observations were directly performed on the specimen without any particular preparation procedure, i.e. no conductive coating was used.

4.8.4. Joint area measurement

In order to calculate the joint strength, joint area was quantified using a dedicated experimental approach. After failure, macroscopic images of the joint area on both joining partners were obtained using a digital FUJIFILM X-Pro2 camera (Tokyo, Japan). Then, dimension of a single-pixel was measured using GIMP 2.10 software by correlating pixel size with a predefined scale positioned on the sample close to the joint area. Next, the joint area boarders were outlined and its area was calculated based on the number of pixels it contained. Using Lecia DM4000 microscope, polarized and stitched microscopic images of joint area were used to confirm the measurements in high resolution. In case of laser welding of Ti64 – PA6.6 optimization experiments, joint strength (MPa) was calculated based on the joint area that was conducted on PA6.6 after failure.

Chapter 5

5. Results

This chapter presents research results. It shows the effects of laser welding parameters on properties and performance of titanium to polyamide joints, and provides insights of preliminary investigations comparing the effects of aluminum plasma surface pre-treatment with that of laser ablation on surface properties and performance of laser-welded aluminum-polyamide joints. Then, it describes the influence of laser ablation parameters on joint behavior, surface properties, and interfacial thermal transfer.

5.1. Laser welding optimization DoE

In this section, results of Ti64 – PA6.6 laser welding DoE optimization experiments are illustrated. OFAT, screening and optimization DoE results, in addition to the evolution of welding defects along the process window, are discussed.

5.1.1. One Factor at A Time (OFAT)

Figure 34 (a) shows the effects of varying laser beam pulsing mode parameters, those are peak power (P_{peak}), pulse frequency (f_p) and duration (T_{pulse}), on joint's resistance to failure. Overlapping error bars indicate no significant variation in joint resistance to shear load at a constant average power (144 W). Thus, the laser mode was set to CW in DoE to reduce number of factors included in the design. Figure 34 (b) shows the effects of shielding gas type on the joint's resistance to failure. Results show insignificant effect of shielding gas type. However, argon shielding gas results in a lower deviation in the average shear load at failure, and was chosen for the DoE.

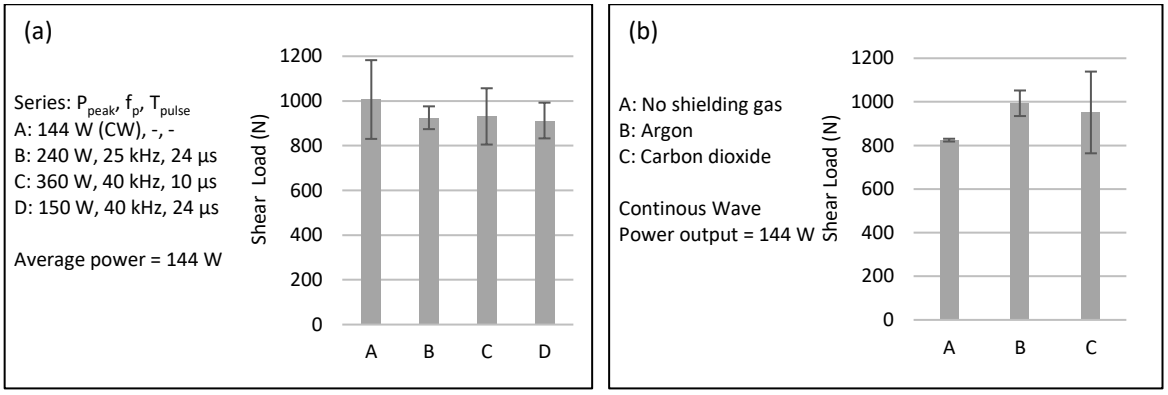

Figure 34: effects of (a) effects of pulsing mode and; (b) effects of shielding gas type on performance of laser wended Ti64 – PA6.6

5.1.2. Screening DoE

Pareto chart shown in Figure 35 (a) demonstrates the magnitude of effects for screened parameters. The effect of a single parameter illustrates the difference in mean shear load at the parameter's low and high values. The red line shows the effect size at 0.1 level of significance and is determined by Lenth's method [141]. Results show significance of laser power, wobble trajectory, defocus and wobble repetition, on the joint's resistance to failure. Main effect plot (Figure 35 (b)) demonstrates how a single factor influences the mean shear load. While speed does not show a significant response, it is important to note that Plackett-Burman design does not account for possible interactions between the

factors under investigation. A different design, e.g. full-factorial design, has to be used to analyze interactions between beam speed and laser power.

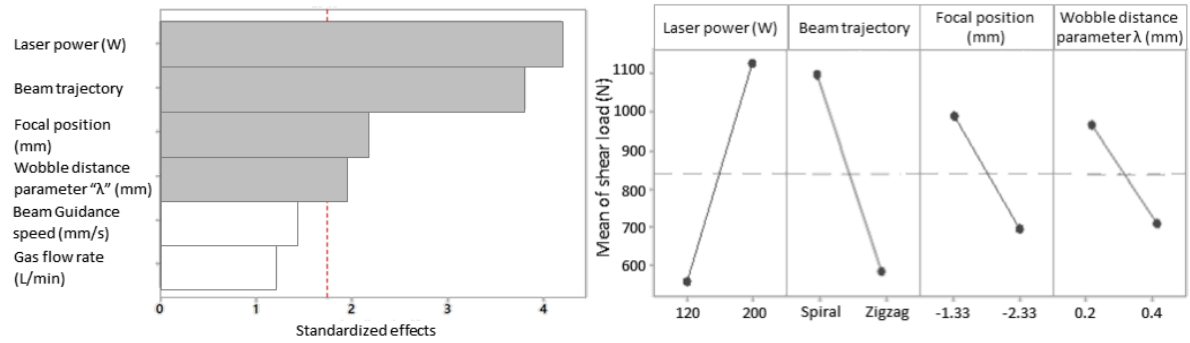

Figure 35: (a) pareto chart of effects where dashed line represents 0.1 level of significance; (b) main effect plot where dashed line presents average shear load

5.1.3. Optimization DoE

Focal position

Based on the screening results, it was decided to first optimize the focal position by varying the laser power density and controlling the laser power together with the focal position. Spiral wobble trajectory was chosen for its better response over zigzag alternative. The remaining significant parameters were kept unchanged as indicated in Table 13. Contour lines of contour plot, shown in Figure 36 (a), show nonlinear relation between focal position and joint strength, indicating maximum strength at a focal position near the titanium surface (z = 0), having beam spot diameter of 31 µm. The developed regression model (Equation 10) describes the relation between laser power, focal position, and joint strength. ANOVA F-tests results show, with 95% confidence, the significance of power (P), focal position (f) and non-linearity in both power (P^2) and focal position (f^2). No significant interaction was detected between both parameters. The developed model had R^2 value of 0.804, meaning that the model accounted for 80.4% of the variations in strength.

While shielding gas flow rate showed no significant effect on the shear load as indicated by the screening design, it exhibits significant effect on the joint quality as shown in the coloring of titanium in Figure 36 (b). Deducing gas flow rate decreases turbulence at the weld region, resulting in a stabilized plasma which prevents rapid oxidation of titanium [39], [142]. Thus, gas flow rate was reduced to 10 L/min in the upcoming optimization experiments.

Table 13: laser welding parameters of focal position optimization DoE

Beam guidance speed	Beam trajectory	Wobble distance parameter	Gas flow rate
V = 800 mm/s	Spiral	λ = 0.2 mm	Argon: 20 L/min

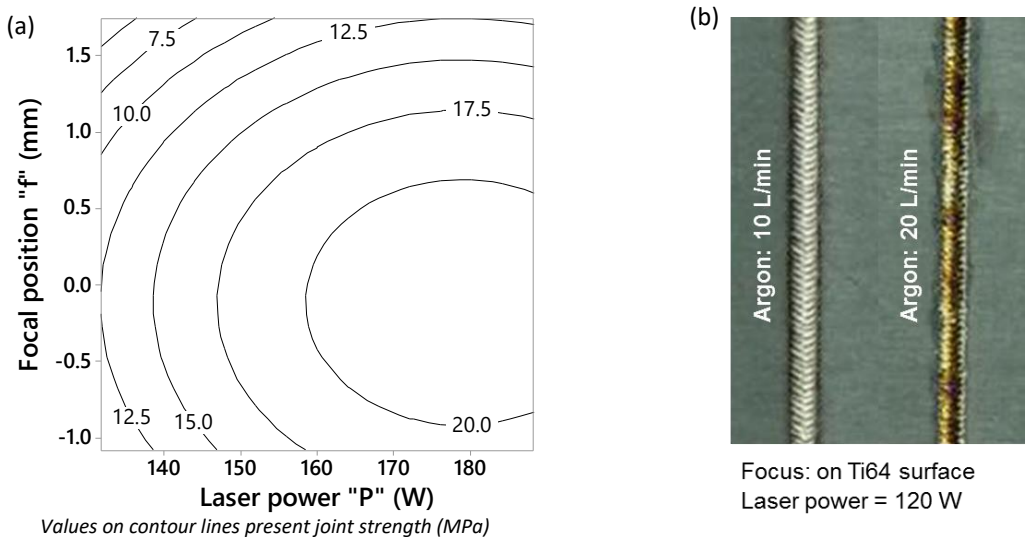

Values on contour lines present joint strength (MPa)

Focus: on Ti64 surface
Laser power = 120 W

Figure 36: (a) contour plot of joint strength verses focal position and laser power; (b) effect of gas flow rate on weld seam quality

$$Strength_{P,f} = -110.7 + 1.480\,P - 0.625\,f - 0.00414\,P^2 - 2.670\,f^2 \;\ldots\ldots\ldots\ldots\ldots\ldots\ldots\ldots\ (10)$$

Where:

$Strength_{P,f}$	predicted strength as a function of laser power and focal position (MPa)
P	laser power (W)
f	focal position (mm)

Beam guidance speed

After indicating the optimal focal position, additional optimization experiments were performed to expand the process window and determine possible interactions between laser power and beam guidance speed. Here, the laser beam was focused on titanium surface keeping the remaining parameters fixed, as indicated in Table 14, while reducing the gas flow rate to 10 L/min to avoid coloring of titanium. In order to examine a broad process window, fifteen combinations of parameters were tested as indicated by Figure 23 in §4.2.3. RSM results are shown in contour plot of Figure 37 (a), that is described by Equation 11, where P is the laser power (W) and V is the beam guidance speed (mm/s). ANOVA F-tests show, with 95% confidence, the significant effects of power (P), nonlinearity in power (P^2), and interaction between both variables (PV). However, relatively low significance of beam guidance speed V on joint strength is indicated with a P-value of 0.01. This model explains 63% of the variation in shear load (R2 = 0.63). It predicts a maximum strength of 23.9 MPa at 60 W and 900 mm/s. Using CCD design, a detailed RSM investigation was performed at the region of predicted optimum, and results are shown in Figure 37 (b). Results verify prediction showing maximum joint strength of 21 MPa at 60 W and 900 mm/s. This value is three times higher than existing values from the literature [42].

Table 14: laser welding parameters of beam speed optimization DoE

Focal position	Beam trajectory	Wobble distance parameter	Gas flow rate
0 mm	Spiral	λ = 0.2 mm	Argon: 10 L/min

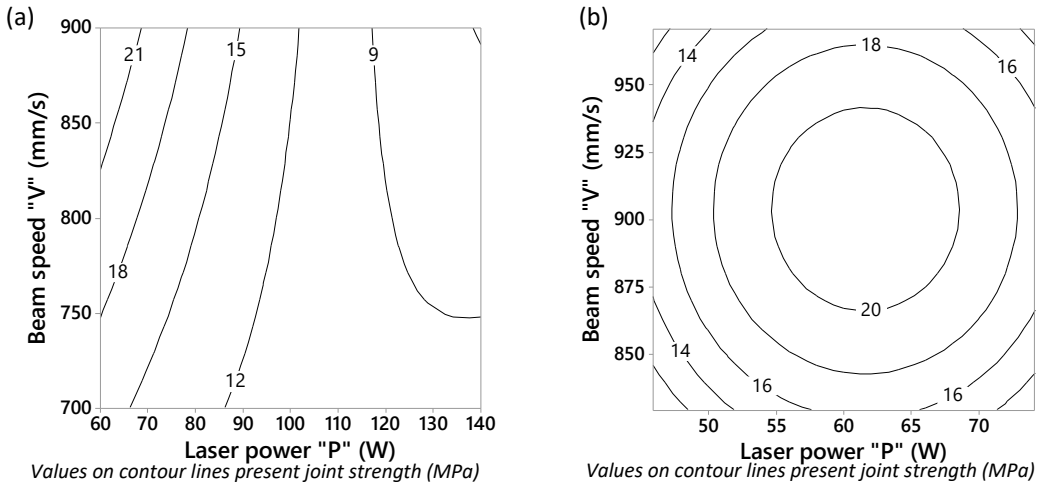

Figure 37: contour plot of shear strength verses laser power and beam guidance speed for: (a) complete process window; (b) detailed process window around region of optimal conditions

$$Strength_{P,V} = -24.5 + 0.139\,P + 0.0830\,V + 0.001517\,P^2 - 0.000742\,PV \ldots\ldots\ldots\ldots\ldots\ldots (11)$$

Where:

$Strength_{P,V}$	predicted strength as a function of laser power and beam speed (MPa)
P	laser power (W)
V	Beam speed (mm/s)

5.1.4. Weld defects

Evolution of weld defects

Samples welded with five different parametric combinations, that resulted in a broad range of joint strength, were chosen from the process window of Figure 37 (a) and investigated for welding defects. Table 15 shows the welding parameters, sequenced with respect to an increasing laser beam energy density, and illustrates the evolution of weld defects. Results indicate a strong correlation between increased laser energy density, growth of weld defects, and decline in joint strength. At high levels of energy density ($\gtrsim$ 5.5 J/mm2), weld pool cavities, flash defects, excessive penetration, and bubble formation are observed. High thermal input causes excessive heat penetration through the titanium thickness. This can cause polymer degradation, which would generate gaseous products, and force the humidity inside the polymer to evaporate creating high internal gaseous pressure. This pressure results in the formation of voids and bubbles, and potentially expulsion of molten polymer out of the weld joint, as indicated by the flash defect, or through blow-out cavities in the weld pool. Welding deflection increased along with increased energy density, except for parameter 5 which resulted in lower deflection than parameter 4. This can be explained by the localized stress relief points created by weld pool cavities during the laser welding process using parameter 5. However, this reduced deflection correlates with an increase in strength for parameter 5 compared to 4. This might be explained by the extra anchoring points formed between the polymer and blow-out holes.

Table 15: evolution of laser welding defects in Ti64 – PA6.6 joints showing the regions illustrated in §4.8.1

Parameter	1	2	3	4	5
Laser power (W)	60	60	80	120	140
Beam speed (mm/s)	900	700	900	900	700
Energy density (J/mm²)	2.7	3.5	3.7	5.5	8.2
Average strength (MPa)	21.19 ± 1.56	18.38 ± 0.44	19.01 ± 1.30	11.64 ± 3.40	15.05 ± 4.40
Weld pool cavities					
Flash defect	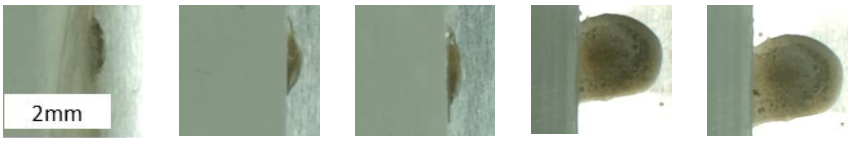				
Excessive penetration					
Bubbles and voids					
Average deflection (°)	0.22 ± 0.17	0.59 ± 0.11	1.15 ± 0.28	1.20 ± 0.41	0.89 ± 0.47

Welding induced deflection

Welding deflection is a critical defect in laser welding Ti64 – PA6.6 as it can result in a complete failure of the joint by peeling during cooling down of the weld seam. Welding induced deflection was analyzed for all samples involved in RSM shown in Figure 37 (a). Figure 38 (a) shows contour plot demonstrating effects of laser power and beam guidance speed on welding induced deflection as described by Equation 12. ANOVA analysis demonstrates significant linear (P) and nonlinear (P^2) response of the laser beam power, as well as interaction (PV) between both parameters on the resulted deflection. Although the speed (V) parameter is included in the model, F-test results demonstrated that it does not have a significant effect on the response.

Results show an increase in deflection along with increased laser power and decreased beam speed. Figure 38 (a) and Figure 38 (b) show high correlation between increased welding induced deflection angle and deterioration in joint strength. However, the high variability in results (R^2 = 54.2%) contributes to reducing the magnitude of Pearson correlation coefficient (r = -0.67) between deflection angle and joint strength. At some welding conditions, this defect resulted in significant peeling stresses causing some of the welded joints to fail while handling or cooling down after the welding process. Those welding conditions exhibit a minimum deflection angle of 1.02°. Thus, a threshold of 1° deflection is considered as an upper limit for a robust joint. Figure 38 (b) shows the combined contour plot with the robust process window.

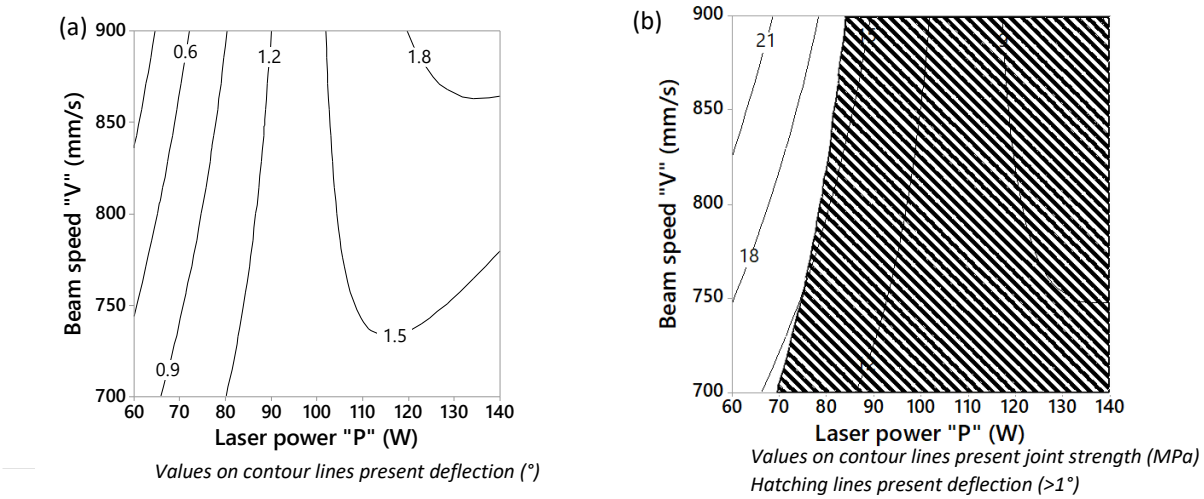

Figure 38: (a) contour plot of welding induced deflection verses beam speed and laser power; (b) combined contour plot of joint strength and welding induced deflection showing robust process window (un-hatched)

$$Deflection = 4.19 - 0.0008\,P - 0.00865\,V - 0.000275\,P^2 + 0.000087\,PV \quad \ldots\ldots\ldots\ldots\ldots\ldots\ldots\ldots (12)$$

Where:

$Deflection$	predicted welding induced deflection angle (°)
P	laser power (W)
V	beam speed (mm/s)

5.1.5. Summary and conclusion

The influence of laser welding parameters on the strength and quality of Ti64 – PA6.6 joints was investigated. Preliminary results show no significant effects of laser pulsing mode and shielding gas type on the joint's resistance to failure. Screening results outlined significant influence of laser power, focal position, wobble distance parameter and geometry on the joint strength, favoring a spiral wobble trajectory and a shorter wobble distance parameter with 0.2 mm gap between consecutive wobbles. Statistically strong mathematical model was generated describing the influence of laser beam power and focal position on joint strength. Both variables demonstrate strong influence favoring focal position on titanium surface (spot size of 31 µm). Another model describing effects of beam guidance speed and laser power on joint strength was generated. Although the influence of beam guidance speed is not significant, ANOVA analysis shows its significant interaction with laser beam power and a significant effect of laser power. Results outline optimal joining conditions at 2.7 J/mm², following 8 mm wide spiral wobble trajectory with 0.2 mm gap between consecutive wobbles, under the shielding of argon gas at a flow-rate of 10 L/min. The resulting joint strength is 21 MPa, close to the value predicted by regression model (23 MPa).

Weld defects, in particular weld pool cavities, flash defect, excessive penetration, bubbles and voids, were highlighted and welding induced deflection was quantified. Results show the evolution of defects along with increased energy density of the welding process. The formation of bubbles and voids and the extrusion of molten polymer out of blow-out holes and/or flash defects during a thermally intensive welding process ($\gtrsim$ 5.5 J/mm²) suggest rapid expansion of molten polymer during the laser welding process. A mathematical model, developed to describe the effects of laser power and beam guidance speed on welding induced deflection, indicates a strong interaction between both laser welding parameters. Inversely proportional correlation between welding induced deflection and

joint strength is observed, demonstrating influence of peeling induced forces on joint failure, and indicating an upper threshold of 1° for a robust joining process. Optimized laser beam conditions resulted in a high strength, robust, and defect-free joint (gap 1).

5.2. Surface pretreatments preliminary investigations

In this section, results of plasma and laser ablation pretreatments preliminary investigations are shown. The effects of surface pretreatments on surface energy, composition, and topography, are illustrated, and correlations with failure behavior and joint performance are discussed.

5.2.1. Surface energy

Influence of plasma exposure time

In order to determine the plasma treatment time and to set up the DoE levels, WCA measurements were performed on the treated surfaces as a function of treatment conditions. It can be concluded from Figure 39 that plasma treatment time increases the water wettability significantly. In case of Al1050, it is shown that wettability increases with plasma exposure time, and a saturation effect was observed for plasma treatment time above 24 s. To include a relevant "mid-value" of the plasma treatment time in the DoE (§4.4.1), a mid-value of WCA, between the saturated WCA of plasma treated Al1050 and initial WCA of the solvent cleaned Al1050, was selected at 3 s treatment. In case of PA6.6, it is shown that wettability increases with plasma exposure time, and a saturation effect was observed above 60 s. A maximum plasma treatment time of 60 s was chosen in order to prevent possible surface deterioration of polymer which might have a negative effect on the joint quality as reported by Arai et al. [34]. 13s was used for the mid-value.

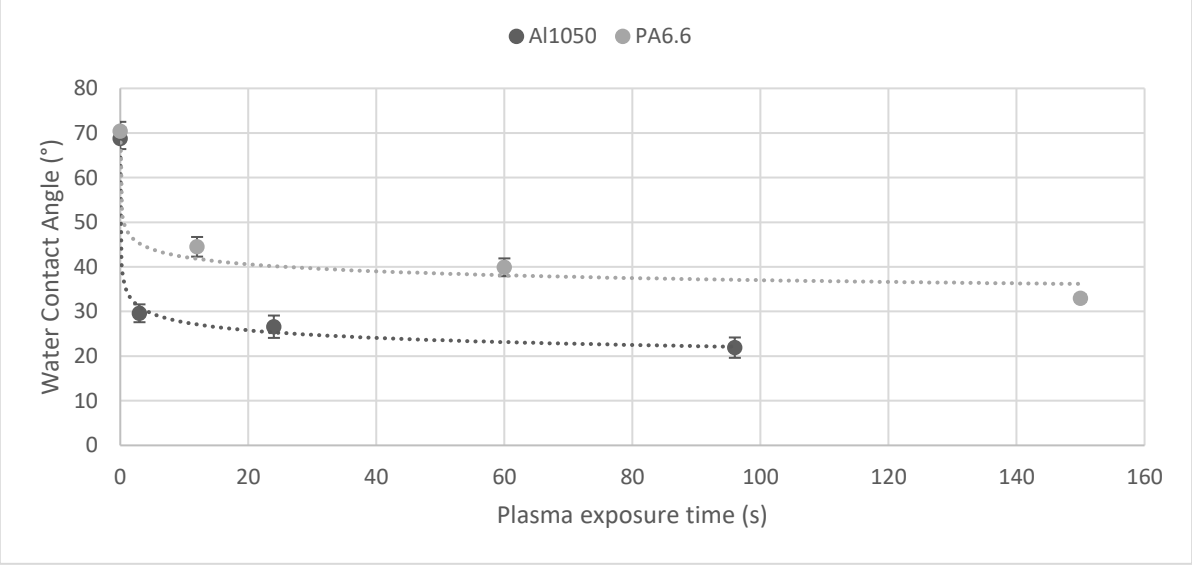

Figure 39: influence of plasma pre-treatment time on Water Contact Angle.

Surface energy

Figure 40 shows the effect of plasma surface pretreatment technique on Water Contact Angle (WCA) and surface energy (SE). It is clearly shown that plasma treatment of Al1050 and PA6.6 increases their water wettability, which indicates an increase in the surface

energy, in particular the polar part. The same is observed for Al1050 after laser ablation, where water and diiodomethane perfectly wets the surface (contact angle less than 5°), indicating an even greater increase in surface energy compared to plasma treatment. For comparison purpose, those WCA and SE values are obtained from measurements performed 3h after the last step of surface treatment, as it corresponds to the time of laser assembly after surface pretreatments. Contact angle measurements and surface energy calculations for the treated samples are according to OWRK method (see §4.6.2) using values provided in Table 12.

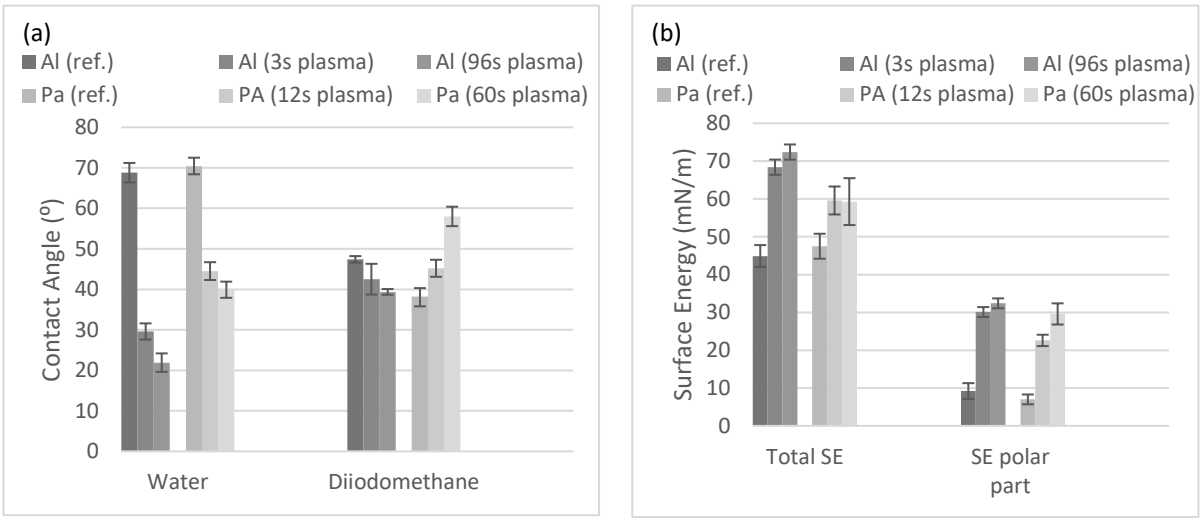

Figure 40: influence of plasma surface pretreatment on (a) water and diiodomethane contact angle and; (b) total surface energy (SE) and its polar part

Aging of treatment

In the case of plasma-treated aluminum, it is observed that WCA increases as a function of aging time when the Al sample is kept in lab conditions. This phenomenon was already observed by Strohmeier [143] and is assigned to the adsorption on the aluminum surface of hydrophobic airborne carbon species. This phenomenon, called recontamination, is further quantified by measuring the evolution of surface energy as a function of Al1050 storage time after long plasma treatment (Figure 41). In the case of plasma-treated PA6.6, calculated surface energy revealed hydrophobic recovery as a function of aging time as shown in Figure 42. No increase of WCA value is observed for laser-ablated aluminum samples for storage times reaching up to one week.

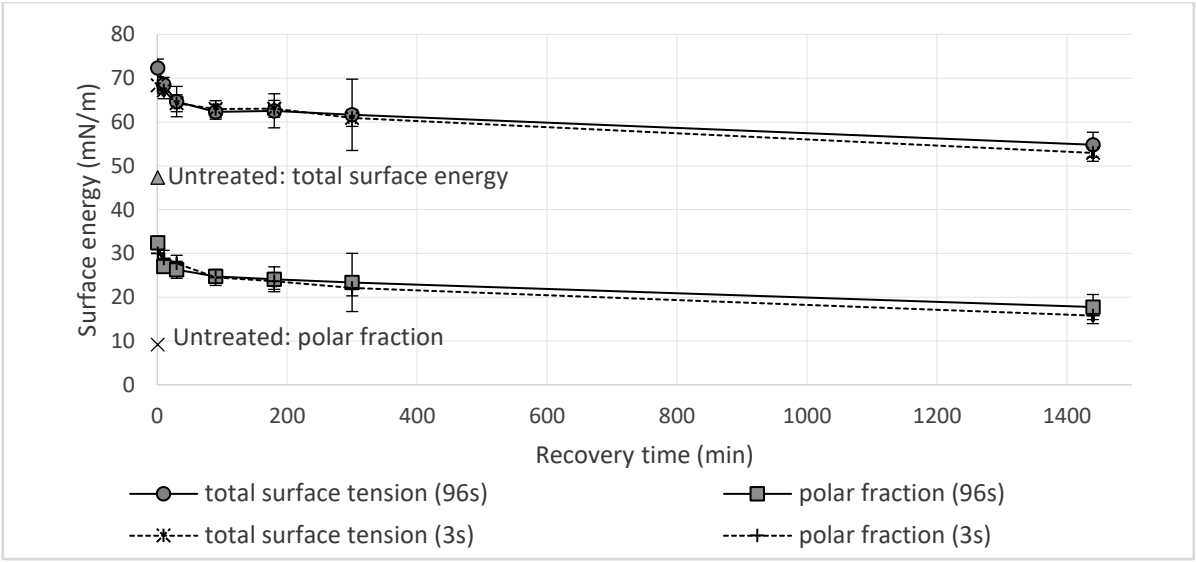

Figure 41: recontamination effect on surface energy of 3s and 96s plasma-treated Al1050

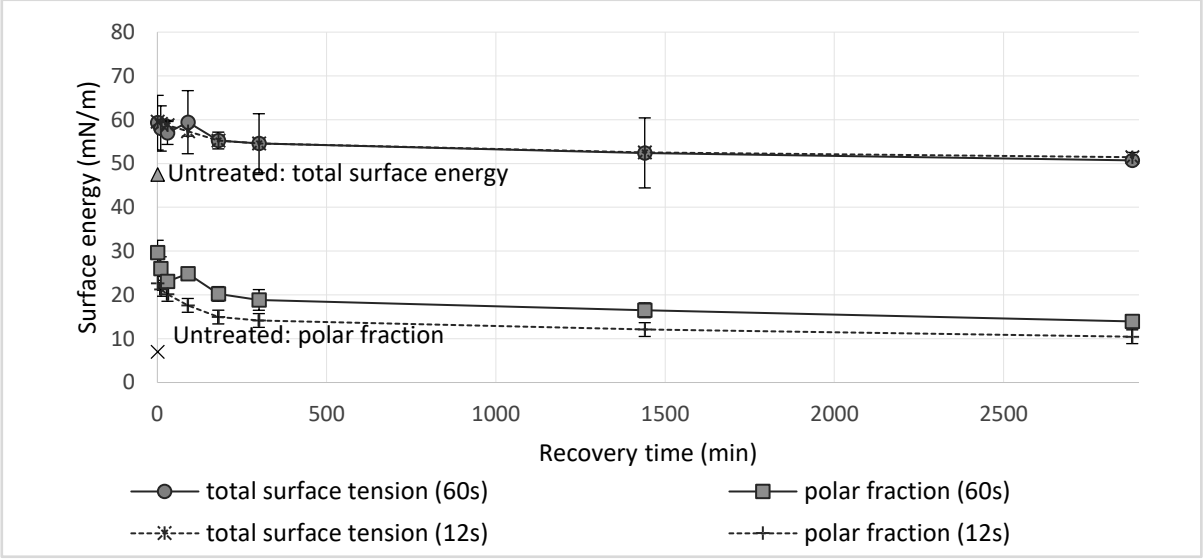

Figure 42: hydrophobic recovery of 12s and 60s plasma-treated PA6.6

5.2.2. Surface composition

XPS analysis was performed only on the aluminum sheets before and after treatment. The results are presented in Table 16. Fluorine is certainly a contamination from the analysis chamber and will no longer be discussed. Both Surface treatments (plasma and laser ablation) lead to a surface that is richer in oxygen and poorer in carbon. However, this change is more pronounced for laser-ablated Al1050, where much lower content of metallic aluminum is detected. This is certainly assigned to the laser ablation process' surface oxidation effect, so that more oxygen is present, and "cleaning" effect, thereby decreasing the presence of adventitious carbon. The slight increase in oxygen content regarding the 3s treatment compared with the reference sample is probably correlated with the non-significant increase of shear load. The increase in N content is low for plasma-treated Al and can be assigned to the contact with activated species in the nitrogen-rich plasma. N content of laser-ablated sample is very low, probably due to the presence of a large oxide layer on the surface. Surface composition of plasma-treated Al1050 (96s) is comparable to that of laser-ablated Al1050.

Table 16: XPS results showing surface composition of treated Al samples

Sample	% Al	%O	%C	% N	% F	% Al metal
Al-ref (0s)	29.88	46.89	17.15	1.29	4.79	25.98
Al-plasma (3s)	26.98	48.62	21.43	1.46	1.51	26.21
Al-plasma (96s)	25.75	55.04	12.31	1.47	5.43	23.73
Al-laser ablation	31.59	58.07	9.98	0.36	0.00	1.97

5.2.3. Surface topography

Respectively, the effects of surface treatments on the surface topography of Al1050 and PA6.6 are shown in Figure 43 and Figure 44. It is clearly shown that plasma surface treatment did not result in a significant change in the surface topography of both Al and PA. However, laser ablation has significantly increased the surface roughness resulting in a total increase of 11% of the calculated surface area with respect to the projected surface area. Such interpretation was calculated using the Sda% roughness parameter. Such an increase in roughness is expected to enhance the joint strength by increasing the total surface area of contact between both materials providing more anchoring points for prospective chemical bonding, and possibly providing anchoring points for mechanical interlocking.

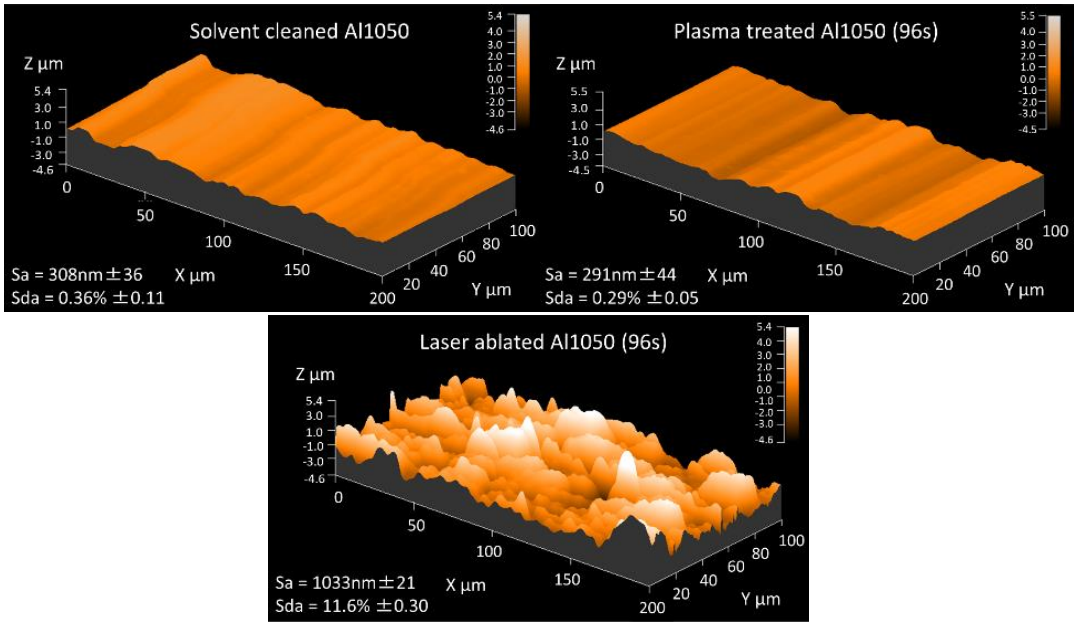

Figure 43: 3D topography of treated aluminum surface

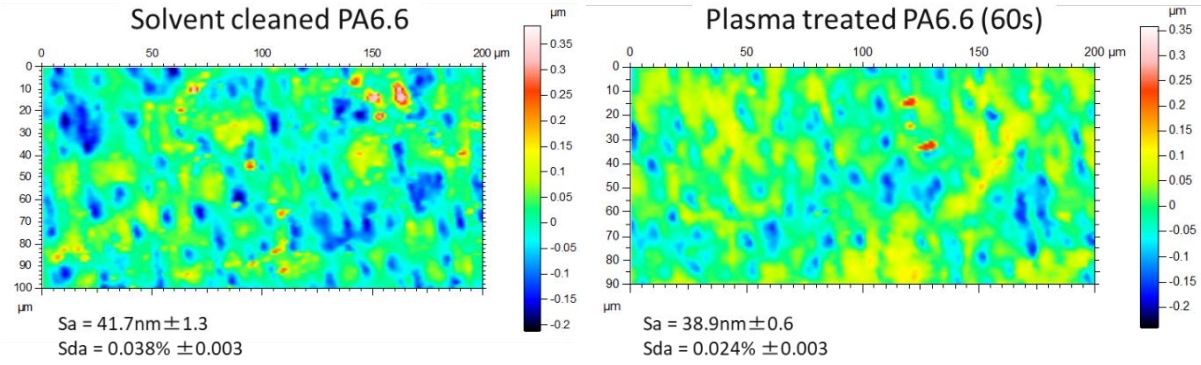

Figure 44: "false color" 3D topography of treated polyamide. Color code represents Z axis

5.2.4. Joint resistance to failure

Full-factorial DoE results were analyzed using a response surface method [144], with the aid of Minitab software. Contour plot results (Figure 45) show positive effects of increasing plasma treatment time of Al1050 and a nonlinear response of PA6.6 treatment time resulting in a predicted maximum of 1635 N at 96 s and 39 s plasma treatment time for Al1050 and PA6.6, respectively. ANOVA analysis indicates no significant interaction between aluminum and polyamide treatment times, and a larger influence of polyamide treatment time than that of aluminum. Nonlinear response of polyamide plasma treatment time suggests surface deterioration of the polymer at high treatment times. The insignificant factors were eliminated from the newly generated model shown in Equation 13 (in un-coded units). $R^2 = 38.6\%$ value shows that the model explains only 38.6 % of the variability of the response data around its mean. On the other hand, a significantly low p-value = 0.00 of the regression model interprets the model's high accuracy but low precession of predictability.

Interval plot (Figure 45) illustrates the mean value of the maximum shear load (N) with respect to the different treatment parameters, including laser-ablated samples. Overlapping standard errors bars indicate that the difference between the means is not statistically significant. To ensure statistically significant difference between the means, a T-test assuming equal variance was used in calculating the p-value between each two set of samples. By considering the solo effect of plasma treatment of Al1050 on the joint strength (i.e. keeping the PA6.6 surface treatment constant), it can be interpreted from the results that Al1050 plasma treatment time did not yield a significant increase in shear load compared to its non-treated alternative, as much as PA6.6 plasma treatment keeping constant Al1050 treatment time. It is important to note that the p-value calculated for the DoE model, which indicates the significance of the Al treatment, is comparing the shear load's mean value of all the data set (including different treatment conditions for PA) involving no Al plasma treatment, with those involved in Al plasma treatment. meaning, the combined mean value of (0,0), (0,12), and (0,60) is compared to that of (96,0), (96,12), and (96,60).

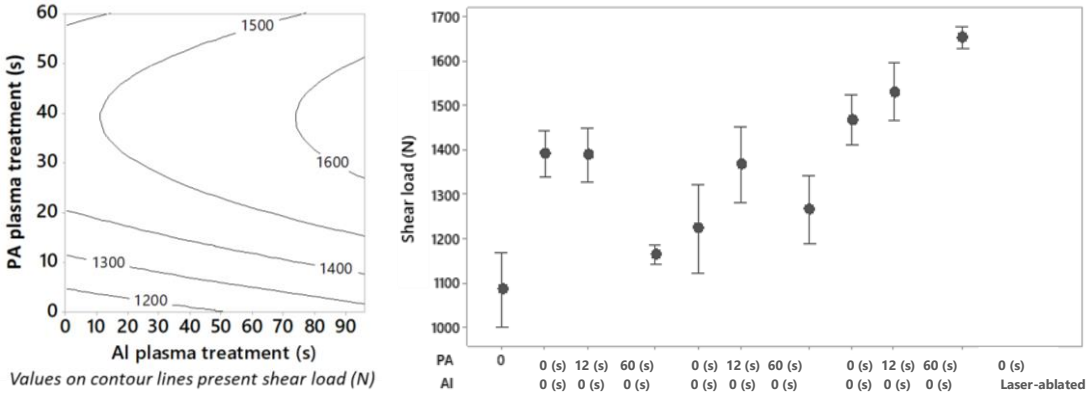

Figure 45: (left) contour plot of plasma treatment; (right) interval plot of surface pretreatments

$$Shear\ load\ = 1119.3 + 1.591\ Al + 18.63\ PA - 0.2389\ PA^2 \ \ldots\ldots\ldots\ldots\ldots\ldots\ldots\ldots\ldots\ldots\ldots\ldots \ (13)$$

Where:

$Shear\ load$	predicted shear resistance to failure (N)
Al	aluminum plasma pretreatment time (s)
PA	polyamide plasma pretreatment time (s)

5.2.5. Failure mode analysis

SEM analysis was performed on Al1050 and PA6.6 at the welded joint zone after failure in order to understand the failure behavior. In all welded combinations, aluminum surfaces show zones which corresponds to three different “locus of failure” at the joint interface, and are referred to as 1, 2, and 3 as indicated on the plasma-treated Al1050 surface shown in Figure 46. EDX analysis results of those regions are given in Figure 47, and regions of investigation are elaborated in Figure 69 (Appendix A).

While region 1 represents adhesive failure zone in plasma-treated aluminum and out-of-weld zone close to the joint area in laser-ablated aluminum, EDX analysis of the zones 2 and 3 shows that they consist of relatively thin polyamide layer and relatively thick polyamide layer, respectively, on both treated aluminum surfaces. The presence of a layer of polyamide on aluminum confirms a cohesive failure zone. Larger area of thick residual polyamide is noticed on the plasma-treated aluminum (96 s) with respect to reference aluminum. 45º strips of polyamide are visible only on the plasma-treated aluminum. It is assumed that those strips are a result of deformation taking place first in the polyamide bulk, referred to as "shear banding deformation", and propagating to the Al1050 – PA6.6 interface. Regions of adhesive failure are noticed at the weld region in between thick polyamide residue lines on both reference and plasma-treated aluminum. However, visual inspection shows larger regions of cohesive failure on joints where both aluminum and polyamide are treated with 96 s and 60 s, respectively. EDX results show larger carbon content at region 2 in laser-ablated aluminum than that of plasma-treated aluminum. Laser-ablated Al1050 demonstrates relatively high carbon content in all its regions of failure, which confirms fully cohesive failure mode.

In the case of reference polyamide welded to laser-ablated aluminum, two zones (a and b) can be identified as equal in area and matching in geometry on both joining partners. Region “a” corresponds to high density of polyamide residues on ablated aluminum after failure, and rough pits are noticed on polyamide at region “b” where traces of aluminum particles can be found in relatively high distribution densities, particularly at the edges of the joint. This suggests that failure at region “b” is closer to the interface than failure at region “a”, resulting in a mixed cohesive failure mode where residues of both partners can be found on one another. However, aluminum traces are rarely seen with other Al treatments. It is suspected that those aluminum traces are either a result of aluminum oxide dust, trapped on the rough surface, or due to the random geometry of aluminum oxide peaks which might lead to their detachment from the aluminum surface during the shear test. Optical and microscopic inspections revealed similar failure behavior in all similarly pretreated joints.

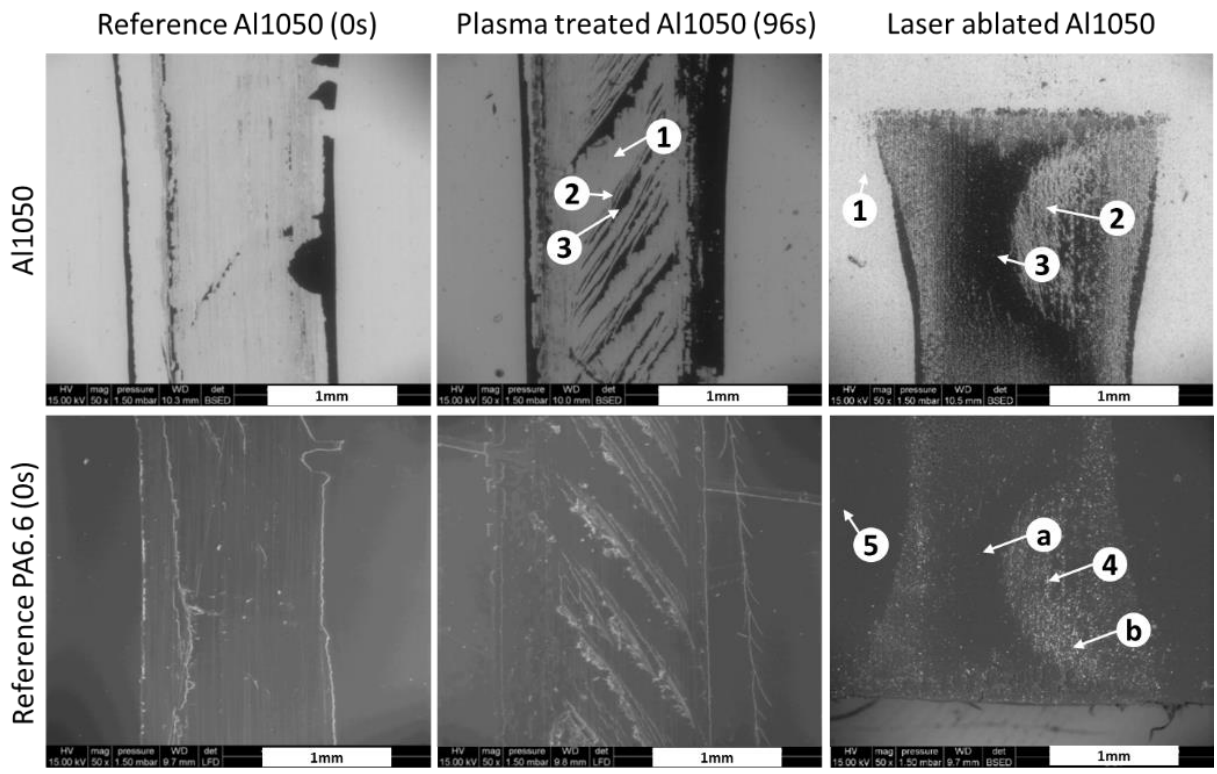

Figure 46: SEM showing failure zone of differently pretreated Al1050 welded to PA6.6

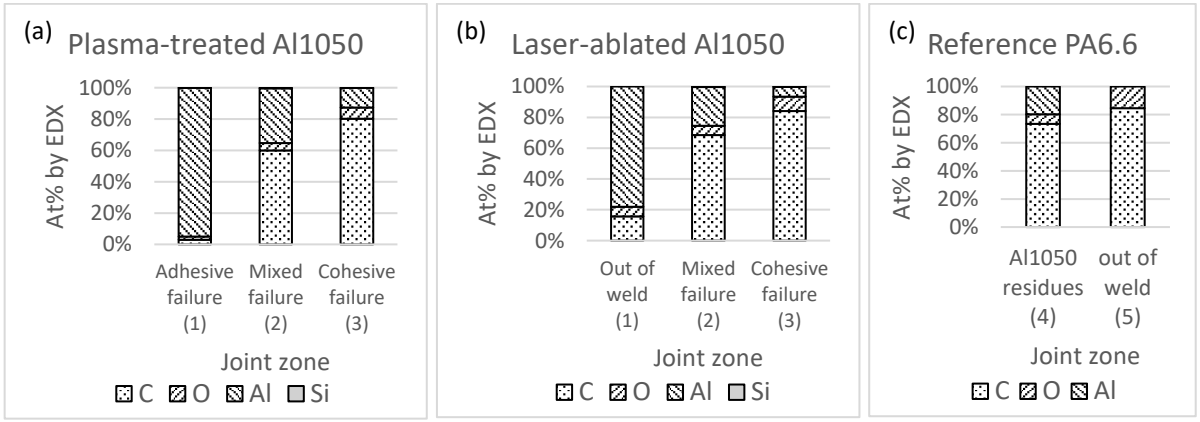

Figure 47:EDX results showing elemental composition of zones on Al1050 (a and b) and PA6.6 (c) in case of (a) plasma-treated Al1050; (b and c) laser-ablated Al1050

5.2.6. Summary and conclusion

Significant improvement in shear resistance to failure of laser-welded Al1050 – PA6.6 joints is recorded after plasma pretreatment. Improvement in joint performance is not related to changes in surface topography, but rather to chemical modifications of pretreated aluminum surface. Moreover, plasma pretreatment of polyamide and of both joining partners is also effective in improving joint resistance to shear load. This improvement is correlated with an increase in surface energy of pretreated surfaces, in particular the polar part, in agreement with the adsorption theory of bonding (§2.2.2). These results confirm that an improvement of LAMP joint resistance to failure can certainly be achieved without an increase of interfacial interlocking.

When aluminum surface composition and topography are changed due to laser ablation, the improvement in joint performance is larger than in the case of plasma pretreatment. This is assigned to additional strengthening effects related to the high increase in oxidized aluminum, roughness amplitude, interfacial bonding area, and surface wettability, resulting in a fully cohesive failure mode (gap 2).

5.3. Laser ablation DoE

Laser ablation process already demonstrated its adhesion promotion potential in laser-welded Al1050 – PA6.6 joints. This section shows the influence of laser ablation parameters on performance of laser-welded Al1050 – PA6.6 and Ti64 – PA6.6. Screening DoE results highlight the significant laser ablation parameters. Optimization results outline the process window, model the response, and optimize the process in terms of maximizing the joint's resistance to shear load.

5.3.1. Screening

Al1050 – PA6.6

Laser ablation screening design results in several ablation morphologies including patterned, semi-patterned, and stochastic geometries (Figure 48). Microscopic investigations show that all laser-ablated samples result in cohesive failure mode regardless of the ablation parameters. Figure 49 shows screening design results, represented in a Pareto chart which shows the magnitude of effects of screened parameters, and in the main effects plot of significant parameter. The effect of a single parameter in the pareto chart illustrates difference in mean shear load at the parameter's high and low values. The dashed line, determined by Lenth's method [141], shows the effect size at 0.05 level of significance. Results recognize pulse frequency to have statistically significant effect on joint resistance to failure, identifying significance of PPP and overlap ratio (see §4.4.2). Main effect plot describes how changes to a single factor influences mean shear load. Results show that a high level of pulse frequency, reflecting an increase in overlap ratio and a decrease in PPP, enhances the joint's resistance to failure.

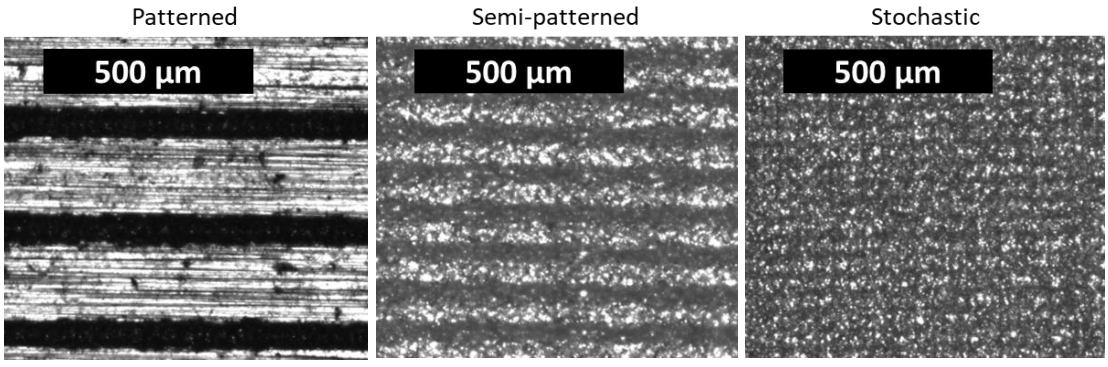

Figure 48: surface morphology of ablated Al1050 resulting from screening DoE

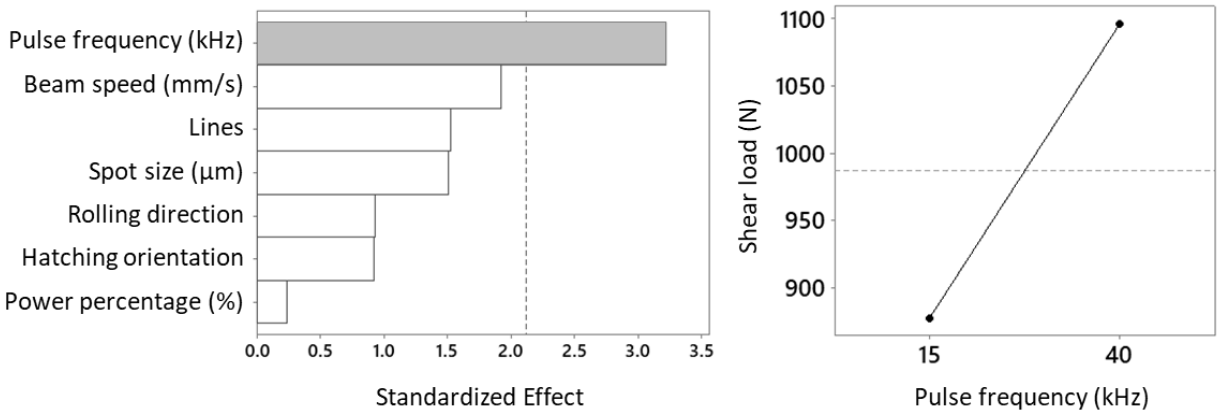

Figure 49: (left) Pareto chart of effects, where dashed line represents 0.5 level of significance; (right) main effects plot of significant parameters of Al1050 ablation where dashed line presents average shear load

Ti64 – PA6.6

Laser ablation screening results of titanium show similar ablation morphology as laser ablation of aluminum, i.e. patterned, semi-patterned, and stochastic. However, some parametric combinations result in a shiny titanium surface, similar to a polished appearance, as shown in Figure 50. This effect, titled as "polished" is only achievable at relatively high pulse frequency (120 kHz) and low PPP (5 kW). Microscopic investigations show mixed cohesive/adhesive failure mode in case of polished titanium surface. However, all other ablated titanium samples demonstrate a completely cohesive failure mode. Pareto chart (Figure 51) shows magnitude of effects of screened parameters, with dashed line underlining effect size at 0.05 level of significance. Similar to the case of aluminum ablation, results identify only pulse frequency to have a significant impact on the joint's resistance to failure, signifying effects of PPP and overlap ratio. Here, main effects plot shows that a low level of pulse frequency is favored to increase the shear load. However, this result is influenced by the relatively low joint resistance to failure of polished titanium, which is ablated at 120 kHz. Since pulse frequency influences both overlap ratio and PPP, and given that beam speed only influences overlap ratio, it was decided to proceed with the optimization process by simultaneously varying beam speed alongside pulse frequency to gain better control over the process variables.

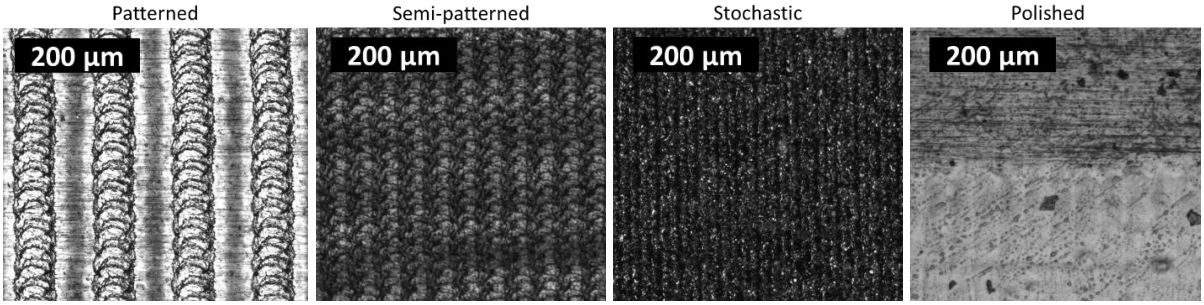

Figure 50: surface morphology of ablated Ti64 resulting from screening DoE

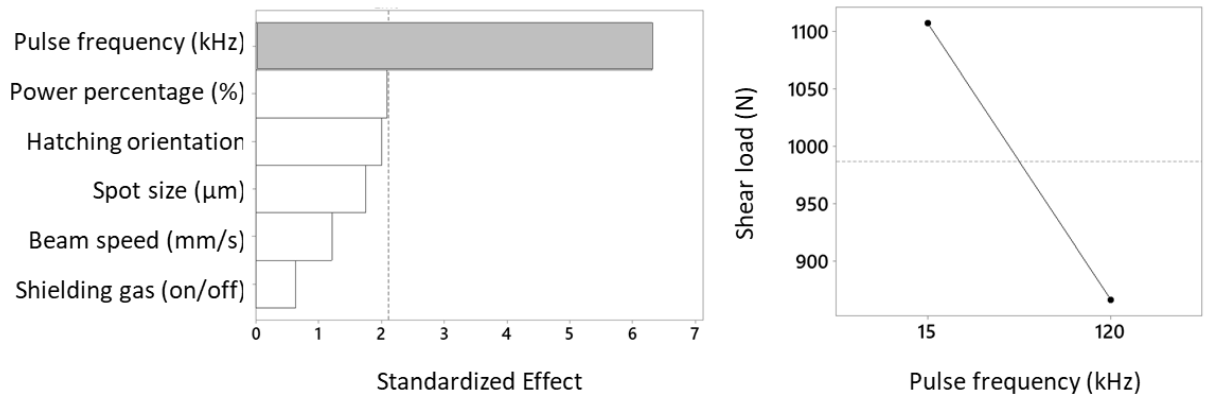

Figure 51: (left) Pareto chart of effects where dashed line represents 0.5 level of significance; (right) main effects plot of significant parameter of Ti64 ablation where dashed line presents average shear load

5.3.2. Optimization

Al1050 – PA6.6

During optimization experiments, pulse frequency and beam speed were simultaneously varied to create a predictive model describing the response, while keeping constant setup of insignificant factors as indicated in Table 17. Figure 52 (a) shows contour plot of developed predictive model (Equation 14), in terms of pulse frequency "f_p" (kHz) and speed "V" (mm/s). ANOVA analysis reveal high reliability of the model and the significance of its coefficients at 0.05 level of significance. Significant influence of pulse frequency (f_p) and beam speed (V) indicate significant influence in both, PPP and overlap ratio. The non-linear response of beam speed (V^2) outlines the region of highest predicted joint resistance to shear load (>1400 N) between overlap ratio of 60% and 75%, as shown in the contour plot. Since the maximum achievable pulse frequency of the laser ablation machine in use is 120 kHz, process window was further expanded by lowering PPP through reducing power percentage while keeping overlap ratio (≈ 68%) of the predicted optimal setting (120 kHz and 1750 mm/s) unchanged. Results of this last optimization step show maximum joint resistance to failure at calculated PPP of ≈ 4.75 kW, achieving a maximum average shear load of 1465 ± 65 N. However, it is important to note that other maximums are also expected along laser ablation process window, and the stated "optimal" is only with regards to the investigated design space.

Table 17: fixed parameters settings during laser ablation optimization (Al1050)

Power (%)	Spot size	Hatching	Lines	Rolling
100	45 µm	Perpendicular	Off	Axial

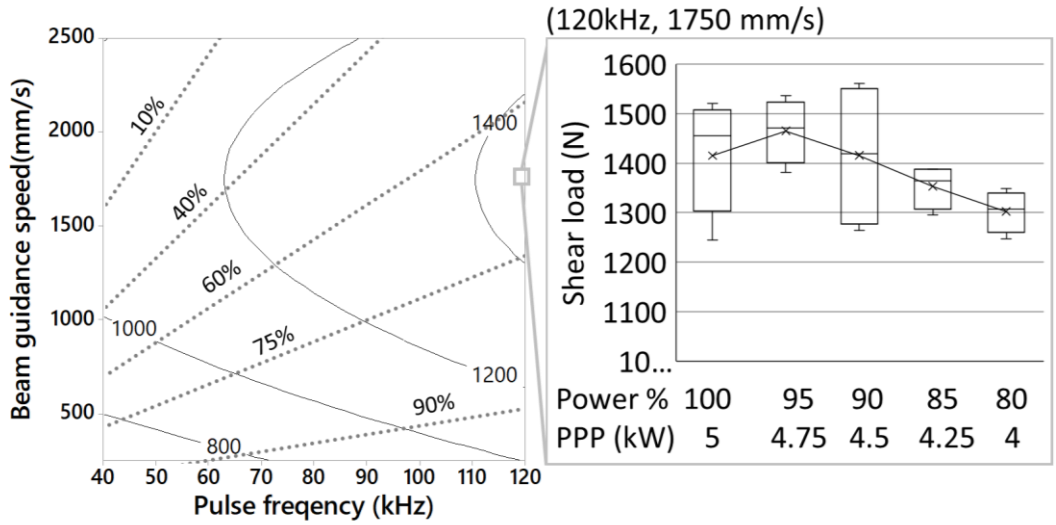

Values on contour lines present Shear load (N)
Dotted lines present overlap ratio

Figure 52: results of laser ablation optimization (Al1050)

$$Shear\ load = 343.7 + 4.3\ f_p + 0.68\ V - 0.00019\ V^2 \ \ldots\ldots (14)$$

Where:

$Shear\ load$	predicted shear load at failure (N)
f_p	pulse frequency (kHz)
V	beam guidance speed (mm/s)

Ti64 – PA6.6

Same as in the case of aluminum laser ablation, pulse frequency and beam speed were varied simultaneously to model the response. The remaining parameters were kept constant as shown in Table 18. Preliminary full factorial design (15 – 40 kHz, 150 – 650 mm/s) was excluded from RSM, as some of the ablation parameters result in high deflection and curvature in the titanium samples ablated at relatively high overlap ratio and PPP. This forms a gap between the metal and polymer during the welding process, and prevents the welding process. Contour plot of Figure 53 describes the regression model (Equation 15) generated along the robust process window. ANOVA analysis shows high accountability of the model (coefficient of determination $R^2 = 93.8\%$) and significance of its coefficients ($p\text{-value} < 0.05$), in particular: beam speed (V), and significant non-linearity in its response (V^2), with no significant impact of pulse frequency (f_p) and no interaction between pulse frequency and speed. This signifies the influence of overlap ratio and the non-linearity in its response. Dashed lines on contour plot demonstrate resulted overlap ratio across investigated process window. Significant correlation between overlap ratio and contour lines, indicates its significant effect on the joint's resistance to failure. Regression model predicts a maximum shear load of 1222 N at 43.89 kHz and 364.15 mm/s, which corresponds to an 82% overlap ratio.

Process window was expanded in two directions as described in §4.4.2 – one along the path of steepest ascent up to -790% overlap ratio (patterned structure), and the other by varying PPP at predicted optimal overlap ratio. Results of process window expansion are shown in Figure 54. Along the path of steepest ascent, a slight increase of joint's resistance

to failure followed by slight decrease is noticed. At a constant overlap ratio of 82%, reducing PPP from 60 kHz to 15 kHz slightly increases the joint's resistance to shear load, followed by a sharp drop at PPP of 5 kW. Results show the highest average bearable shear load (1201 ± 35 N) at a pulse frequency of 30.28 kHz and a beam speed of 5520.5 mm/s. However, parametric conditions at 34.17 kHz and 3772.82 mm/s (PPP = 44.5 kW and O = -145%) result in the smallest deviation in joint resistance to failure (1187 ± 11 N), and are identified as the optimal ablation conditions.

Table 18: fixed parameters settings during laser ablation optimization (Ti64)

Power %	Shielding gas	Hatching	Spot size
100	off	perpendicular	45 µm

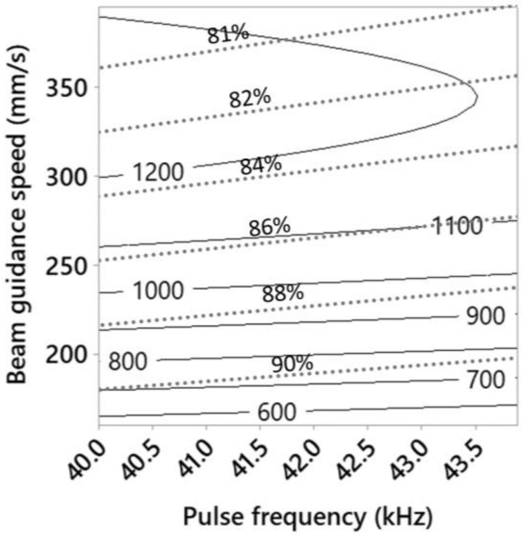

Values on contour lines present shear load (N)

Figure 53: contour plot of laser ablation optimization (Ti64)

$$Shear\ load = -654 - 11.6\ f_p + 13.71\ V - 0.01993V^2 \ \ldots\ldots\ldots\ldots\ldots\ldots\ldots\ldots\ldots\ldots\ldots\ldots\ (15)$$

Where:

$Shear\ load$	predicted shear load at failure (N)
f_p	pulse frequency (kHz)
V	beam guidance speed (mm/s)

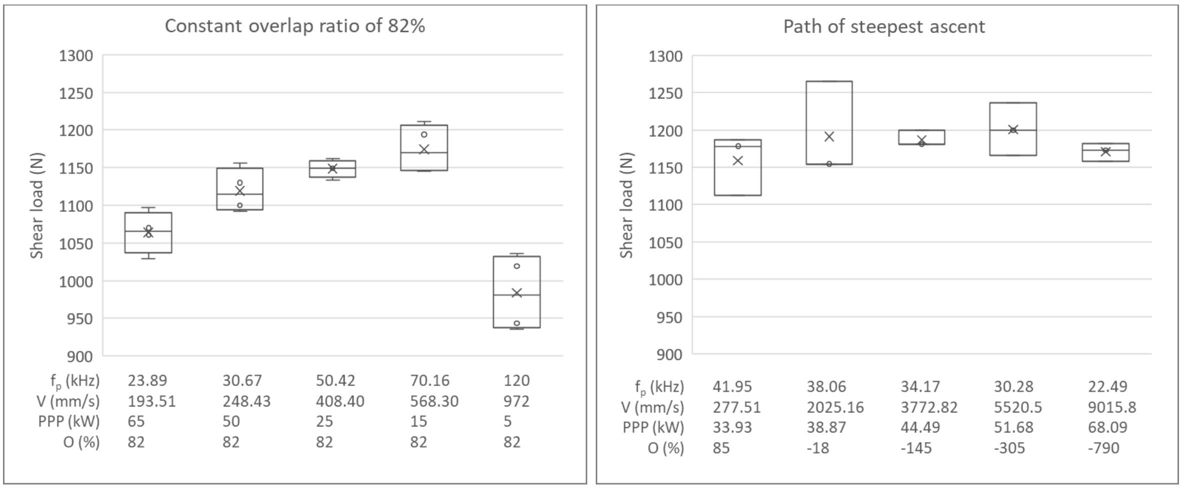

Figure 54: expanding process window along: (left) 82% overlap ratio; (right) path of steepest ascent

5.3.3. Summary and conclusion

A DoE was developed to investigate the influence of short-pulsed laser ablation parameters on the performance of laser-welded Al1050 – PA6.6 and Ti64 – PA6.6 assemblies. Screening results highlight the significant influence of pulse frequency on the joint's resistance to failure, marking the importance of both PPP and overlap ratio. Effects of pulse frequency and beam speed on joint performance were outlined, and a statistically reliable predictive regression model is developed. In case of Al1050 – PA6.6, the model describes directly proportional linear relation between the shear load and the pulse frequency, and a nonlinear relation with the beam guidance speed. This shows linear influence of PPP and nonlinear influence of overlap ratio on the joint's resistance to failure. Optimal laser ablation parameters were identified at a spot size of 45 µm, pulse frequency of 120 kHz and beam speed of 1750 mm/s, equivalent to a PPP of ≈ 4.75 kW and a calculated overlap ratio of ≈ 68%.

In case of Ti64 – PA6.6, the process window is limited by deformations of titanium sample at relatively high levels of overlap ratios and PPP. A robust process window is identified between pulse frequency of 40 – 43.89 kHz, and beam speed of 160 – 395.01 mm/s. A statistically significant regression model was developed to describe relation between pulse frequency and beam speed on the joint's resistance to failure. ANOVA analysis revealed significance of beam speed and non-linearity in its response, with no significant impact of pulse frequency along the investigated process window. Strong correlation between overlap ratio and joint resistance to failure is identified. The regression model predicts highest response of shear load at 82% overlap ratio within the investigated process window. Expanding the process window by reducing PPP at 82% overlap ratio reveals a slight increase in the joint's resistance to failure throughout a range of PPP from 65 kW to 15 kW, followed by a sharp drop of joint's shear load at failure at 5kW. Path of steepest ascent reveals a plateau of joint resistance to failure across PPP of 33.93 kHz to 68.09 kHz, identifying optimal ablation conditions at 34.17 kHz and 3772.82 mm/s (PPP = 44.5 kW and O = -145%) resulting in one of the highest average joint resistance to failure and the lowest deviation (1186 ± 11 N).

5.4. Laser-ablated surfaces characterization

In order to evaluate effects of ablation parameters on surface properties, parameters that resulted in significantly different joint resistance to shear load were chosen from the investigated process window, as shown in Table 19. Al represents aluminum samples, and Ti represents titanium ones. Although it is irrelevant to include polished and solvent cleaned titanium surfaces in the hypothesis testing of this thesis – as both surfaces resulted in mixed adhesive/cohesive failure mode, it was decided to investigate some of their properties to identify possible reasons for such relatively weak interfacial bonding. Solvent cleaned aluminum and titanium resulted in a joint shear load of 411 ± 116 N and 772 ± 70 N respectively.

Table 19: attributes of ablated aluminum and titanium samples

Parameter	f_p (kHz)	V (mm/s)	PPP (kW)	Fluence (J/cm2)	Overlap Ratio (%)	Shear load (N)
Al_1	85.00	250.00	11.00	15.20	93	580 ± 41
Al_2	40.00	1000.00	35.00	28.60	44	800 ± 65
Al_3	70.00	1000.00	15.00	17.90	68	1222 ± 143
Al_4	85.00	1750.00	11.00	15.20	54	1341 ± 172
Al_5	120.00	1750.00	5.00	9.12	68	1415 ± 113
Al_5-95%	Same as Al_5 but with 95% power		4.75	8.66	68	1465 ± 65
Ti_1	43.89	160.00	32.00	27.70	92	387 ± 117
Ti_2	40.00	160.00	37.37	30.60	91	690 ± 57
Ti_3	23.89	193.50	65.00	40.00	82	1064 ± 28
Ti_4	34.17	3772.82	41.70	31.00	-145	1186 ± 11
Ti_polished	120.00	2500.00	5.00	9.12	53	764 ± 5

5.4.1. Surface morphology

Al1050

SEM results shown in Figure 55 illustrate the ablated aluminum surfaces indicating effects of the ablation parameters on morphology of aluminum oxide. Images of ablated samples are arranged from left to right in ascending order of increased joint resistance to a shear load as indicated in Table 19. Surfaces ablated with parameters that are associated with the lowest resistance to shear load (Al_1), show relatively high peaks and deep valleys with relatively coarse structures. However, as joint resistance to shear load increases, ablated surfaces are shown to exhibit a smoother topography with finer peak structures, as can be clearly seen with Al_5-95%, which resulted in the highest average resistance to failure. Since failure occurs close to the metal – polymer interface, typically 10-15μm in depth in the polyamide as indicated by topography measurement of polyamide at failure zone, the influence of mechanical interlocking cannot be excluded a priori. It would be expected for a rougher surface to enhance mechanical interlocking and resistance to shear load of laser welded metal – polymer joint. Here, the opposite effect is observed, i.e., the samples exhibiting lower roughness resulted in better resistance to shear load. It is therefore assumed that mechanical interlocking was not the main factor governing the difference in joint resistance to failure across differently ablated surfaces.

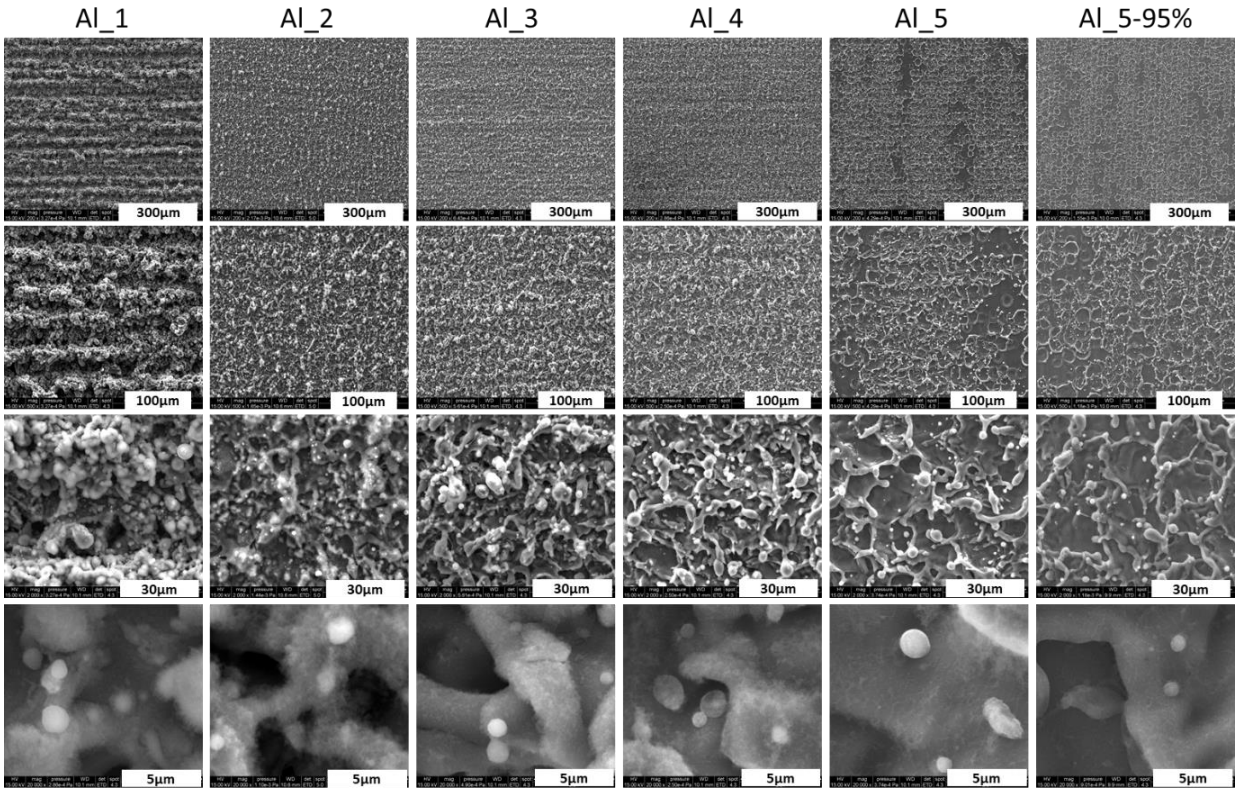

Figure 55: SEM images of ablated aluminum surfaces (laser ablation attributes are indicated in Table 19)

Ti64

Effects of ablation parameters on titanium surfaces are shown in SEM images of Figure 56 along with polished (Ti_polished) and solvent cleaned (Ti_ref) titanium, indicating effects of laser pretreatment parameters on the morphology of titanium oxide. Images of ablated titanium (Ti_1 to Ti_4) surfaces are arranged from left to right in ascending order of increased joint resistance to shear load. Same as in the case of aluminum ablation, a smoother ablated surface with finer and more flat asperities correlates with improved resistance to shear load. Rough surface asperities are visible on all ablated samples which are expected to promote mechanical interlocking. Under high magnification, especially in Ti_3, it can be seen that the surface asperities are composed of finer sub-micron sized features. This might have resulted from interactions between ablation dynamics and rapid oxidation of molten titanium. Laser pulses in Ti_4 parameters result in well-defined craters with almost flat, but rough and sharp, oxidized edges. This morphology correlates with the highest achieved joint resistance to shear load. However, laser pulses during polishing (Ti_polished) occasionally result in smooth-edged craters. No sharp titanium oxide asperities are detected on polished nor reference samples.

The effects of laser ablation parameters, as well as laser-material interaction, on aspect-ratio and morphology of laser-induced craters are well investigated in literature [145]–[148]. During laser ablation, an increase in laser fluence results in an increase in crater diameter [145]. However, it is difficult to outline the crater shape on ablated surfaces in this study due to a large overlap ratio for cases of Ti_1 to Ti_3. Still, the scanning lines can be clearly identified in the “stochastic roughness” observed on those surfaces; more precisely the horizontal lines indicated on Ti_1, Ti_2, and Ti_3 show that the roughness features are aligned. In the case of Ti_4, the negatively calculated overlap ratio (-145)

indicates no pulse overlap in the beam guidance direction (horizontal), resulting in a relatively wide gap between pulses and demonstrating obvious craters. Apparently, laser-material interaction results in a wider crater on titanium than the irradiated spot size (45 μm). Thus, it is important to note that the overlap ratio reported throughout this thesis is based on the theoretical calculation of Equation 6.

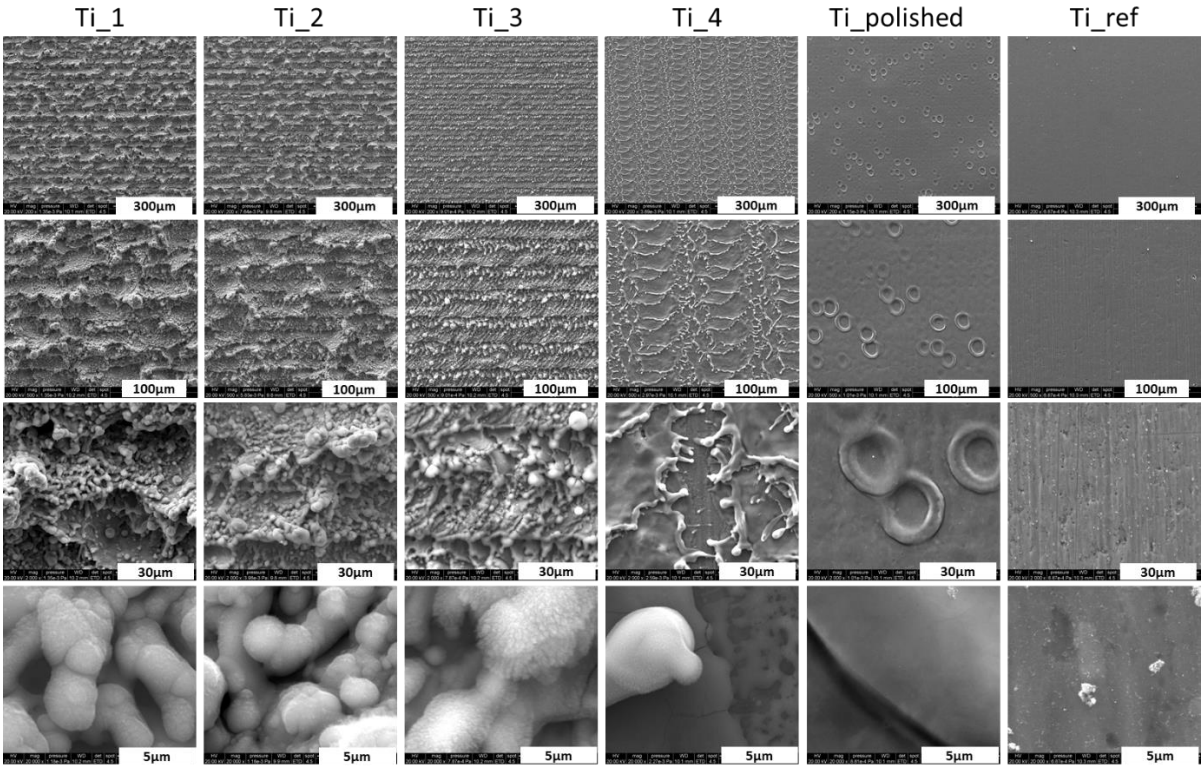

Figure 56: SEM images of ablated titanium surfaces (laser ablation attributes are indicated in Table 19)

5.4.2. Surface wettability

Al1050

All material, in its as received state, can be contaminated from dust, grease and other kind of carbon contaminations. This contamination triggers a decreased wettability (i.e. an increased contact angle). Since ablated samples show perfect wettability, evolution of glycerol droplets on the ablated aluminum surface as a function of time was monitored as described in §4.6.2. Figure 57 shows evolution of glycerol contact angle on five differently ablated aluminum surfaces in the first two seconds. It can be seen that series Al_5, which yielded the high shear load in average compared to the others in the test, demonstrated a starting contact angle of 40°, while sample Al_1, which experienced the weakest joint, demonstrated a lower starting contact angle of 34°. However, all of the samples had a similar rate of spreading across the treated surface. By the end of the process investigation, all the samples were completely wetted, concluding that they are all "glycerol-philic". No significant correlation of the shear load and surface roughness could be noticed with the analysis of the glycerol spreading five differently ablated aluminum samples.

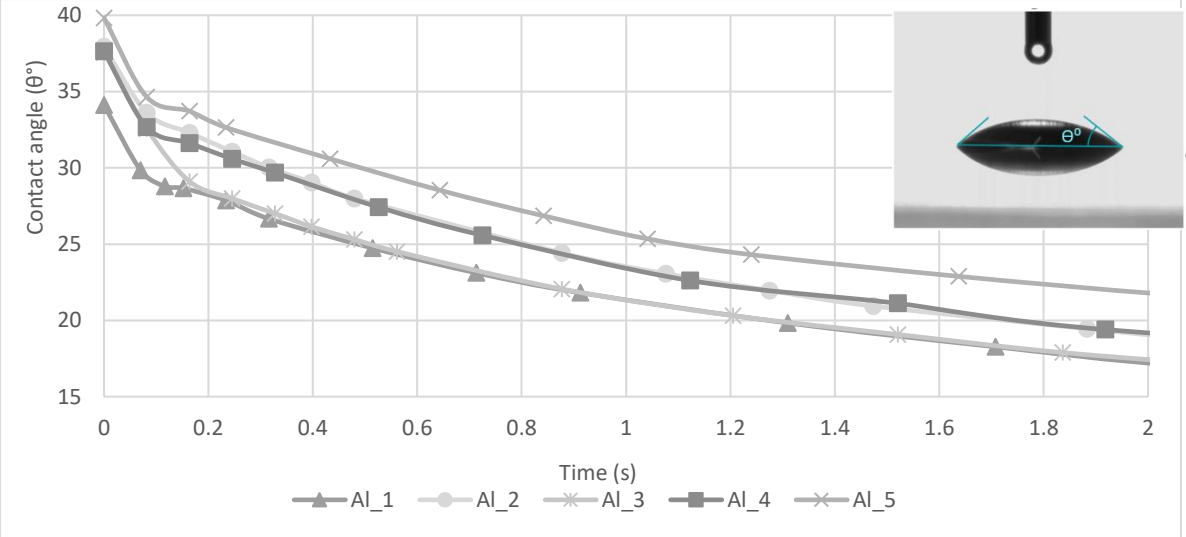

Figure 57: evolution of Glycerol contact angle with time (laser ablation attributes are indicated in Table 19)

Ti64

Four ablation parameters (Ti_1 to Ti_4) resulted in perfect water wettability (water contact angle less than 5°). Otherwise, polished titanium demonstrates a water contact angle of 28.5° ± 2.6° and reference samples results in a water contact angle of 69.8° ± 13.9°. In terms of adhesion phenomena, it is expected that laser ablation increases wetting of polar liquid (e.g. molten polyamide) on modified surfaces, and to a smaller extent, that polished samples show better wettability than that of solvent cleaned surfaces but lower than that of laser-ablated surfaces. This is confirmed by visual inspection where ablated titanium shows cohesive failure mode after failure with perfect wettability of molten PA on ablated titanium surface, and polished samples show mixed adhesive/cohesive failure mode with wider areas of cohesive failure compared to solvent cleaned titanium. Increased titanium surface wettability could result in a larger polyamide residual layer on titanium after failure, since molten polyamide can be considered to be a polar liquid due to presence of amide groups in its molecular structure. However, since all ablated samples show perfect water wettability, it is not possible to extract any difference between these four samples from the sessile drop test.

5.4.3. Surface composition

Al1050

The general surface composition of the treated aluminum surface is shown in Figure 58 as obtained by XPS. It is observed that laser ablation removes large part of absorbed carbon on the surface, together with other impurities, resulting in "cleaning" effect. Samples with surface only wiped with ethanol (Al_ref) shows a high carbon content (29.5 at.%) and a relatively low oxygen concentration (41.1 at.%). Laser ablation pretreatment results in a significant decrease of carbon content along with an increase in oxygen content of the treated surface. Two main effects of the laser ablation process can justify these results. First, high energy density of the laser beam during laser ablation process causes removal of surface contaminants, thereby exposing aluminum surface underneath. Second, high surface temperature during the ablation process results in regeneration of a thicker oxide layer. While a small nitrogen content of 0.7, 0.7, and 0.5 at.% is detected on

Al_1, Al_2, and Al_3 samples, respectively, Al_4, Al_5, and Al_5-95% samples illustrate the presence of only aluminum, oxygen, and carbon elements.

The oxide thickness of the reference samples is estimated at 5.5 nm by using Strohmeier's method [149]. However, this method must be considered with caution when evaluating ablated surfaces because (i) the exact nature of oxide (or hydroxide) is not cross-checked by another technique and (ii) it does completely neglect the roughness in the calculation. No metallic aluminum at 72.7 eV can be found in the high-resolution Al 2p spectra of the ablated samples limiting the use of Strohmeier's method to estimate the oxide thickness. This implies that the oxide layer is much thicker than the depth limit probed in XPS, which is evaluated in its wide range at 20 nm [150]. Details of high-resolution spectra of different elements (C 1s, O 1s, and Al 2p) are similar across the ablated surfaces, as shown in Appendix B, indicating almost identical surface chemistry regardless of laser ablation parameters and resulted joint strength.

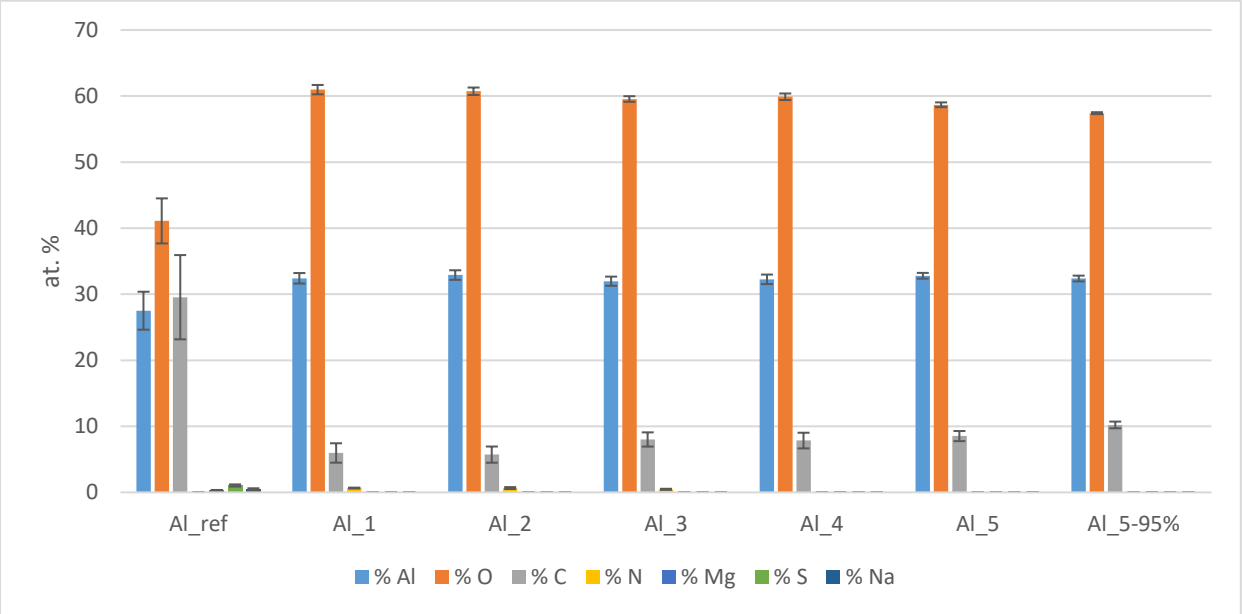

Figure 58: XPS results showing elemental composition of treated aluminum surfaces (laser ablation attributes are indicated in Table 19)

EDX results of ablated aluminum surfaces are shown in Figure 59, illustrating the atomic percentage of oxygen, carbon, and aluminum. While XPS analyzes a depth smaller than 20 nm [150], EDX depth of analysis with the parameters and material in use would yield a depth close to 2 µm. The carbon content is not considered in this study as it cannot be correctly quantified by EDX technique. Interestingly, oxygen concentration increases for all ablated conditions, with a highly significant increase for ablation conditions Al_1 and Al_2 (16.4% and 15.6%, respectively), and a lower increase for conditions Al_3 and Al_4 (9.4% and 6.7%, respectively), compared to untreated aluminum (2.4%). This is coherent with XPS results and leads to the assumption that aluminum oxidation occurs for ablation conditions at a depth of greater than 20nm. EDX results show a significant correlation between an increased joint resistance to failure and a decreased oxygen atomic percentage, from ablated parameter Al_1 to that of Al_5-95%, with Pearson correlation coefficient ($r = -0.98$). A decline in oxygen peak intensity along ablated samples Al_1 to Al_5 suggests a decline in aluminum oxide and/or hydroxide layer thickness. Aluminum oxide (12 mm^2/s) has lower thermal diffusivity than pure aluminum (94 mm^2/s) at 300 K

[151]. If we assume oxygen is entirely bound to aluminum in the form of aluminum oxide, a decline in aluminum oxide thickness would have an impact on improving thermal transfer between the joining partners resulting in an increase in the volume of molten polymer and improving the joint quality achieving a higher resistance to failure. However, EDX results should be considered with caution when referring to aluminum oxide and/or hydroxide layer thickness as they might be influenced by topographic changes. EDX is not conclusive for conditions Al_5 and Al_5-95%, probably because it is not precise enough to detect differences at these low concentrations of oxygen (close to 2.4%).

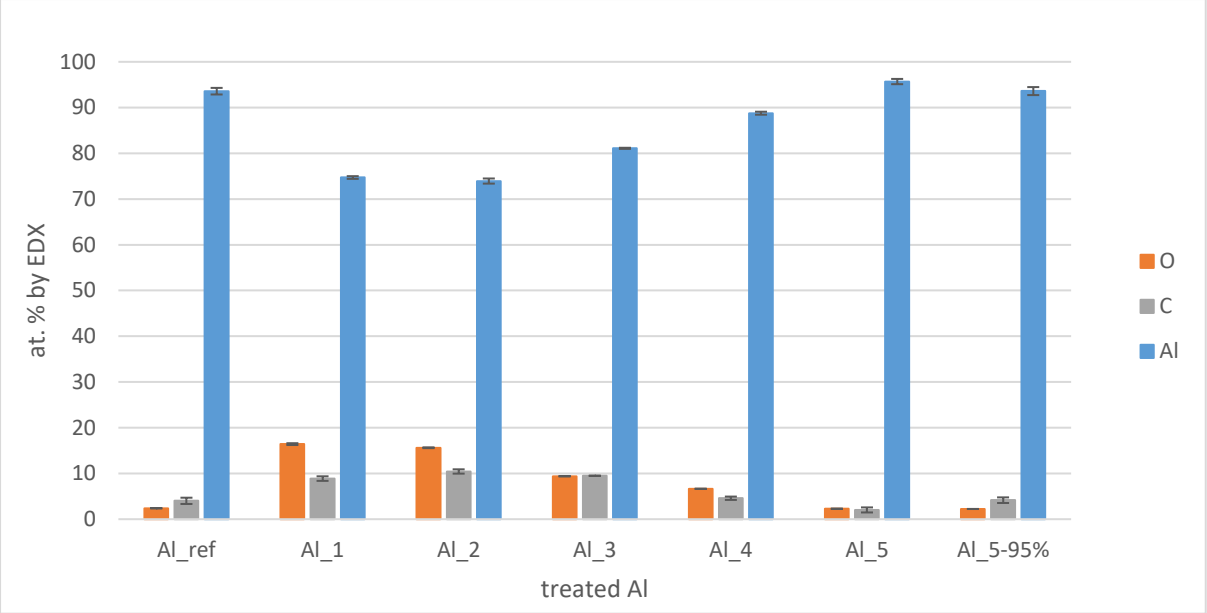

Figure 59: EDX results of treated aluminum surfaces (laser ablation attributes are indicated in Table 19)

Ti64

Figure 60 shows the composition of laser-ablated, laser polished, and solvent cleaned titanium surfaces as obtained by XPS. Survey spectra and selected high resolution spectra are shown in Appendix C. Results show fewer surface impurities (Si, S, F, Fe, Ca, Zn) on ablated surfaces compared to solvent cleaned and laser polished surfaces. Increased oxygen content indicates oxidation of laser-ablated titanium surface. It is noticeable that ablation also reveals more from the bulk of the material, which explains the increase in Al and V percentages in the four ablated surfaces. Results show no significant difference in surface composition of three of the four ablated surfaces: Ti_1, to Ti_3. However, a slight increase of carbon (C) content, and a decrease of oxygen (O) and titanium (Ti) content, are shown on Ti_4 sample's surface. This might be linked to the negative overlap ratio and relatively lower PPP of the laser ablation parameters resulting in a lower "cleaning effect" of the titanium surface compared to other ablation conditions Ti_1 to Ti_3.

Results indicate oxidation and cleaning effects for laser-ablated titanium surfaces leading to a titanium oxide layer with a reduction in miscellaneous contamination elements other than carbon. However, the effects of surface roughness complexity associated with ablated surfaces, as observed from topography data (§5.4.4) and qualitatively observed in SEM pictures (Figure 56), on the very low level of water contact angle cannot be excluded a priori. Interestingly here, the less rough character and less favorable surface composition

of Ti_4 does not change its water wettability compared to other ablated surfaces. In other words, the water contact angle test is not able to discriminate between all the ablated surfaces.

As for the polished sample, no significant difference in roughness amplitude (§5.4.4) and level of carbon contamination from the reference sample can be identified. Therefore, it is assumed that the better water wettability (§5.4.2) of polished sample is a consequence of a cleaning effect, which is manifested here by the slight increase in titanium concentration, and a decrease of miscellaneous contamination elements other than carbon (Si, S, F, Fe, Ca, Zn). Oxygen levels on the polished surface are low, even compared to solvent cleaned surface. This phenomena is also reported in laser polishing of commercially pure titanium using with a ns ArF excimer laser [152], and might be assigned to melting of the native titanium oxide and re-formation of a new, but thin, oxide layer after laser polishing. Relatively similar carbon concentration on solvent cleaned and laser polished surfaces can explain their relatively low interfacial bonding when laser welded to PA6.6, resulting in mixed failure mode.

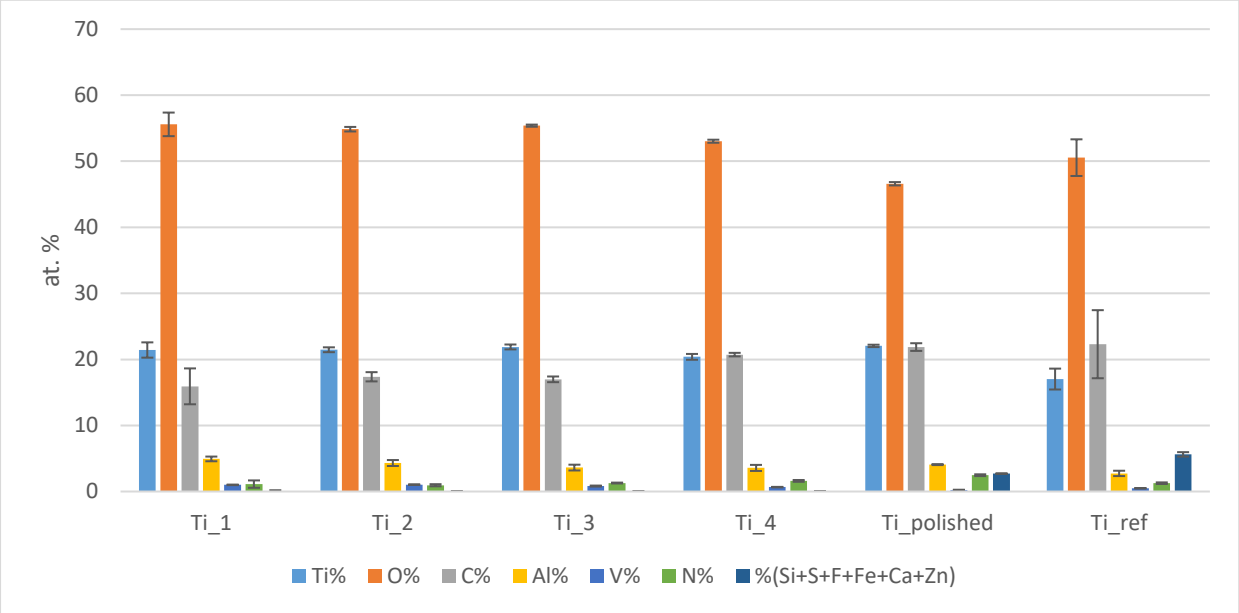

Figure 60: XPS results showing elemental composition of treated titanium surfaces (laser ablation attributes are indicated in Table 19)

EDX results of treated titanium surfaces are shown in Figure 61, demonstrating the atomic percentage of oxygen, titanium, carbon, aluminum and vanadium. Based on testing conditions, EDX yields a depth of analysis reaching a maximum of 1-2µm. An increase in oxygen elemental content is observed on all laser-treated surfaces, compared with solvent cleaned surface, emphasizing surface oxidation. A lower oxygen signal for sample Ti_4, with respect to other titanium ablation conditions, can be justified by lower oxidation during the ablation process, which correlates with laser energy per scanned length (pulsed peak power/speed) of Ti_4 compared to Ti_1, Ti_2, and Ti_3. Unlike the case of aluminum ablation, no correlation can be found between the elemental composition of ablated titanium surfaces and the joint resistance to failure. EDX results of the polished sample show comparable composition to the reference sample, with lower oxidation compared to laser-ablated samples, which can be justified by the relatively low PPP

associated with the laser polishing process. In terms of oxidation, EDX results are coinciding with XPS results.

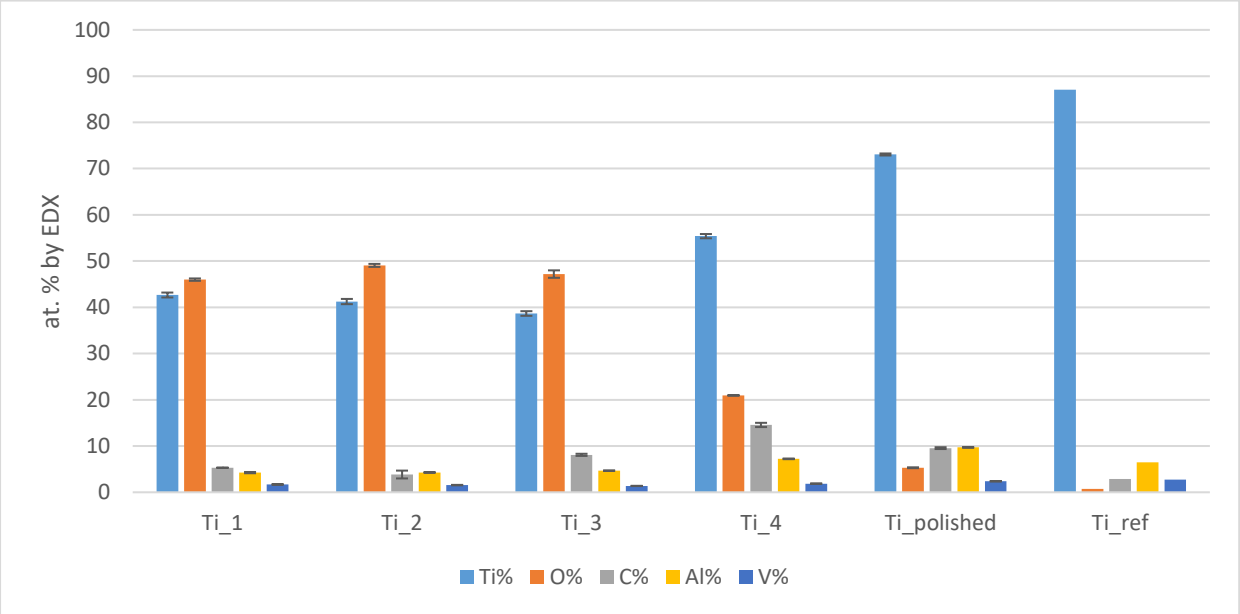

Figure 61: EDX results of treated titanium surfaces (laser ablation attributes are indicated in Table 19)

5.4.4. Surface topography

Al1050

Table 20 shows results of 3D topography mapping of ablated aluminum surfaces from Al_1 to Al_5. Sa represents arithmetical mean height within the defined area, and Sz is defined as the sum of the largest peak height value and the largest pit depth value. A correlation between Sa and joint resistance to failure is noticed favoring a smoother surface for improved performance. Ssk defines skewness of surface, and a positive value means that the surface contains mainly peaks and asperities rather than valleys. However, "masking" effect can be expected by the random morphological features of ablated aluminum oxide, as indicated by SEM, covering valleys during the topography test. Sku (Kurtosis) measures the sharpness in the defined area. Sku > 3 indicates sharp surface features. Sdr is the developed interfacial area ratio and it expresses the percentage of additional surface area, which results from the surface texture, as compared to the planed definition area.

Table 20: 3D profilometry parameters of ablated aluminum (laser ablation attributes are indicated in Table 19)

	Al_ref	Al_1	Al_2	Al_3	Al_4	Al_5
Sa (µm)	0,48 ± 0.06	5,43 ± 0.07	1,65 ± 0.06	1,43 ± 0.05	1,34 ± 0.04	1,07 ± 0.01
Sz (µm)	5,92 ± 1.03	37,25 ± 1.91	16,30 ±4.95	10,90 ± 0.99	12,15 ± 2.33	9,97 ± 1.74
Ssk (µm)	1,90 ± 1.55	0,50 ± 0.26	1,30 ± 0.53	0,70 ± 0.02	0,80 ± 0.14	0,90 ± 0.14
Sku (µm)	12,40 ± 11.72	3,10 ± 0.25	6,70 ± 3.79	3,70 ± 0.47	4,20 ± 0.11	4,90 ± 1.53
Sdr (%)	1,02 ± 0.00	55,70 ±11.22	26,70 ± 1.64	17,56 ± 1.99	20,22 ±1.21	19,05 ± 7.28

3D mapping of ablated surfaces is shown in Figure 62. It adopts a unified Z scale of 36 µm for all measured samples. The zero is referenced at the median Z value so that a particularly deep valley or high peak does not accidentally influence the scale position. Qualitative assessment of topography results shows that an improved joint resistance t failure correlates with a decrease in density of high peaks and valleys distribution. This

suggests that the shear load correlates with two main topographic features: the distribution density of peaks and valleys, and their average amplitude.

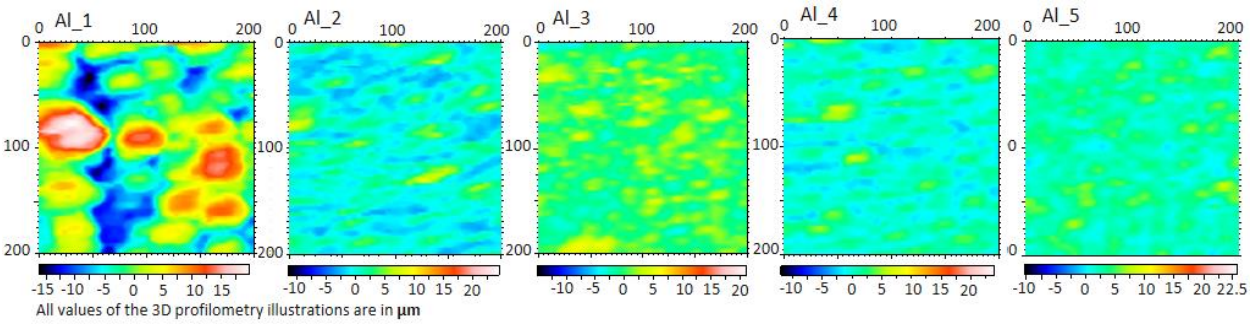

Figure 62: 3D profilometry mapping (laser ablation attributes are indicated in Table 19)

2D profilometry results are shown in Figure 63 indicating the root-mean-square roughness (Rq) and root-mean-square slope (Rdq) of each ablated aluminum sample, and demonstrates the relation between roughness profile elements' mean width (Rsm) with joint resistance to failure. The reference aluminum (cleaned with ethanol) exhibits relatively low surface roughness (Rq = 0.43 ± 0.26 µm). Slight inverse correlation was found between the joint resistance to failure and Rq and Rdq of laser-ablated samples, indicated by Pearson's correlation coefficient of -0.83 and -77, respectively, and a strong inverse correlation between Rsm and joint resistance to failure (r = - 0.90). A decrease in Rsm would result in improved thermal transfer across the interface during the laser welding process as more aluminum oxide 'peaks' will be in contact with polyamide, which might explain the improved joint resistance to shear load.

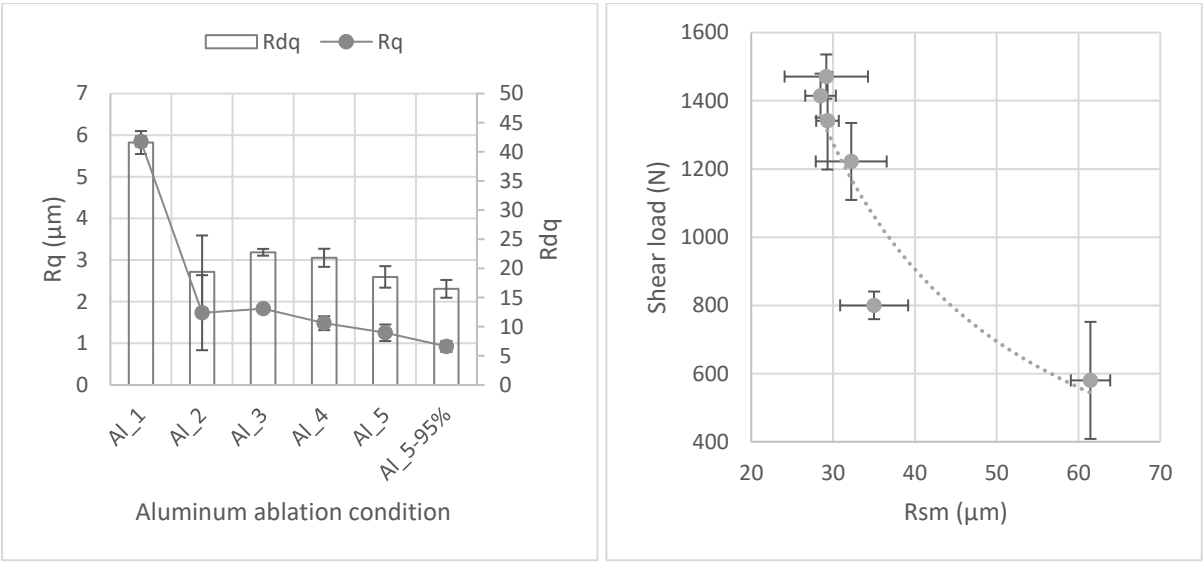

Figure 63: 2D topography results of treated aluminum surfaces (laser ablation attributes are indicated in Table 19)

Ti64

2D profilometry results of treated titanium surfaces are shown in Figure 64. Reference titanium exhibits relatively low roughness amplitude (Rq = 0.07 µm) and the polished sample shows slightly higher roughness (Rq = 0.18 µm) compared to ablated samples. The same applies for Rdq values. These results show quantitatively what was assumed from the observation of SEM pictures, i.e. reference and polished samples are very smooth

compared to the ablated samples, and that roughness amplitude decreases from Ti_1 to Ti_4. Regarding laser-ablated titanium, although no significant correlation can be found between Rsm and joint resistance to failure (r = -0.63), a strong inverse correlation is found between both Rq, Rdq and the joint's resistance to failure indicated by Pearson correlation coefficients of −0.99 and −0.98, respectively.

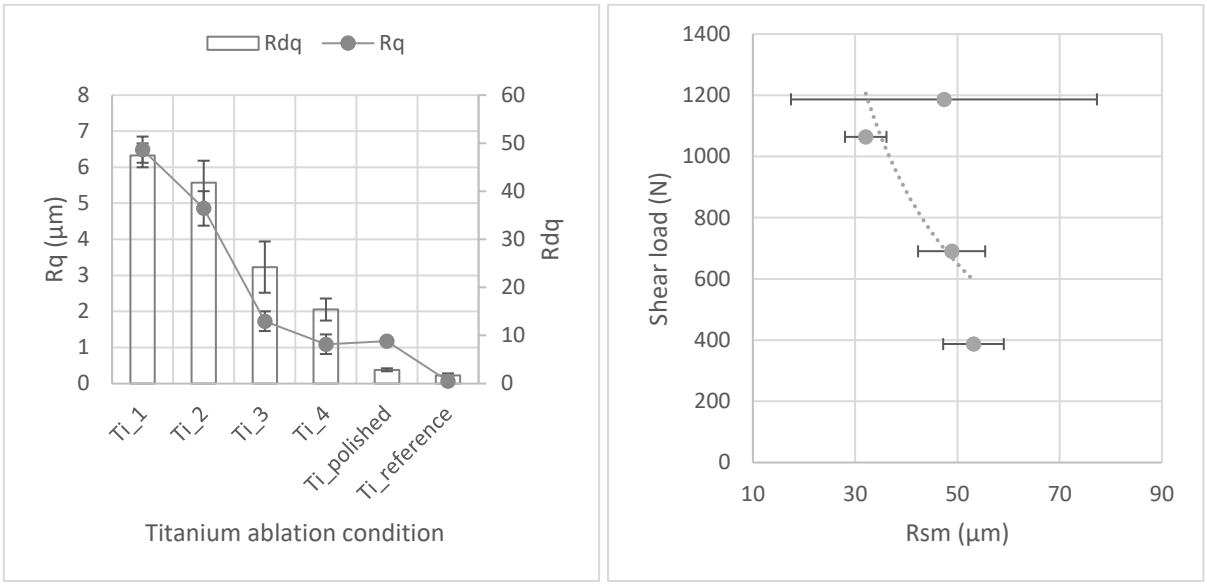

Figure 64: 2D topography results of treated titanium surfaces (laser ablation attributes are indicated in Table 19)

However, it is still difficult to reach a conclusion by correlating the values of the roughness parameters individually with joint resistance to shear load. TCR is calculated as a function of a ratio between root-mean-square roughness (Rq) and root-mean-square slope (Rdq) parameters as indicated in the CMY model (§2.5). A correlation between the ratio of those two parameters and the joint resistance to shear load supports proving the hypothesis (§3) by highlighting the influence of TCR on LAMP joint performance.

5.5. Interfacial thermal transfer

5.5.1. Cooper–Mikic–Yovanovich (CMY) model

Cooper–Mikic–Yovanovich (CMY) model (§2.5) describes a relation between the ratio of topography parameters (Rq/Rdq) and interfacial TCR. In order to test the hypothesis (§3), the relation between this parametric ratio and joint performance is reported in Figure 65. Interestingly, results show a strong inverse correlation (r = -0.94%) between Rq/Rdq and joint resistance to failure in all ablated samples (Al1050 and Ti64) combined. This indicates a strong impact of surface roughness on joint performance by influencing TCR during the laser welding process. Analyzing correlation between topography coefficient (Rq/Rdq) and joint resistance to failure in case of aluminum and titanium ablation, separately, also shows a strong correlation with Pearson's correlation coefficients of -0.93 and -0.99, respectively. However, having a common trend between two ablated metallic materials with very different thermophysical properties, shows that surface roughness is the governing factor of the ablated samples' joint performance, and ensures the generalization and reproducibility of this finding.

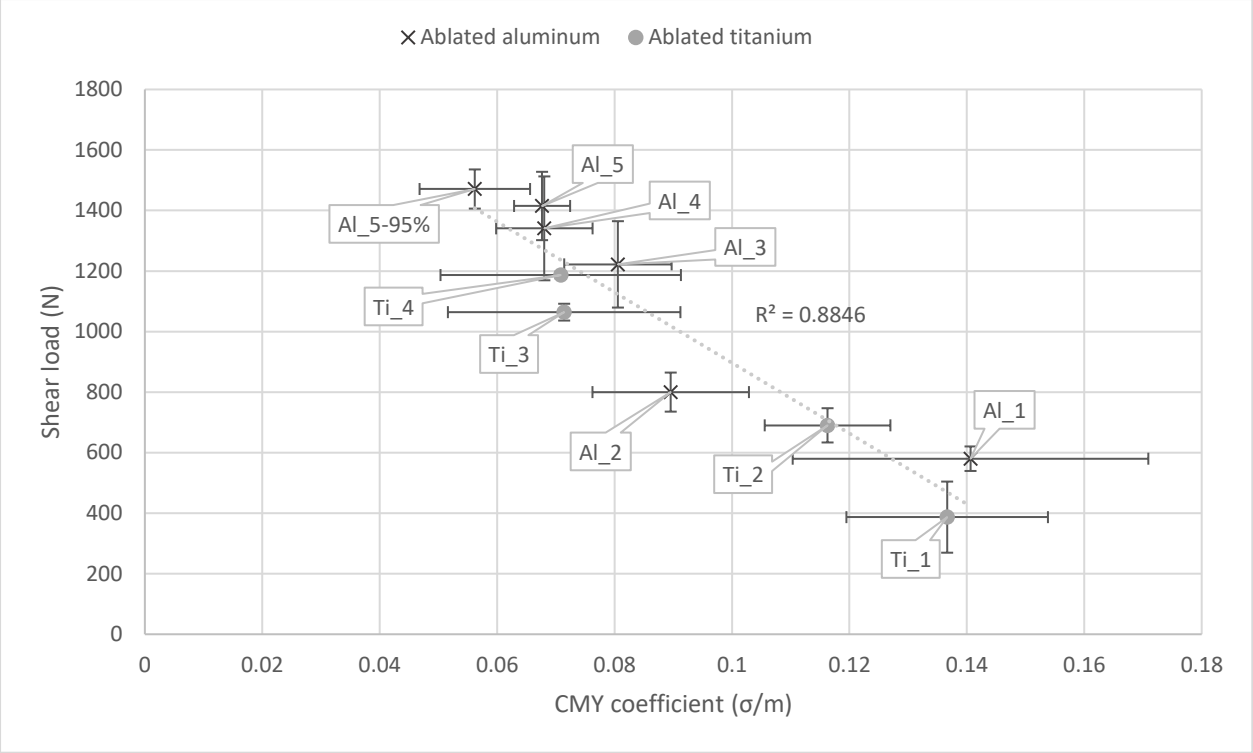

Figure 65: relation between CMY coefficient (σ/m), calculated with topography ratio (Rq/Rdq), and joint resistance to failure (laser ablation attributes are indicated in Table 19)

5.5.2. Laser Flash Analysis (LFA)

Layered LFA results, shown in Figure 66, illustrate the relation between measured TCR of ablated surfaces and the joint resistance to shear load. Results show a lower TCR for all ablated titanium samples than that of all ablated aluminum samples. However, given that thermal diffusivity of aluminum oxide is around 13% that of pure aluminum, and given that laser ablation of aluminum results in a strong influence on oxide layer thickness as demonstrated in EDX results (§5.4.2), it is expected that a thick aluminum oxide layer would increase calculated TCR values. Moreover, it is important to note that LFA does not provide quantitative data on TCR between the joining partners during the welding process, given the testing setup in use as explained in §4.2. It rather provides a valid comparison between differences in TCR of ablated surfaces from the same material.

Results demonstrate that a decreased TCR across the interface of the layered setup correlates significantly with an increase in the laser-welded joint resistance to failure, with a Pearson correlation coefficient of r = -0.94 and r = -0.99 for ablated aluminum and titanium respectively. Results confirm that the improvement in joint quality is very likely to be a result of enhanced thermal conductivity across the interface of the joining partners during the welding process. If so, increased TCR should correlate with a decline in molten polymer and joint area.

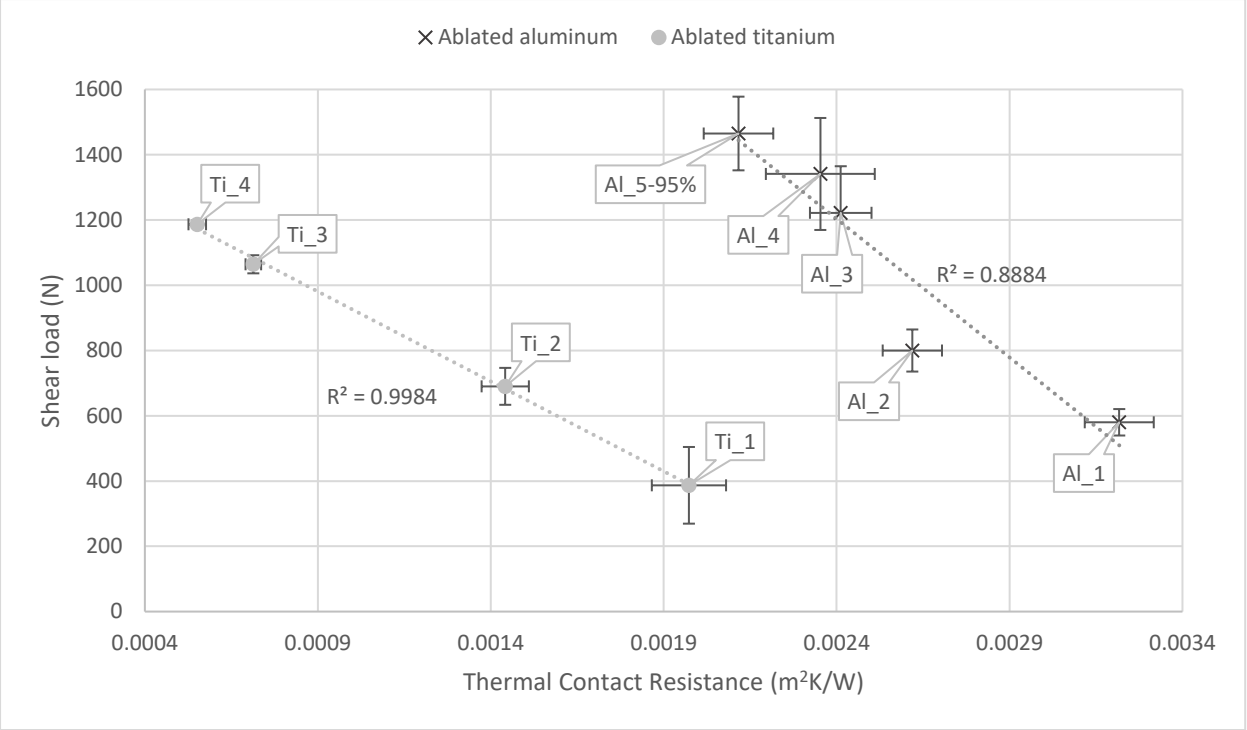

Figure 66: relation between TCR and joint resistance to failure of selected laser-ablated samples (laser ablation attributes are indicated in Table 19)

5.6. Joint strength and quality

5.6.1. Joint strength

In order to quantify the joint strength, joint area at the interface was identified after failure as the area of damages/residues on both joining partners. The joint area measured on the metallic surface in case of ethanol wiped aluminum (Al_ref) and titanium (Ti_ref), and laser polished titanium (Ti_polished) shows 58%, 65%, and 73% of the corresponding joint area on polyamide, respectively, indicating a mixture between adhesive and cohesive failure modes. Thus, those conditions are irrelevant for the hypothesis testing in this study. Figure 67 shows joint area versus shear load at failure for ablated metallic surfaces of welded samples in both Al1050 – PA6.6 and Ti64 – PA6.6 combinations. Although shear load at failure of both combinations varies from 387 N to 1632 N, a linear relation between joint area and shear load indicates constant strength across all welded samples of both material combinations. Linear regression model describing the relation between all data points illustrates a high coefficient of determination (R^2) of 0.95, demonstrating very low variability in the calculated strength. The joint strength is indicated by a slope of 36.4 MPa. Moreover, results show relatively equal and matching joint area on corresponding metal and polyamide partners for both material combinations, highlighting cohesive failure mode and indicating that the reported variation in joint quality is less likely to be a result of interfacial adhesion, i.e. chemical bonding or mechanical interlocking. The effects of aluminum laser ablation parameters on the joint area are illustrated by the stitched microscopic images of PA joint area shown in Figure 67. An inverse correlation between joint resistance to failure and join area confirms a strong influence of TCR on area of molten polymer and corresponding joint quality.

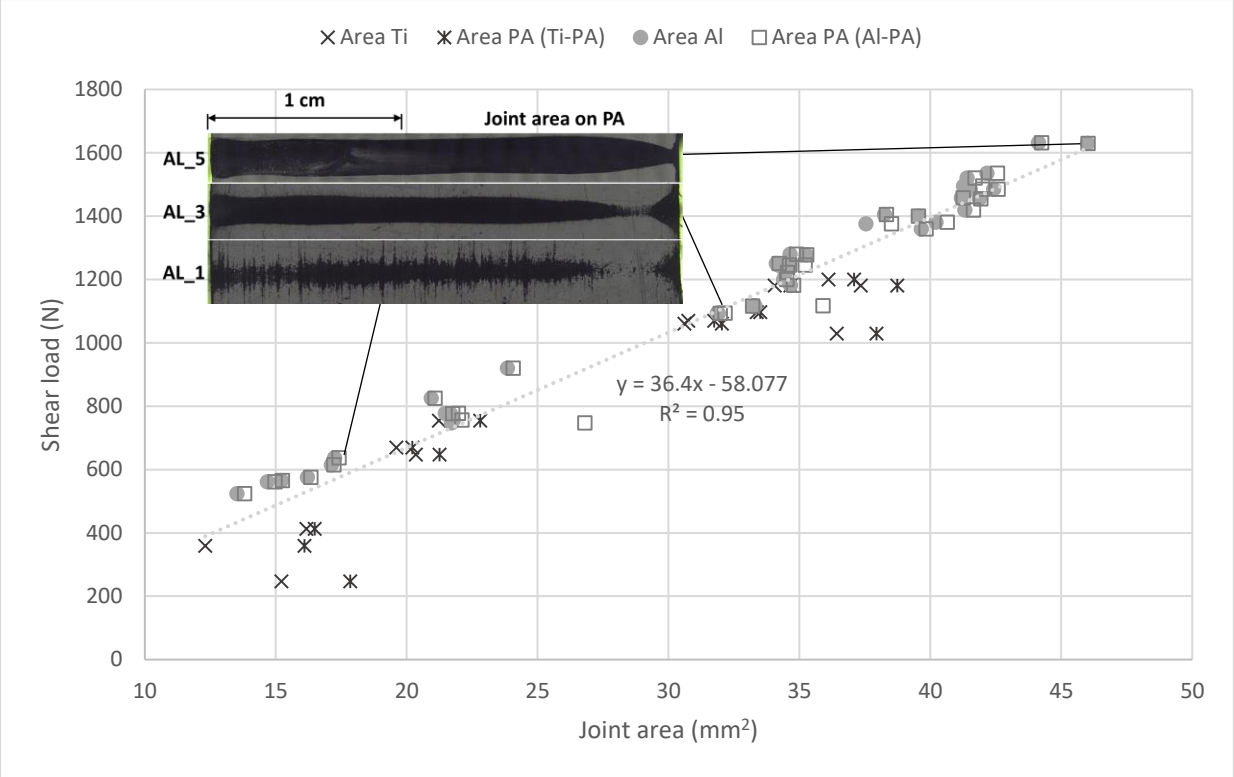

Figure 67: relation between joint area and shear load; stitched microscopic images show PA joint area after failure (dark area)

5.6.2. Joint quality

Figure 68 shows SEM images of laser-welded titanium – polyamide cross-sections, having titanium surface ablated with Ti_1 and Ti_4. The difference in titanium topography of both samples is very clear. While smoothly ablated sample (Ti_4) shows intimate joining between the interface of both partners, even at titanium's surface asperities, roughly ablated titanium (Ti_1) shows voids at deep valleys of its topography indicating no joining at those regions. The random morphology of surface asperities is expected to release any potential gaseous products generated from the welding process at the interface. The absence of bubbles/voids at the interface of Ti_4 indicates no welding induced defects. Given that both surfaces are welded with similar parameters (see §4.2.2), it is highly unlikely that the voids in the deep valleys of Ti_1 are a result of bubble formation and/or polymer degradation.

However, the flow of polyamide inside titanium surface asperities in both ablated surfaces indicates mechanical interlocking between joining partners. Interestingly, Ti_1 (rough surface) resulted in lower joint resistance to failure compared to Ti_4 (smooth surface), suggesting that mechanical interlocking is not the governing aspect of joint performance. Moreover, since cohesive failure mode is observed after shear load testing, specifying no interfacial failure, and given that all the samples failed at similar joint strength (MPa), it is unlikely that those voids had an effect on the joint's resistance to shear load during testing. However, those voids can result from inadequate melting of polyamide due to limited thermal transfer at regions of deep valleys during the laser welding process. On the other hand, intimate joining in the case of smoothly ablated titanium suggests adequate thermal transfer and proper melting of polyamide at the interface.

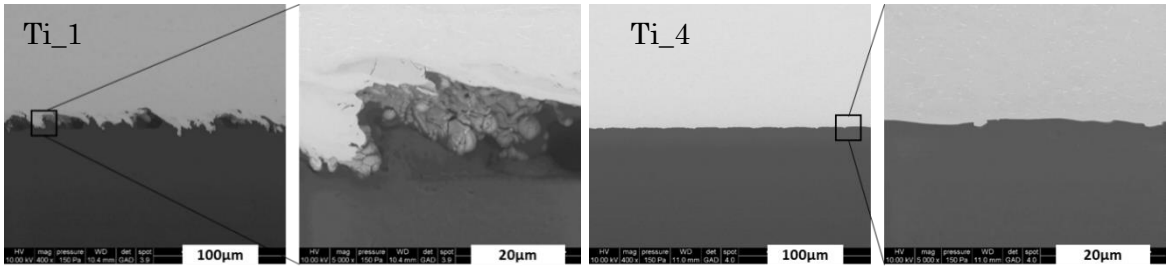

Figure 68: SEM of Ti64 – PA6.6 cross sections under different titanium laser ablation conditions (laser ablation attributes are indicated in Table 19)

Chapter 6

6. Summary and conclusion

This work aims at expanding the understanding of the effects of surface pretreatments on properties and performance of LAMP joints by outlining the effects of surface properties on interfacial thermal transfer. Considering industrial relevance, two metallic materials with different thermophysical properties were used in the study to be welded with polyamide 6.6, those are aluminum (Al1050) and titanium (Ti64). First, the laser welding process was optimized and parameters were kept unchanged. Optimal laser welding parameters of Al1050 – PA6.6 were obtained from literature, and optimization of Ti64 – PA6.6 laser welding process was performed using DoE techniques. Laser welding optimization experiments mapped effects of focal position, laser power, and beam speed on joint strength and quality. This work identified and eliminated laser welding defects, in particular weld pool cavities, flash defect, excessive penetration, bubbles and voids. Results showed optimal joining conditions at 2.7 J/mm^2 under the shielding of argon gas at a flow-rate of 10 L/min, following 8 mm wide spiral wobble trajectory with 0.2 mm gap between consecutive wobbles.

It is hypothesized that a smoother pretreated surface in LAMP would promote the interfacial thermal transfer during the laser welding process, resulting in a larger joint area and an improved joint performance. To properly test this hypothesis, the effect of interfacial adhesion on joint performance has to be avoided, and a cohesive failure has to be guaranteed.

Two factors are reported in literature with the most influence on interfacial adhesion in LAMP, those are chemical bonding and mechanical interlocking. Preliminary investigations were conducted to study the influence of plasma pretreatment and laser ablation on laser-welded Al1050 – PA6.6 joints. While plasma pretreatment results in insignificant changes in surface topography, which is responsible for mechanical interlocking, laser ablation parameters result in relatively similar surface composition and chemistry, which are responsible for chemical bonding. Results show an increase in joint resistance to failure in the case of plasma pretreatment of each of the joining partners, and a higher increase in the case of plasma pretreatment of both joining partners. Such increase in joint performance is not related to any changes in topography of the treated surfaces, but rather correlated with changes in surface chemistry and an increase in surface energy, resulting in a larger distribution density of cohesive failure regions. These findings confirm that an improvement in assembly's shear resistance to failure can certainly be achieved without an increase of the interfacial interlocking, as observed in the case of plasma-treated aluminum.

Compared to plasma pretreatment, laser ablation results in the highest improvement of joint performance and in a fully cohesive failure mode. This is assigned to modifications in surface chemistry and to strengthening effects related to the high increase of roughness amplitude of ablated surfaces. Laser ablation results in a cleaner (fewer surface contaminations) more oxidized chemistry, and also in a rough morphology compared to plasma pretreatment of aluminum, and laser polishing of titanium. Both of those properties certainly contribute to better interfacial adhesion, justifying absence of

adhesive failure in laser-ablated samples. In this regard, water contact angle measurements show an interesting comparison between surface properties before welding: samples with lower angle, i.e. better wettability, show more distribution of regions with cohesive failure. Laser ablation resulted in perfect wettability to water and diiodomethane, and in a fully cohesive failure mode. However, contact angle measurements were not able to identify differences between ablated samples. Using DoE, further studies were performed to outline the effects of aluminum and titanium laser ablation parameters on the joint performance when laser welded to polyamide. Results reveal a prominent effect of PPP and overlap ratio on joint resistance to shear load, highlighting optimal ablation parameters at a pulse frequency of 120 kHz and 34.17 kHz, and speed of 1750 mm/s and 3772.82 mm/s, for aluminum and titanium, respectively, at a spot size of 45 µm. PPP of 4.75 kW and 44.5 kW, and overlap ratio of 68% and -145%, are calculated at the optimal ablation conditions of aluminum and titanium, respectively.

Effects of aluminum and titanium laser ablation parameters on surface properties, interfacial thermal transfer, and joint quality when laser welded to polyamide were investigated. In terms of surface properties, the main difference that could be accounted for laser ablation parameters is the surface topography of ablated metal, manifested quantitatively by roughness amplitude (Rq) and roughness slope (Rdq) values. Increased surface roughness promotes mechanical interlocking, which certainly plays an important role in strengthening interfacial adhesion. In this research, the joint resistance to failure increases when the roughness characteristic values of ablated surfaces decrease. The contrary would be expected if mechanical interlocking would be prominent. As evidenced here, mechanical interlocking effects were not governing joint performance as all ablated samples showed cohesive failure mode with equal and matching joint area on both joining partners. Ratio between two topography variables (Rq/Rdq), which represents σ/m ratio in the CMY model, shows a strong influence on interfacial TCR as discussed in §2.5. An increase in root-mean-square roughness (Rq), alongside a decrease in Root mean square slope (Rdq), reduces the area of contact between surface asperities at the interface, limiting thermal transfer. Strong inverse correlation ($r = -0.94$) between Rq/Rdq and joint resistance to failure in both material combinations, indicates that an increased TCR across interface deteriorates joint performance. LFA experiments following Hartmann's method were conducted to evaluate TCR of differently ablated surfaces. Results show a strong inverse correlation between TCR with shear load at failure of laser-welded Al1050 – PA6.6 ($r = -0.94$) and Ti64 – PA6.6 ($r = -0.99$).

Improved interfacial thermal transfer should increase the area of molten polymer and joint resistance to shear load. From post-mortem joint area inspection, it is observed that all laser ablation parameters for both aluminum and titanium yielded in a cohesive failure mode with the matching area on both joining partners. Moreover, all ablated samples of both material combinations exhibit a relatively similar shear strength of 36.4 MPa, indicating similar failure behavior. In fact, the reported differences in joint performance are a result of changes in the joint area, which correlates very well with changes in topography parameters of metallic joining partner, which governs TCR, and with the measured TCR itself. Thus, it can be concluded that changes of TCR by means of different topography explain the increase in shear load related to differently ablated surfaces.

The fact that both studies, one with aluminum and the other with titanium, led to similar results and similar conclusion, strengthen the research findings and confirms their generalization and reproducibility.

Based on this work, need for the following investigations arises in order to expand the understanding on the effects of surface properties and interfacial thermal transfer in LAMP:

- Results have shown nonlinear effect of polyamide plasma pretreatment exposure time on joint resistance to failure. More investigations are required to explore the influence of plasma pretreatment time on polyamide's surface properties, e.g. crystallinity, morphology, etc. and to understand its effects on joint performance.
- In order to expand the understanding of the effects of surface properties on interfacial thermal transfer, modeling, simulation and experimental investigations are required in four dimensions, considering special and temporal propagation of thermal energy through the polymer's joint zone.
- The interaction between laser ablation pretreatment and laser welding parameters, and their influence on interfacial thermal transfer, should be investigated to explore the potentials of adapting the laser welding parameters to the surface properties in order to further improve the joint performance.
- Although constant joint strength is reported among all laser-ablated samples of both material combinations, suggesting similar failure behavior, effects of the interfacial thermal transfer on the polymer's morphology and crystallinity across the joint zone should be investigated for opportunities to optimize the properties at the region of failure.
- The interaction between surface properties and failure mechanism should be further investigated in order to determine the crack initiation location in addition to the speed and direction of crack propagation. In addition, further investigations should be carried out on the joint performance at different environments and modes of loading, i.e. elevated temperature, peeling stress, and dynamic loading, in order to expand the understanding of the influence of interfacial thermal transfer on the welded joint.

References

[1] Center for Automotive Research, "Automotive Technology : Greener Products , Changing Skills Lightweight Materials & Forming Report," Driv. Cha. Rep., 2011.

[2] N. Lutsey, "Survey of vehicle mass-reduction technology trends and prospects," El Monte, California, 2010. https://www.yumpu.com/en/document/view/8263209/survey-of-vehicle-mass-reduction-technology-trends-and-prospects (accessed Feb. 05, 2021).

[3] Lanxess Corporation, "Plastic/Metal Hybrid Technology: Innovative Design Solutions for Structural Performance with Weight and Cost Reduction," 2005, [Online]. Available: http://techcenter.lanxess.com/scp/americas/en/docguard/P_M_Hybrid_Solutions.pdf?docId=77014 (accessed Feb. 08, 2021).

[4] Mark Kane, "ONSERT: That's How BMW i3, BMW i8 Join Lightweight Materials," 2014. https://insideevs.com/onsert-thats-bmw-i3-bmw-i8-join-lightweight-materials-wvideo/ (accessed Feb. 10, 2021).

[5] C. Soutis, "Carbon fiber reinforced plastics in aircraft construction," *Mater. Sci. Eng. A*, vol. 412, pp. 171–176, 2005, doi: 10.1016/j.msea.2005.08.064.

[6] I. Inagaki, T. Takechi, S. Yoshihisa, and A. Nozomu, "Application and Features of Titanium for the Aerospace Industry," 2014.

[7] R. R. Boyer, "Titanium for aerospace: Rationale and applications," *Adv. Perform. Mater.*, vol. 2, no. 4, pp. 349–368, 1995, doi: 10.1007/BF00705316.

[8] A. K. Naskar, J. K. Keum, and R. G. Boeman, "Polymer matrix nanocomposites for automotive structural components," *Nat. Nanotechnol.*, vol. 11, no. 12, pp. 1026–1030, 2016, doi: 10.1038/nnano.2016.262.

[9] "Worries about new composite made airplane," 2011. https://www.1001crash.com/transport-page-composite-lg-2.html (accessed Feb. 10, 2021).

[10] H. C. Amstutz, "Polymers as bearing materials for total hip replacement: A friction and wear analysis," *J. Biomed. Mater. Res.*, vol. 3, no. 4, pp. 547–568, 1969, doi: 10.1002/jbm.820030402.

[11] G. Renganathan, N. Tanneru, and S. L. Madurai, "Orthopedical and biomedical applications of titanium and zirconium metals," in *Fundamental Biomaterials: Metals*, P. Balakrishnan, S. M. S, and S. Thomas, Eds. Woodhead Publishing, 2018, pp. 211–241.

[12] C. N. Elias, J. H. C. Lima, R. Valiev, and M. a Meyers, "Biomedical Applications of Titanium and its Alloys," *J. Miner. Met. Mater. Soc.*, vol 60, pp. 46–49, 2008, doi: 10.1007/s11837-008-0031-1.

[13] M. Vojdani and R. Giti, "Polyamide as a Denture Base Material: A Literature Review.," *J. Dent. (Shiraz, Iran)*, vol. 16, no. 1 Suppl, pp. 1–9, 2015.

[14] J. R. Davis, "Handbook of Materials for Medical Devices," ASM International, 2003. doi: 10.1361/hmmd2003p001.

[15] "Shenzhen Changhua Biomedical Engineering Co.,ltd."

https://www.ecplaza.net/offers/orthopedic-implant-of-polyamide-composite-material_8482655 (accessed Feb. 16, 2021).

[16] B. Qiao *et al.*, "Bone plate composed of a ternary nano-hydroxyapatite/polyamide 66/glass fiber composite: Biomechanical properties and biocompatibility," *Int. J. Nanomedicine*, vol. 9, no. 1, pp. 1423–1432, 2014, doi: 10.2147/IJN.S57353.

[17] "Dental Implant Abutments & Attachments." https://preat.com/attachment_systems/dental-implant-abutments/ (accessed Feb. 16, 2021).

[18] "Cementless Implant - Stryker Components." https://tarlowknee.com/surgical-treatments/cementless-press-fit-total-knee-replacement/ (accessed Feb. 13, 2021).

[19] R. W. Messler, "Features Trends in key joining technologies for the twenty-first century," Assem. Auto, vol 20, no. 2, pp. 118 - 128, 2014.

[20] M. C.-Y. Niu and M. Niu, *Composite Airframe Structures*, Third edit. Hong Kong Conmilit Press Ltd, 2010.

[21] R. W. Messler, "Joining Composite Materials and Structures: Some Thought-provoking Possibilities," *J. Thermoplast. Compos. Mater.*, vol. 17, pp. 51–75, 2004, doi: 10.1177/0892705704033336.

[22] D. Grewell and A. Benatar, "Welding of Plastics : Fundamentals and New Developments," 2007.

[23] M. Rink, "Device for producing bonded parts," US005940949, 1999.

[24] J. Kweon, J. Jung, T. Kim, J. Choi, and D. Kim, "Failure of carbon composite-to-aluminum joints with combined mechanical fastening and adhesive bonding," vol. 75, pp. 192–198, 2006, doi: 10.1016/j.compstruct.2006.04.013.

[25] I. Paper, Y. Farazila, M. Fadzil, and M. Hamdi, "A Brief Review : Laser Joining of Polymer-Metal Structures," vol. 2, no. 2, pp. 5–12, 2012.

[26] S. Katayama and Y. Kawahito, "Laser direct joining of metal and plastic," *Scr. Mater.*, vol. 59, no. 12, pp. 1247–1250, 2008, doi: 10.1016/j.scriptamat.2008.08.026.

[27] C. Ageorges, L. Ye, and M. Hou, "Advances in fusion bonding techniques for joining thermoplastic matrix composites: a review." *Comp. Part A: App. Sci. Man.,* vol. 32, no. 6, pp. 439-857, 2001

[28] S. T. Amancio-Filho, C. Bueno, J. F. dos Santos, N. Huber, and E. Hage, "On the feasibility of friction spot joining in magnesium/fiber-reinforced polymer composite hybrid structures," *Mater. Sci. Eng. A*, vol. 528, pp. 3841–3848, 2011, doi: 10.1016/j.msea.2011.01.085.

[29] C. Ageorges and L. Ye, "Resistance welding of metal/thermoplastic composite joints," *J. Thermoplast. Compos. Mater.*, vol. 14, no. 6, pp. 449–475, 2001, doi: 10.1106/PN74-QXKH-7XBE-XKF5.

[30] J. Dutta Majumdar and I. Manna, "Laser processing of materials," *Sadhana*, vol. 28, no. 3–4, pp. 495–562, 2003, doi: 10.1007/BF02706446.

[31] S. Meco, L. Cozzolino, S. Ganguly, S. Williams, and N. McPherson, "Laser welding of steel to aluminium: Thermal modelling and joint strength analysis," *J. Mater. Process. Technol.*, vol. 247, pp. 121–133, 2017, doi: 10.1016/j.jmatprotec.2017.04.002.

[32] Z. Sun and J. C. Ion, "Laser welding of dissimilar metal combinations," *J. Mater. Sci.*, vol. 30, no. 17, pp. 4205–4214, 1995, doi: 10.1007/BF00361499.

[33] L. N. Trinh and D. Lee, "The characteristics of laser welding of a thin aluminum tab and steel battery case for lithium-ion battery," *Metals (Basel).*, vol. 10, no. 6, pp. 1–15, 2020, doi: 10.3390/met10060842.

[34] S. Arai, Y. Kawahito, and S. Katayama, "Effect of surface modification on laser direct joining of cyclic olefin polymer and stainless steel," *Mater. Des.*, vol. 59, pp. 448–453, 2014, doi: 10.1016/j.matdes.2014.03.018.

[35] K. W. Jung, Y. Kawahito, M. Takahashi, and S. Katayama, "Laser direct joining of carbon fiber reinforced plastic to zinc-coated steel," *Mater. Des.*, vol. 47, pp. 179–188, 2013, doi: 10.1016/j.matdes.2012.12.015.

[36] J. P. Bergmann and M. Stambke, "Potential of laser-manufactured polymer-metal hybrid joints," *Phys. Procedia*, vol. 39, pp. 84–91, 2012, doi: 10.1016/j.phpro.2012.10.017.

[37] E. Kannatey-Asibu, "Principles of Laser Materials Processing," *Wiley*, pp. 502–567, 2008, doi: 10.1002/9780470459300.

[38] A. P. Tadamalle, Y. P. Reddy, and E. Ramjee, "Influence of laser welding process parameters on weld pool geometry and duty cycle," *Adv. Prod. Eng. Manag.*, vol. 8, no. 1, pp. 52–60, 2013, doi: 10.14743/apem2013.1.153.

[39] C. Li, B. Li, Z. Wu, X. Qi, B. Ye, and A. Wang, "Stitch welding of Ti − 6Al − 4V titanium alloy by fiber laser," *Trans. Nonferrous Met. Soc. China*, vol. 27, no. 1, pp. 91–101, 2017, doi: 10.1016/S1003-6326(17)60010-4.

[40] Sivarao, Shukor, T. J. S. Anand, and Ammar, "DOE Based Statistical Approaches in Modeling of Laser Processing – Review & Suggestion," *Int. J. Eng. Technol.*, vol. 10, no. 4, 2010.

[41] K. F. Tamrin, Y. Nukman, and S. S. Zakariyah, "Laser Lap Joining of Dissimilar Materials – A Review of Factors Affecting Joint Strength," *Mater. Manuf. Process.*, vol 28, pp. 857–871, 2013, doi: 10.1080/10426914.2013.792413.

[42] Y. Cai, C. Huang, H. X. Liu, D. D. Meng, Y. W. Wu, and X. Wang, "Modeling and Optimization of Laser Direct Joining Process Parameters of Titanium Alloy and Carbon Fiber Reinforced Nylon Based on Response Surface Methodology," *Key Eng. Mater.*, vol. 620, pp. 3–9, 2014, doi: 10.4028/www.scientific.net/KEM.620.3.

[43] K. Y. Ã. Benyounis, A. G. Olabi, and M. S. J. Hashmi, "Multi-response optimization of CO 2 laser-welding process of austenitic stainless steel," vol. 40, pp. 76–87, 2008, doi: 10.1016/j.optlastec.2007.03.009.

[44] M. Schneider, L. Berthe, R. Fabbro, and M. Muller, "Measurement of laser absorptivity for operating parameters characteristic of laser drilling regime," *J. Phys. D. Appl. Phys.*, vol. 41, no. 15, 2008, doi: 10.1088/0022-3727/41/15/155502.

[45] J. T. Norris and C. V. Robino, "Development of a time resolved energy absorption measurement technique for laser beam spot welds," *ICALEO 2008 - 27th Int. Congr. Appl. Lasers Electro-Optics, Congr. Proc.*, pp. 153–159, 2008, doi: 10.2351/1.5061443.

[46] R. Fabbro, S. Slimani, I. Doudet, F. Coste, and F. Briand, "Experimental study of the dynamical coupling between the induced vapour plume and the melt pool for

Nd-Yag CW laser welding," *J. Phys. D. Appl. Phys.*, vol. 39, no. 2, pp. 394–400, 2006, doi: 10.1088/0022-3727/39/2/023.

[47] Y. Kawahito, K. Kinoshita, N. Matsumoto, M. Mizutani, and S. Katayama, "Effect of weakly ionised plasma on penetration of stainless steel weld produced with ultra high power density fibre laser," *Sci. Technol. Weld. Join.*, vol. 13, no. 8, pp. 749–753, 2008, doi: 10.1179/136217108X356971.

[48] V. V. Semak, J. A. Hopkins, M. H. McCay, and T. D. McCay, "Melt pool dynamics during laser welding," *J. Phys. D. Appl. Phys.*, vol. 28, no. 12, pp. 2443–2450, 1995, doi: 10.1088/0022-3727/28/12/008.

[49] R. Fabbro, "Melt pool and keyhole behaviour analysis for deep penetration laser welding," *J. Phys. D. Appl. Phys.*, vol. 43, no. 44, 2010, doi: 10.1088/0022-3727/43/44/445501.

[50] J. Dowden, N. Postacioglu, M. Davis, and P. Kapadia, "A keyhole model in penetration welding with a laser," *J. Phys. D. Appl. Phys.*, vol. 20, no. 1, pp. 36–44, 1987, doi: 10.1088/0022-3727/20/1/006.

[51] S. Fujinaga, H. Takenaka, T. Narikiyo, S. Katayama, and A. Matsunawa, "Direct observation of keyhole behaviour during pulse modulated high-power Nd:YAG laser irradiation," *J. Phys. D. Appl. Phys.*, vol. 33, no. 5, pp. 492–497, 2000, doi: 10.1088/0022-3727/33/5/304.

[52] W. M. Steen, "Laser material processing - An overview," *J. Opt. A Pure Appl. Opt.*, vol. 5, no. 4, 2003, doi: 10.1088/1464-4258/5/4/351.

[53] J. C. Ion, "Laser Processing Diagrams," *Laser Process. Eng. Mater.*, pp. 178–187, 2005, doi: 10.1016/b978-075066079-2/50009-x.

[54] M. F. Ashby and K. E. Easterling, "The transformation hardening of steel surfaces by laser beams-I. Hypo-eutectoid steels," *Acta Metall.*, vol. 32, no. 11, 1984, doi: 10.1016/0001-6160(84)90175-5.

[55] R. McBride, F. Bardin, M. Gross, D. P. Hand, J. D. C. Jones, and A. J. Moore, "Modelling and calibration of bending strains for iterative laser forming," *J. Phys. D. Appl. Phys.*, vol. 38, no. 22, pp. 4027–4036, 2005, doi: 10.1088/0022-3727/38/22/005.

[56] N. Jebbari, M. M. Jebari, F. Saadallah, A. Tarrats-Saugnac, R. Bennaceur, and J. P. Longuemard, "Thermal affected zone obtained in machining steel XC42 by high-power continuous CO2 laser," *Opt. Laser Technol.*, vol. 40, no. 6, pp. 864–873, 2008, doi: 10.1016/j.optlastec.2007.11.006.

[57] R. Fabbro and K. Chouf, "Dynamical description of the keyhole in deep penetration laser welding," *J. Laser Appl.*, vol. 12, no. 4, pp. 142–148, 2000, doi: 10.2351/1.521924.

[58] W. J. Suder and S. W. Williams, "Investigation of the effects of basic laser material interaction parameters in laser welding," *J. Laser Appl.*, vol. 24, no. 3, p. 032009, 2012, doi: 10.2351/1.4728136.

[59] F. Lambiase and S. Genna, "Experimental analysis of laser assisted joining of Al-Mg aluminium alloy with Polyetheretherketone (PEEK)," *Int. J. Adhes. Adhes.*, vol. 84, pp. 265–274, 2018, doi: 10.1016/j.ijadhadh.2018.04.004.

[60] X. Wang, P. Li, Z. Xu, X. Song, and H. Liu, "Laser transmission joint between PET

and titanium for biomedical application," *J. Mater. Process. Technol.*, vol. 210, no. 13, pp. 1767–1771, 2010, doi: 10.1016/j.jmatprotec.2010.06.007.

[61] K. Schricker and J. P. Bergmann, "Temperature- and Time-Dependent Penetration of Surface Structures in Thermal Joining of Plastics to Metals," *Key Eng. Mater.*, vol. 809, pp. 378–385, 2019, doi: 10.4028/www.scientific.net/KEM.809.378.

[62] K. Schricker and J. P. Bergmann, "Determination of sensitivity and thermal efficiency in laser assisted metal-plastic joining by numerical simulation," *Procedia CIRP*, vol. 74, pp. 511–517, 2018, doi: 10.1016/j.procir.2018.08.133.

[63] P. Norman, H. Engström, and A. F. H. Kaplan, "State-of-the-art of monitoring and imaging of laser welding defects," *11th NOLAMP Conf. Laser Process. Mater.*, December 2014, pp. 20–22, 2007.

[64] K. Schricker, S. Diller, and J. P. Bergmann, "Bubble formation in thermal joining of plastics with metals," *Procedia CIRP*, vol. 74, pp. 518–523, 2018, doi: 10.1016/j.procir.2018.08.132.

[65] C. Lamberti, I. Peral Alonso, and P. Plapper, "Influence of Material Moisture during Laser Joining of Polyamide 6.6 to Aluminum," *ATINER'S Conf. Pap. Ser. No IND2017-2270*, no. November, pp. 1–11, 2017.

[66] D. V. Srinivasan, V. Ravichandran, and S. Idapalapati, "Failure analysis of GFRP single lap joints tailored with a combination of tough epoxy and hyperelastic adhesives," *Compos. Part B Eng.*, vol. 200, no. June, p. 108255, 2020, doi: 10.1016/j.compositesb.2020.108255.

[67] J. P. H. Belnoue and S. R. Hallett, "Cohesive/adhesive failure interaction in ductile adhesive joints Part I: A smeared-crack model for cohesive failure," *Int. J. Adhes. Adhes.*, vol. 68, pp. 359–368, 2016, doi: 10.1016/j.ijadhadh.2016.03.009.

[68] K. Schricker, L. Samfaß, M. Grätzel, G. Ecke, and J. P. Bergmann, "Bonding mechanisms in laser-assisted joining of metal-polymer composites," *J. Adv. Join. Process.*, vol. 1, no. January, p. 100008, 2020, doi: 10.1016/j.jajp.2020.100008.

[69] A. Al-Sayyad, J. Bardon, P. Hirchenhahn, K. Santos, L. Houssiau, and P. Plapper, "Aluminum pretreatment by a laser ablation process: influence of processing parameters on the joint strength of laser welded aluminum – polyamide assemblies," *Procedia CIRP*, vol. 74, pp. 495–499, 2018, doi: 10.1016/j.procir.2018.08.136.

[70] M. Wahba, Y. Kawahito, and S. Katayama, "Laser direct joining of AZ91D thixomolded Mg alloy and amorphous polyethylene terephthalate," *J. Mater. Process. Technol.*, vol. 211, no. 6, pp. 1166–1174, 2011, doi: 10.1016/j.jmatprotec.2011.01.021.

[71] Y. J. Chen, T. M. Yue, and Z. N. Guo, "A new laser joining technology for direct-bonding of metals and plastics," *Mater. Des.*, vol. 110, pp. 775–781, 2016, doi: 10.1016/j.matdes.2016.08.018.

[72] A. Klotzbach, M. Langer, R. Pautzsch, J. Standfuß, and E. Beyer, "Thermal direct joining of metal to fiber reinforced thermoplastic components," *J. Laser Appl.*, vol. 022421, no. 806, 2017, doi: 10.2351/1.4983243.

[73] K. Schricker, J. P. Bergmann, M. Hopfeld, and L. Spieß, "Effect of thermoplastic morphology on mechanical properties in laser-assisted joining of polyamide 6 with

aluminum," *Weld. World*, 2020, doi: 10.1007/s40194-020-01048-1.

[74] K. Schricker, M. Stambke, and J. P. Bergmann, "Adjustment and Impact of the Thermoplastic Microstructure of the Melting Layer in Laser-based Joining of Polymers to Metals," LIM Conf., 2015.

[75] K. Schricker, M. Stambke, J. P. Bergmann, and K. Bräutigam, "Laser-Based Joining of Thermoplastics to Metals: Influence of Varied Ambient Conditions on Joint Performance and Microstructure," *Int. J. Polym. Sci.*, vol. 2016, pp. 0–9, 2016, doi: 10.1155/2016/5301081.

[76] K. Schricker, M. Stambke, and J. P. Bergmann, "Experimental investigations and modeling of the melting layer in polymer-metal hybrid structures," *Weld. World*, vol. 59, no. 3, pp. 407–412, 2015, doi: 10.1007/s40194-014-0213-0.

[77] K. Schricker, J. P. Bergmann, M. Hopfeld, and L. Spieß, "Characterization of the Joining Zone in Laser Direct Joining Between Thermoplastics and Metals," *Hybrid Mater. Struct. 2018*, pp. 2–7, 2018, [Online]. Available: https://hybrid2018.dgm.de/fileadmin/Tagungen/2018/2018-04_Hybrid_Materials/02_Druckwerke/2018-Hybrid-Proceedings.pdf.

[78] A. Pizzi and K. L. Mittal, *Handbook of Adhesive Technology*. Marcel Dekker, 2003.

[79] J. W. McBain and D. G. Hopkins, "On Adhesives and Adhesive Action," *J. Phys. Chem*, vol. 29, no. 2, pp. 188–204, 1925.

[80] K. Schricker, M. Stambke, J. P. Bergmann, K. Bräutigam, and P. Henckell, "Macroscopic surface structures for polymer-metal hybrid joints manufactured by laser based thermal joining," *Phys. Procedia*, vol. 56, pp. 782–790, 2014, doi: 10.1016/j.phpro.2014.08.086.

[81] A. Roesner, S. Scheik, A. Olowinsky, A. Gillner, U. Reisgen, and M. Schleser, "Laser assisted joining of plastic metal hybrids," *Phys. Procedia*, vol. 12, pp. 373–380, 2011, doi: 10.1016/j.phpro.2011.03.146.

[82] C. W. Chan and G. C. Smith, "Fibre laser joining of highly dissimilar materials: Commercially pure Ti and PET hybrid joint for medical device applications," *Mater. Des.*, vol. 103, pp. 278–292, 2016, doi: 10.1016/j.matdes.2016.04.086.

[83] J. Holtkamp, A. Roesner, and A. Gillner, "Advances in hybrid laser joining," *Int. J. Adv. Manuf. Technol.*, vol. 47, no. 9–12, pp. 923–930, 2010, doi: 10.1007/s00170-009-2124-6.

[84] L. H. Sharpe and H. Schonhorn, "Surface Energetics, Adhesion, and Adhesive Joints," *Adv. Chem.*, vol. 43, pp. 189–201, 1964, doi: 10.1021/ba-1964-0043.ch012.

[85] E. Petrie, *Handbook of adhesives and selants*. McGraw Hill Professional, 2007.

[86] Z. Zhang, J. Shan, and X. Tan, "Evaluation of the CFRP grafting and its influence on the laser joining CFRP to aluminum alloy," *J. Adhes. Sci. Technol.*, vol. 4243, no. September, pp. 1–17, 2017, doi: 10.1080/01694243.2017.1357457.

[87] A. Ahagon and A. N. Gent, "Effect of interfacial bonding on the strength of adhesion," *Polym. physics, J. Polym. Sci.*, 1975.

[88] C. Lamberti, T. Solchenbach, P. Plapper, and W. Possart, "Laser Assisted Joining of Hybrid Polyamide-Aluminum Structures," *Phys. Procedia*, vol. 56, no. 8, pp. 845–853, 2014, doi: 10.1016/j.phpro.2014.08.103.

[89] P. Hirchenhahn, “Fundamental study of the adhesion phenomena in polymer-metal hybrid materials obtained by laser welding,” PhD dissertation, UNamur, 2020.

[90] P. Hirchenhahn, A. Al-sayyad, J. Bardon, A. Felten, P. Plapper, and L. Houssiau, “Highlighting chemical bonding between nylon-6.6 and the native oxide from an aluminum sheet assembled by laser welding,” *Appl. Polym. Mater*, vol. 2, no. 7, pp. 2517–2527, 2020, doi: 10.1021/acsapm.0c00015.

[91] S. S. Voyutskii and V. L. Vakula, “The role of diffusion phenomena in polymer-to-polymer adhesion,” *J. Appl. Polym. Sci.*, vol. 7, no. 2, pp. 475–491, 1963, doi: 10.1002/app.1963.070070207.

[92] Z. Zhang, J. G. Shan, X. H. Tan, and J. Zhang, “Effect of anodizing pretreatment on laser joining CFRP to aluminum alloy A6061,” *Int. J. Adhes. Adhes.*, vol. 70, pp. 142–151, 2016, doi: 10.1016/j.ijadhadh.2016.06.007.

[93] B. V. Derjaguin and V. P. Smilga, “Electronic theory of adhesion,” *J. Appl. Phys.*, vol. 38, no. 12, pp. 4609–4616, 1967, doi: 10.1063/1.1709192.

[94] J. Bikerman, *The Science of Adhesive Joints,* 2nd Edition. Cleveland, Ohio: Academic Press, 1968.

[95] A. V. Pocius, *Adhesion and Adhesives Technology*, 3rd Edition. Munich: Hanser Publications, 1987.

[96] A. Cenigaonaindia, F. Liébana, A. Lamikiz, and Z. Echegoyen, “Novel Strategies for Laser Joining of Polyamide and AISI 304,” *Phys. Procedia*, vol. 39, pp. 92–99, 2012, doi: 10.1016/j.phpro.2012.10.018.

[97] K. W. Allen, S. Y. T. Chan, and K. B. Armstrong, “Cold-setting adhesives for repair purposes using , various surface preparation methods,” *Inter. J. Adhes. Adhes.,* vol. 2, no. 4, pp. 239–248, 1982.

[98] T. H. Ramarathnam, G.; Libertucci, M.; Sadowski, M. M.; North, “Joining of Polymers to Metal,” *Weld. Res. Suppl.*, no. 2, pp. 483–490, 1992, [Online]. Available: http://www.aws.org/wj/supplement/WJ_1992_12_s483.pdf.

[99] J. D. Venables, “Review Adhesion and durability of metal-polymer bonds,” *J. Mater. Sci.*, vol. 19, pp. 2431–2453, 1984.

[100] D. J. Jung, J. Cheon, and S. J. Na, “Effect of surface pre-oxidation on laser assisted joining of acrylonitrile butadiene styrene (ABS) and zinc-coated steel,” *Mater. Des.*, vol. 99, pp. 1–9, 2016, doi: 10.1016/j.matdes.2016.03.044.

[101] M. Hino, Y. Mitooka, K. Murakami, K. Urakami, H. Nagase, and T. Kanadani, “Effect of aluminum surface state on laser joining between 1050 aluminum sheet and polypropylene resin sheet using insert materials,” *Mater. Trans.*, vol. 52, no. 5, pp. 1041–1047, 2011, doi: 10.2320/matertrans.L-M2011804.

[102] C. Magnus, “Feasibility Study of Metal to Polymer Hybrid Joining,” M.Sc thesis, Lappeenranta Univ. of Tech., 2012.

[103] M. Hinge, K. Kristensen, K. Daasbjerg, S. U. Pedersen, M. Strange, and S.-E. Nielsen, “Patent no.: US 2015.0050507A1; Joining of Polymer and Surface Modified Metal by Laser Welding,” 2015.

[104] P. Amend, S. Pfindel, and M. Schmidt, “Thermal joining of thermoplastic metal hybrids by means of mono- and polychromatic radiation,” *Phys. Procedia*, vol. 41,

pp. 98–105, 2013, doi: 10.1016/j.phpro.2013.03.056.

[105] J. Comyn, L. Mascia, G. Xiao, and B. M. Parker, "Corona-discharge treatment of polyetheretherketone (PEEK) for adhesive bonding," *Int. J. Adhes. Adhes.*, vol. 16, no. 4, pp. 301–304, 1996, doi: 10.1016/S0143-7496(96)00010-3.

[106] A. Popelka *et al.*, "Improvement of aluminum/polyethylene adhesion through corona discharge," *J. Phys. D. Appl. Phys.*, vol. 50, no. 3, p. 035204, 2017, doi: 10.1088/1361-6463/50/3/035204.

[107] A. Popelka, I. Novák, M. A. S. A. Al-Maadeed, M. Ouederni, and I. Krupa, "Effect of corona treatment on adhesion enhancement of LLDPE," *Surf. Coatings Technol.*, vol. 335, pp. 118–125, 2018, doi: 10.1016/j.surfcoat.2017.12.018.

[108] A. P. Pijpers and R. J. Meier, "Adhesion behaviour of polypropylenes after flame treatment determined by XPS(ESCA) spectral analysis," *J. Electron Spectros. Relat. Phenomena*, vol. 121, no. 1–3, pp. 299–313, 2001, doi: 10.1016/S0368-2048(01)00341-3.

[109] I. Sutherland, D. M. Brewis, R. J. Health, and E. Sheng, "Modification of polypropylene surfaces by flame treatment," *Surf. Interface Anal.*, vol. 17, no. 7, pp. 507–510, 1991, doi: 10.1002/sia.740170717.

[110] M. Morra, E. Occhiello, and F. Garbassi, "Contact Angle Hysteresis in Oxygen Plasma Treated Poly(tetrafluoroethylene)," *J. Colloid Interface Sci.*, vol. 132, no. 2, pp. 504–508, 1989, doi: 10.1021/la00087a050.

[111] M. Thomas and K. L. Mittal, *Atmospheric Pressure Plasma Treatment of Polymers: Relevance to Adhesion*. Wiley, 2013.

[112] C. Sperandio, J. Bardon, A. Laachachi, H. Aubriet, and D. Ruch, "Influence of plasma surface treatment on bond strength behaviour of an adhesively bonded aluminium-epoxy system," *Int. J. Adhes. Adhes.*, vol. 30, no. 8, pp. 720–728, 2010, doi: 10.1016/j.ijadhadh.2010.07.004.

[113] M. Moreno-couranjou, N. D. Boscher, D. Duday, R. Maurau, E. Lecoq, and P. Choquet, "Atmospheric Pressure Plasma Polymerization Surface Treatments by Dielectric Barrier Discharge for Enhanced Polymer-Polymer and Metal-Polymer Adhesion," in *Atmospheric Pressure Plasma Treatment of Polymers: Relevance to Adhesion: Wiley*, 2013, pp. 219–249.

[114] J. R. Vig and J. W. LE BUS, "UV / Ozone of Surfaces," *IEEE Trans. Parts, Hybrids, Packag.*, vol. 12, no. 4, 1976.

[115] T. Cui, Q. Li, and Y. Xuan, "Characterization and application of engineered regular rough surfaces in thermal contact resistance," *Appl. Therm. Eng.*, vol. 71, no. 1, pp. 400–409, 2014, doi: 10.1016/j.applthermaleng.2014.07.020.

[116] P. Zhang, T. Cui, and Q. Li, "Effect of surface roughness on thermal contact resistance of aluminium alloy," *Appl. Therm. Eng.*, vol. 121, pp. 992–998, 2017, doi: 10.1016/j.applthermaleng.2017.04.142.

[117] R. Prasher, "Thermal interface materials: Historical perspective, status, and future directions," *Proc. IEEE*, vol. 94, no. 8, pp. 1571–1586, 2006, doi: 10.1109/JPROC.2006.879796.

[118] M. M. Yovanovich, "Four decades of research on thermal contact, gap, and joint resistance in microelectronics," *IEEE Trans. Components Packag. Technol.*, vol. 28,

no. 2, pp. 182–206, 2005, doi: 10.1109/TCAPT.2005.848483.

[119] J. A. Greenwood and J. B. P. Williamson, "Contact of nominally flat surfaces," *Proc. R. Soc. London. Ser. A. Math. Phys. Sci.*, vol. 295, no. 1442, pp. 300–319, 1966, doi: 10.1098/rspa.1966.0242.

[120] J. A. Greenwood, "The Area of Contact Between Rough Surfaces and Flats," *J. Lubr. Tech*, vol. 89, no. 1, pp. 81–87, 1967.

[121] J. A. Greenwood and J. H. Tripp, "The Contact of Two Nominally Flat Surfaces," *Proc lnstn Mech Engr*, vol. 185, pp. 625–633, 1970, doi: 10.1016/0147-5975(81)90037-2.

[122] M. G. Cooper, B. B. Mikic, and M. M. Yovanovich, "Thermal contact conductance," *Int. J. Heat Mass Transf.*, vol. 12, no. 3, pp. 279–300, 1969, doi: 10.1016/0017-9310(69)90011-8.

[123] B. B. Mikić, "Thermal contact conductance; theoretical considerations," *Int. J. Heat Mass Transf.*, vol. 17, no. 2, pp. 205–214, 1974, doi: 10.1016/0017-9310(74)90082-9.

[124] R. S. Sayles and T. R. Thomas, "Thermal conductance of a rough elastic contact," *Appl. Energy*, vol. 2, no. 4, pp. 249–267, 1976, doi: 10.1016/0306-2619(76)90012-X.

[125] M. M. Yovanovich and E. E. Marotta, "Thermal spreading and contact resistances," in *Heat Transfer Handbook*, A. Bejan and A. D. Kraus, Eds. New Jersey: Wiley, 2003, pp. 261–395.

[126] R. A. Fisher, "The arrangement of field experiments," *J. Minist. Agric.*, vol. 33, pp. 503–515, 1965.

[127] R. A. Fisher, *The Design of Experiments*. 1935.

[128] G. E. P. Box and K. B. Wilson, "On the Experimental Attainment of Optimum Conditions," *J. R. Stat. Soc. Ser. B*, vol. 13, no. 1, pp. 1–38, 1951, doi: 10.1111/j.2517-6161.1951.tb00067.x.

[129] B. Jones and C. J. Nachtsheim, "A class of three-level designs for definitive screening in the presence of second-order effects," *J. Qual. Technol.*, vol. 43, no. 1, pp. 1–15, 2011, doi: 10.1080/00224065.2011.11917841.

[130] R. L. Plackett and J. P. Burman, "The Design of Optimum Multifactorial Experiments," *Biometrika*, vol. 33, no. 4, pp. 305–325, 1946.

[131] R. H. Myers, D. C. Montgomery, and C. M. Anderson-Cook, *Response Surface Methodology*. Wiley, 2009.

[132] C. Lamberti, "Laserstrahl gefügten Verbindung zwischen Aluminium und Polyamid sowie die Untersuchung des Interaktionsmechanismus zwischen beiden Materialien in der Grenzschicht," Ph.D. dissertation, Univ. of Luxembourg, 2017.

[133] R. T. Sataloff, M. M. Johns, and K. M. Kost, *Metals Handbook Desk Edition*, 2nd ed. ASM international, 1998.

[134] R. Boyer, G. Welsch, and E. W. Collings, *Materials properties handbook : titanium alloys*. ASM international, 1994.

[135] J. Pearl, "Simpson's Paradox, Confounding, and Collapsibility," in *Causality*, 2nd ed., Cambridge: Cambridge University Press, 2009, pp. 173–200.

[136] G. C. R. A. N. Strohm, M. Fredriksson, and P. E. R. Stenius, “Contact Angles , Work of Adhesion , and Interfacial Tensions at a Dissolving Hydrocarbon Surface,” J. of Coll. and Inter. Sci., vol. 119, no. 2, pp. 352–361, 1987.

[137] “ISO 4287–Geometrical Product Specifications (GPS) — Surface texture: Profile method — Terms, definitions and surface texture parameters,” Geneva, Switzerland, 1997.

[138] W. J. Parker, R. J. Jenkins, C. P. Butler, and G. L. Abbott, “Flash method of determining thermal diffusivity, heat capacity, and thermal conductivity,” *J. Appl. Phys.*, vol. 32, no. 9, pp. 1679–1684, 1961, doi: 10.1063/1.1728417.

[139] S. F. Corbin and Dennis M. T., “Thermal Diffusivity by the Laser Flash Technique,” *Charact. Mater.*, 2002, doi: 10.1002/0471266965.com102.

[140] J. Hartmann, O. Nilsson, and J. Fricke, “Thermal Diffusivity Measurements on Two-Layered and Three-Layered Systems with the Laser-Flash Method,” *High Temp. Press.*, vol. 25, p. 403-410, 1993, [Online]. Available: https://www.researchgate.net/publication/260087738_Thermal_Diffusivity_Measurements_on_Two-Layered_and_Three-Layered_Systems_with_the_Laser-Flash_Method.

[141] R. V Lenth, “Quick and Easy Analysis of Factorials Unreplicated,” *Technometrics*, vol. 31, no. 4, pp. 469–473, 1989.

[142] J. Blackburn *et al.*, “Nd : YAG laser welding of titanium alloys using a directed gas jet,” *J. Laser Appl.*, vol. 22, no. 71, pp. 71–78, 2013, doi: 10.2351/1.3455825.

[143] B. R. Strohmeier, “Improving the wettability of aluminum foil with oxygen plasma treatments,” J. of Adhes. Sci. and Tech., vol. 6, pp. 37–41, 2012, doi: 10.1163/156856192X01051.

[144] J. Antony, *Design of Experiments for Engineers and Scientists*.: Elsevier, 2003.

[145] N. Maharjan, W. Zhou, Y. Zhou, and Y. Guan, “Ablation morphology and ablation threshold of Ti-6Al-4V alloy during femtosecond laser processing,” *Appl. Phys. A Mater. Sci. Process.*, vol. 124, no. 8, pp. 1–10, 2018, doi: 10.1007/s00339-018-1928-3.

[146] C. Zwahr, R. Helbig, C. Werner, and A. F. Lasagni, “Fabrication of multifunctional titanium surfaces by producing hierarchical surface patterns using laser based ablation methods,” *Sci. Rep.*, vol. 9, no. 1, pp. 1–13, 2019, doi: 10.1038/s41598-019-43055-3.

[147] B. Zheng, G. Jiang, W. Wang, K. Wang, and X. Mei, “Ablation experiment and threshold calculation of titanium alloy irradiated by ultra-fast pulse laser,” *AIP Adv.*, vol. 4, no. 3, 2014, doi: 10.1063/1.4867088.

[148] M. A. Jafarabadi and M. H. Mahdieh, “Evaluation of Crater Width in Nanosecond Laser Ablation of Ti in Liquids and the Effect of Light Absorption by Ablated Nano-Particles,” *Int. J. Opt. Photonics*, vol. 7, no. 2, pp. 105–112, 2013.

[149] B. R. Strohmeier, “An ESCA Method for Determining the Oxide Thickness on Aluminum Alloys,” *Surf. Interface Anal.*, vol. 15, no. July 1989, pp. 51–56, 1990.

[150] B. D. Ratner and D. G. Castner, “Electron Spectroscopy for Chemical Analysis,” in *Surface Analysis– The Principal Techniques*, Chichester, UK: John Wiley & Sons, Ltd, 2009, pp. 47–112.

[151] J. A. King, *Materials Handbook for Hybrid Microelectronics*. Boston: Artech House, 1988.

[152] M. Bereznai *et al.*, "Surface modifications induced by ns and sub-ps excimer laser pulses on titanium implant material," *Biomaterials*, vol. 24, no. 23, pp. 4197–4203, 2003, doi: 10.1016/S0142-9612(03)00318-1.

Appendix

Appendix A

Regions investigated by EDX to determine failure mode in plasma pretreated and laser-ablated aluminum welded to solvent cleaned polyamide.

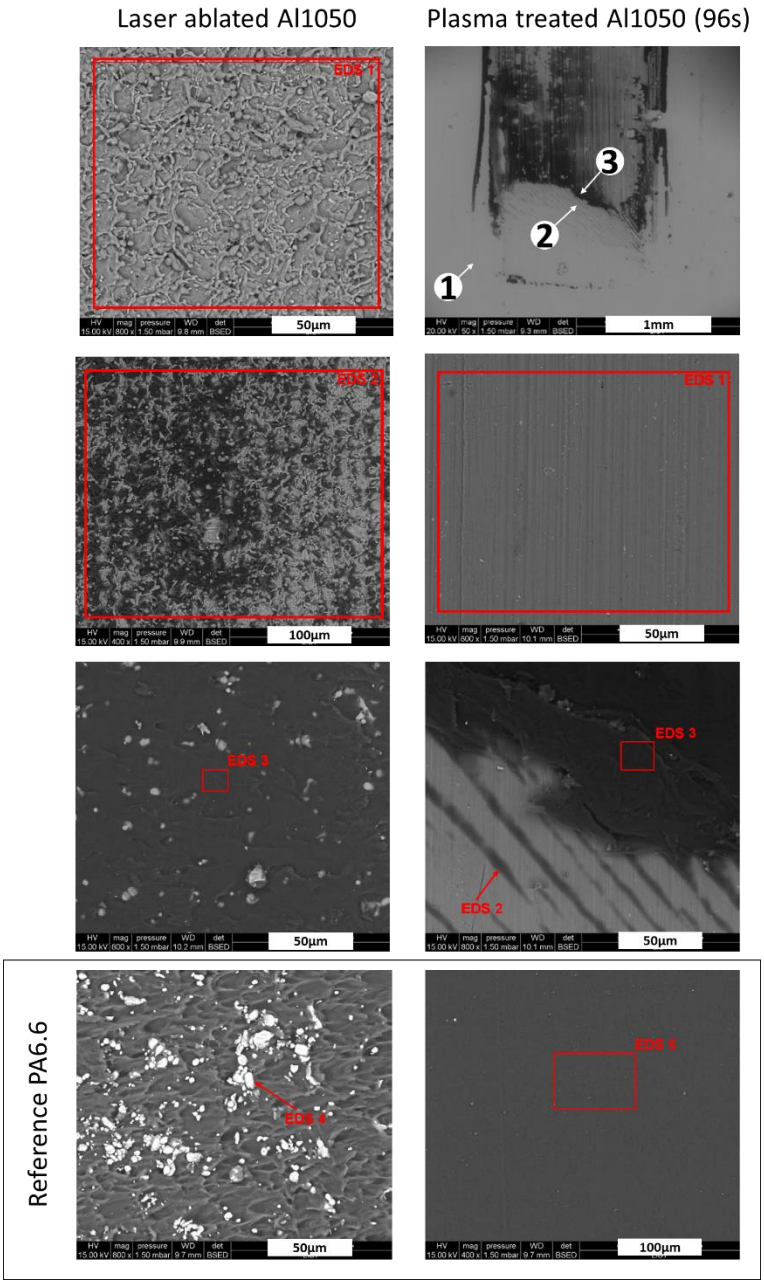

Figure 69: regions investigated with EDX in pretreated Al1050 and PA6.6 (§5.2.5)

Appendix B

XPS survey spectra and high-resolution spectra of pretreated aluminum samples.

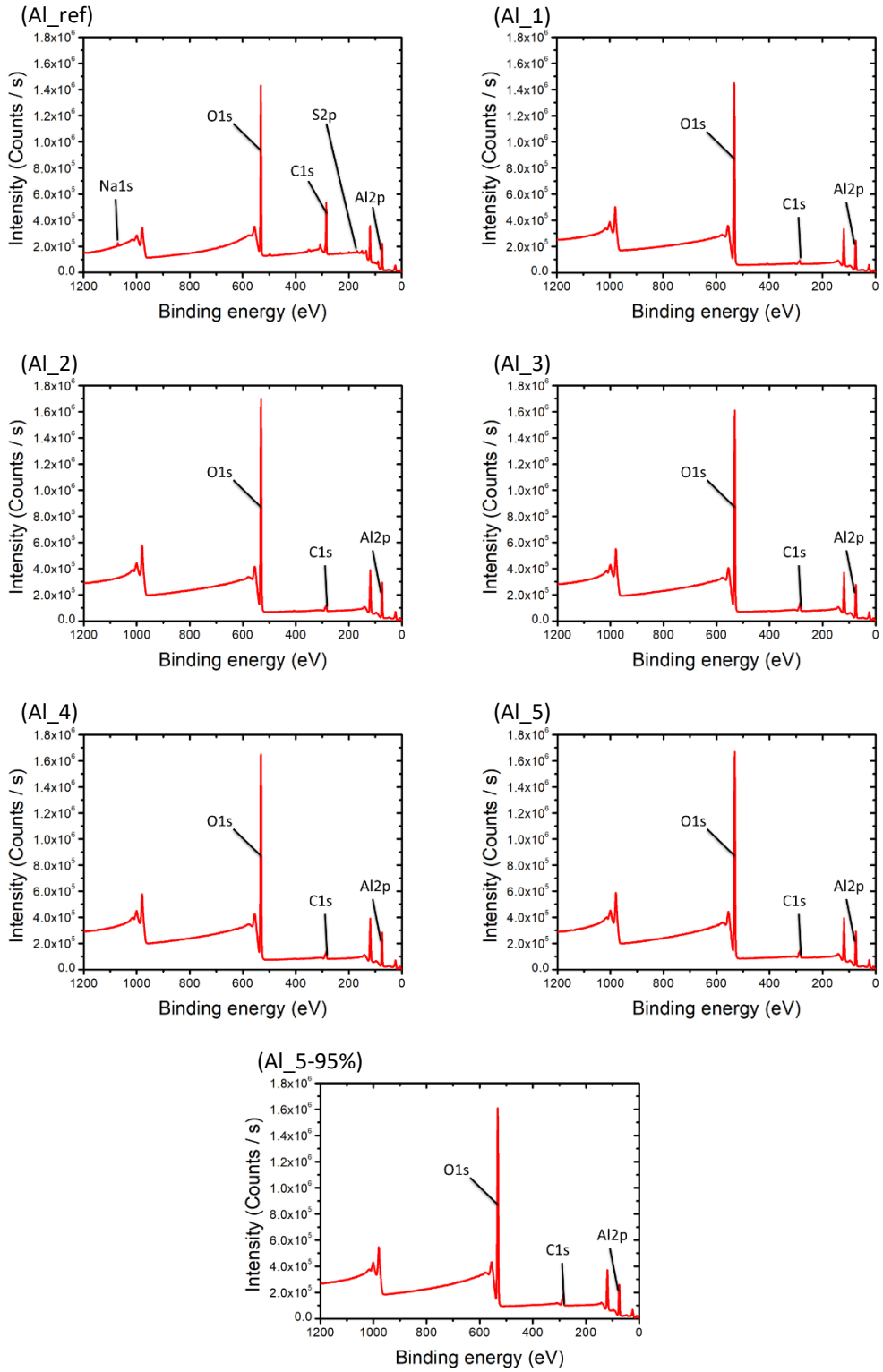

Figure 70: XPS survey spectra of pretreated aluminum (pretreatment attributes are indicated in Table 19, §5.4)

To interpret the spectra in the reference, three contribution were used: a CC/C-H one set at 284.8 eV (serving as calibration peak), a C-O/C-N peak at 285.7 eV and a O-C=O

contribution at 288.6 eV. For the ablated samples only two peaks were used to fit the spectra: a C-C/C-H contribution at 284.8 eV and O-C=O contribution around 288.9 eV

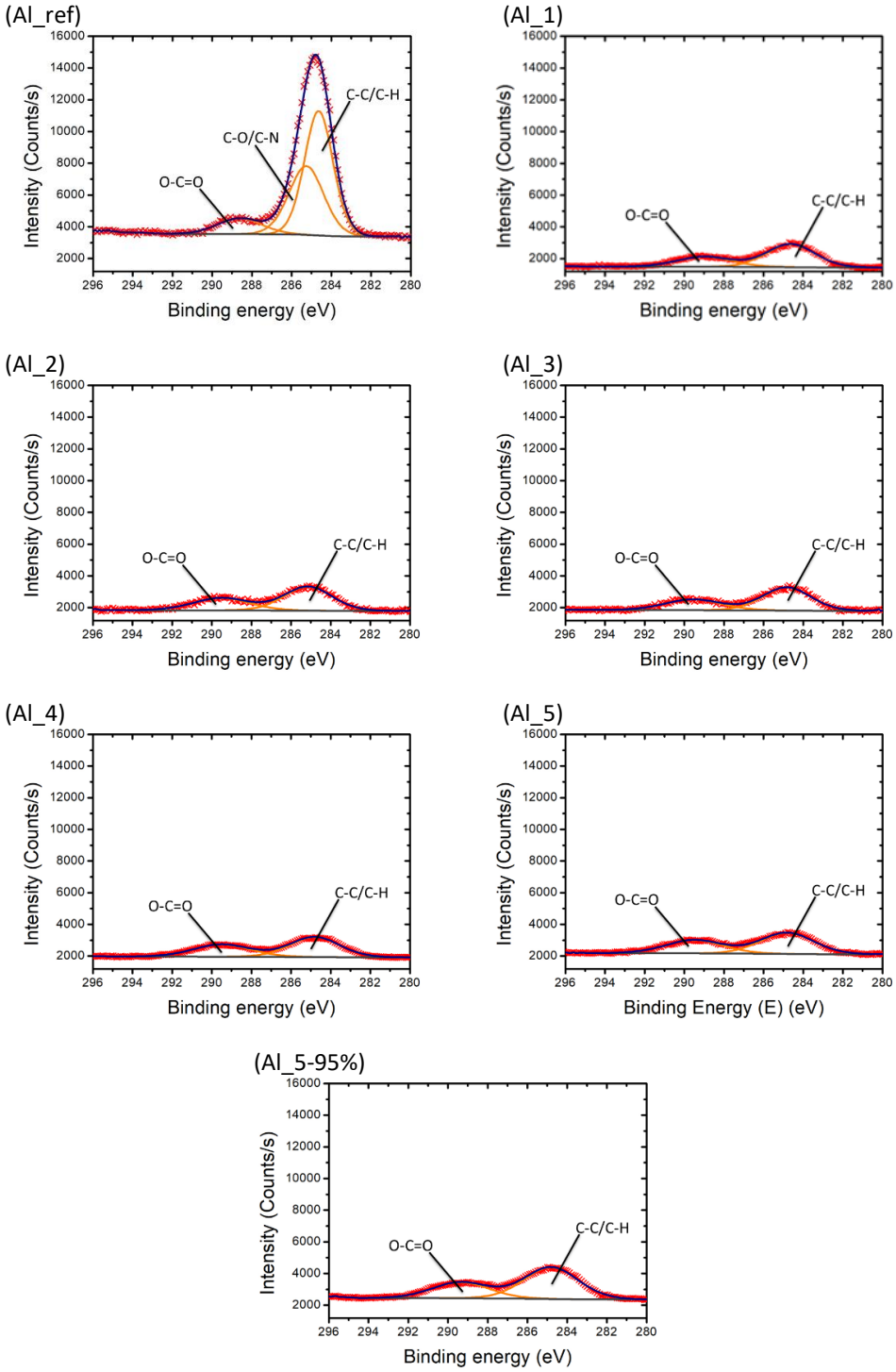

Figure 71: XPS high resolution spectra of the C 1s region for pretreated aluminum (pretreatment attributes are indicated in Table 19, §5.4)

For the fitting of the O 1s regions of all the samples, only two contributions were used: one associated to aluminum oxide and one linked to hydroxide, at slightly varying binding energies.

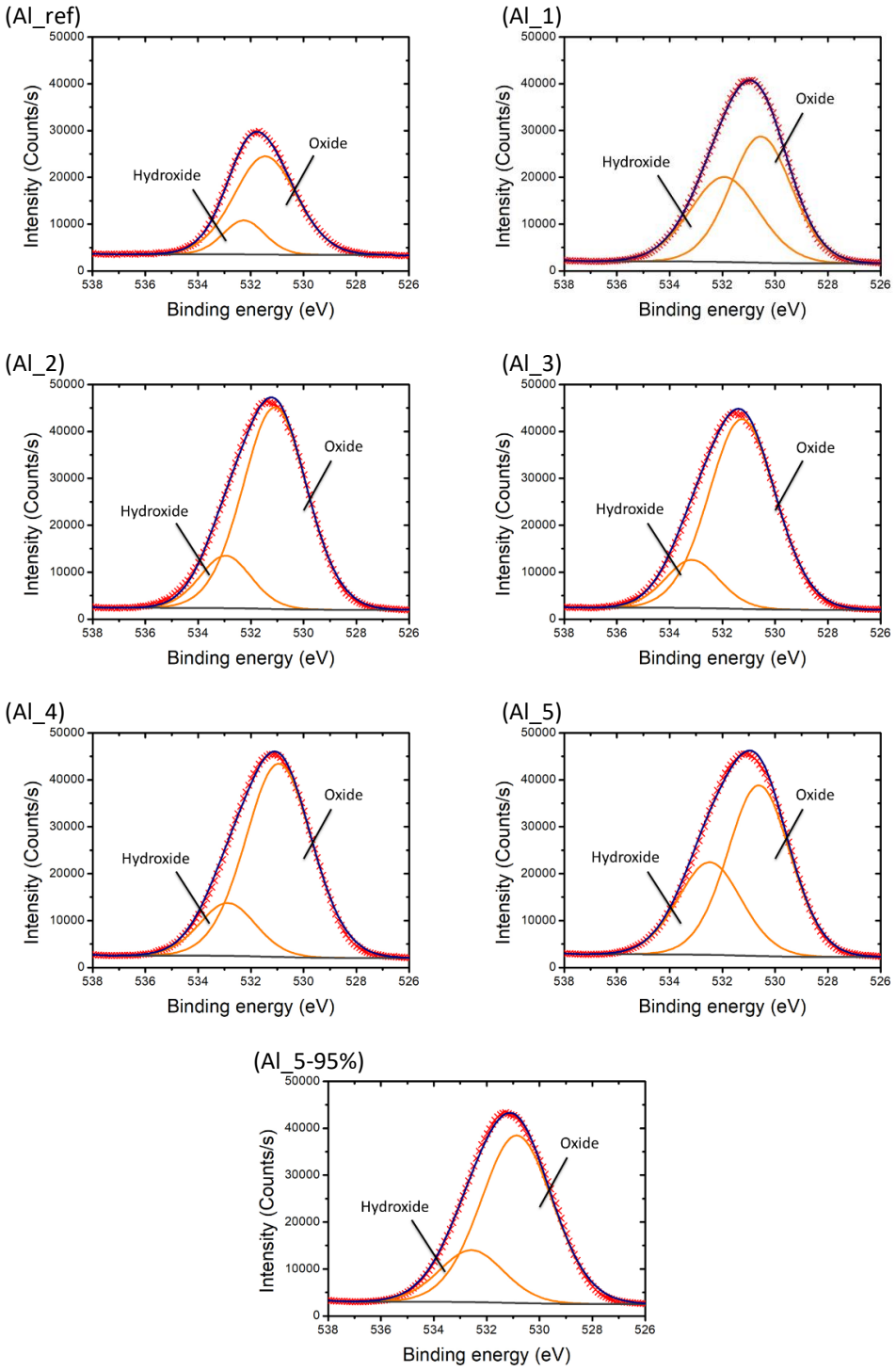

Figure 72: XPS high resolution spectra of the O 1s region for pretreated aluminum (pretreatment attributes are indicated in Table 19, §5.4)

To fit the spectra of the reference sample, two metallic aluminum peaks are associated to Al 2p3/2 and Al 2p3/2 respectively at 72.9 eV and 73.3 eV, and the third contribution is related to oxidized aluminum at 75.0 eV. On the ablated samples a single contribution, associated to oxidized aluminum, was used to fit the spectra around 74.2 eV.

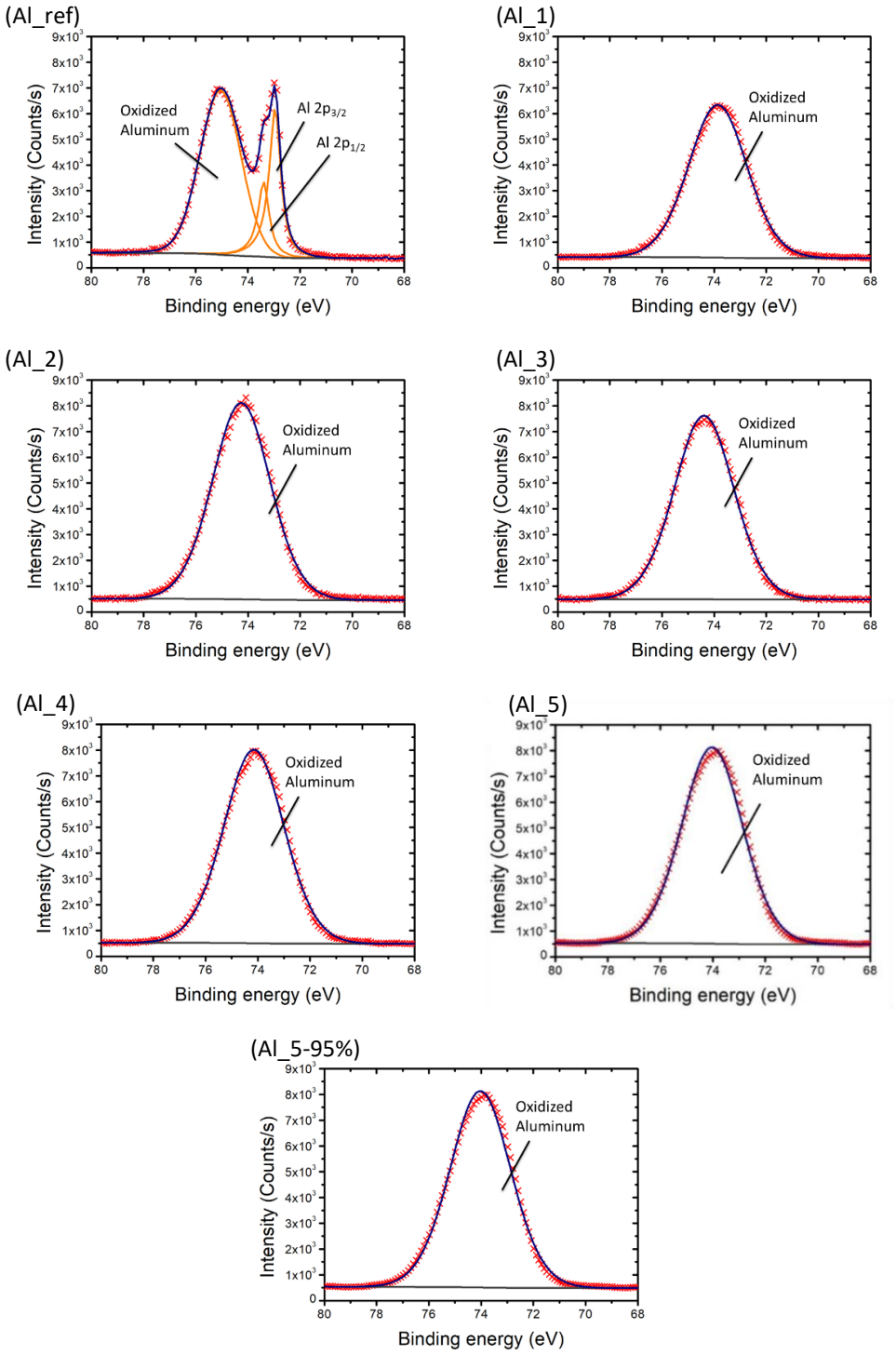

Figure 73: XPS high resolution spectra of the Al 2p region for pretreated aluminum (pretreatment attributes are indicated in Table 19, §5.4)

Appendix C

XPS survey spectra and high-resolution spectra of pretreated titanium samples.

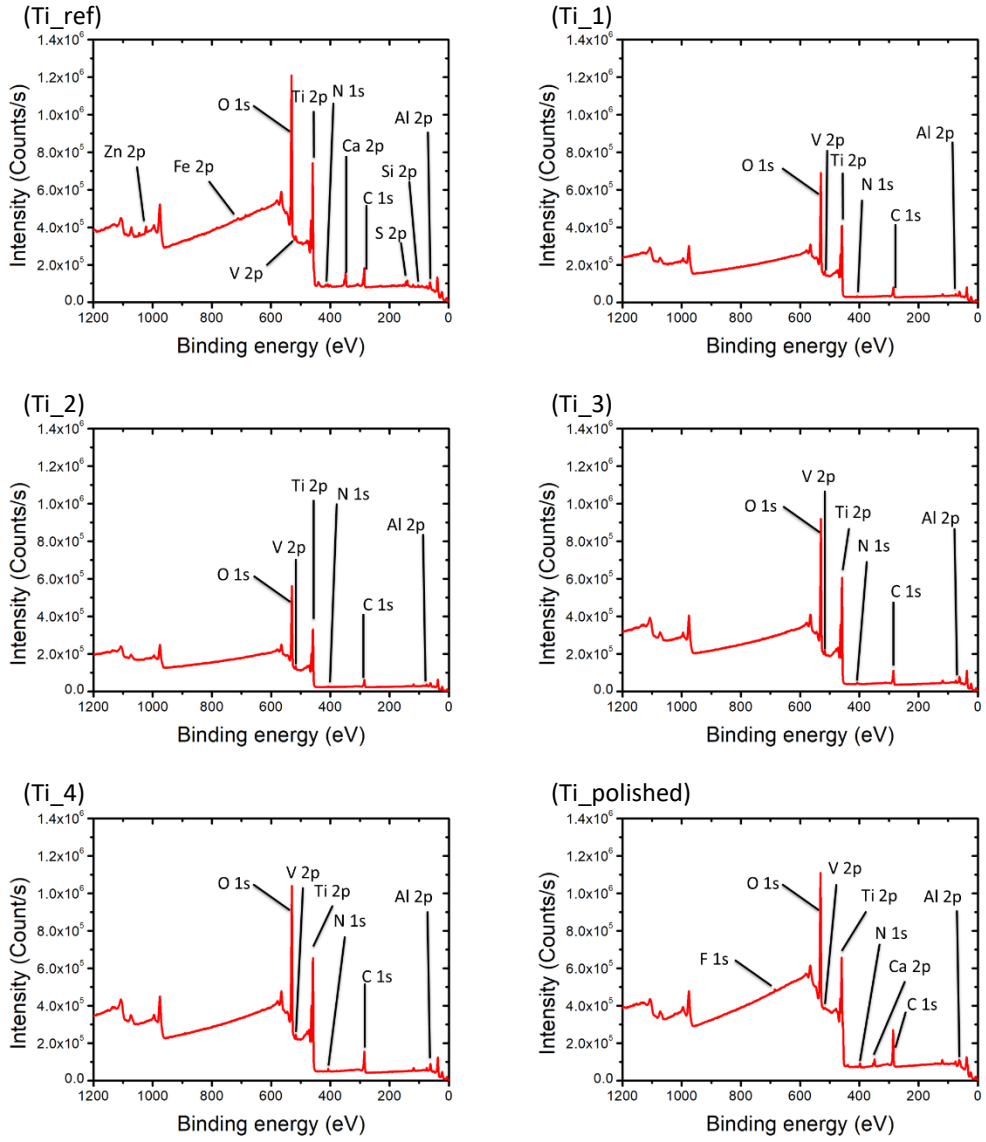

Figure 74: XPS survey spectra of pretreated titanium (pretreatment attributes are indicated in Table 19, §5.4)

To fit the reference, five peaks were used: one C-C/C-H peak set at 284.8 eV, one C-O/C-N peak at 286.5 eV, one CO3 peak at 288.7 eV, one C-F peak at 292.9 eV, and a C-Ti peak at 291.9 eV. For Ti_1, Ti_2, Ti_3 and Ti_4, the same contributions were used to fit the C 1s regions: one C-C/C-H contributions at 284.8 eV, one C-O/C-N contribution at 286.2 eV and a CO3 contribution at 288.9 eV. Additional contribution corresponding to titanium carbide, C-Ti, was added to Ti_polished at 281.6 eV.

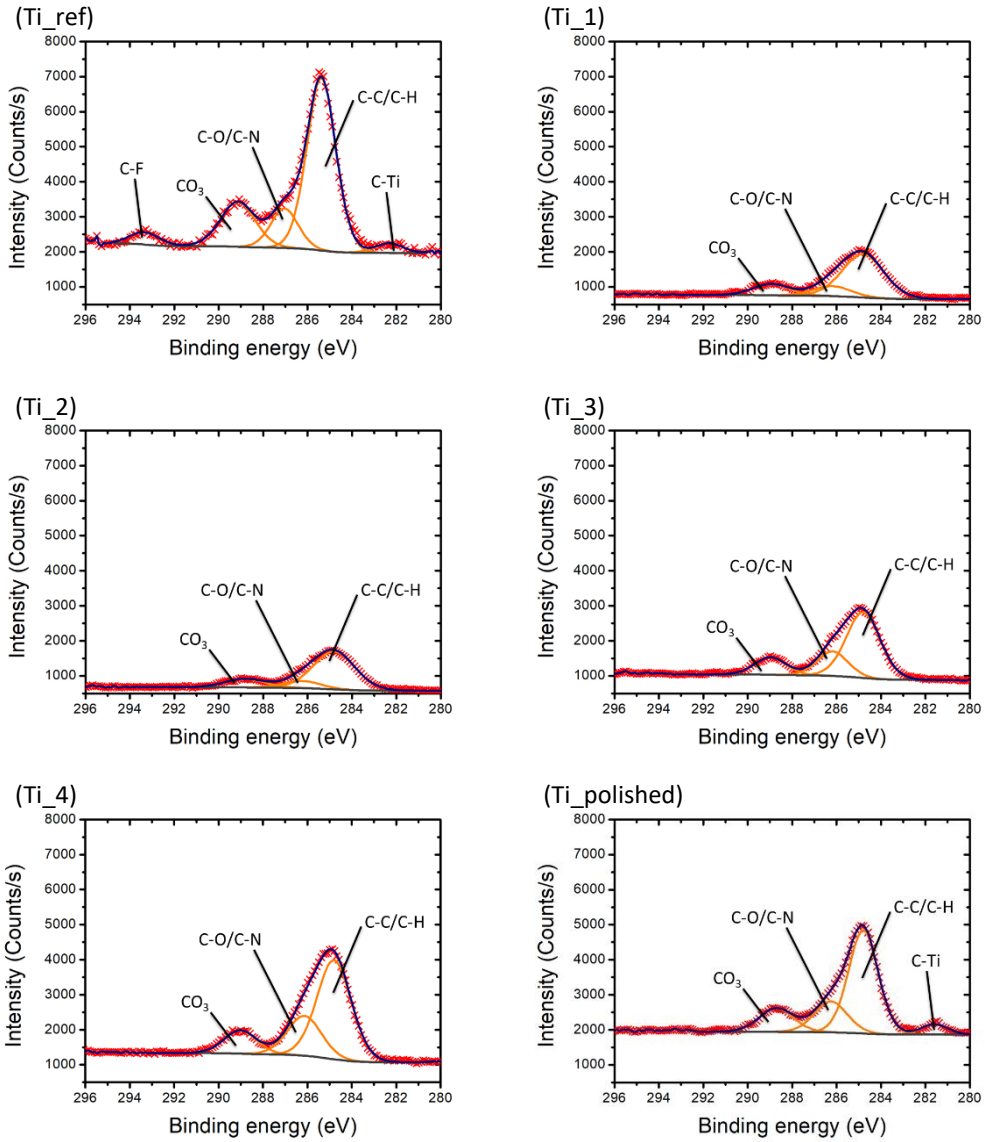

Figure 75: XPS high resolution spectra of the C 1s region for pretreated aluminum (pretreatment attributes are indicated in Table 19, §5.4)

The Ti_ref and the Ti_polished samples were interpreted using nine peaks related to five contributions due to spin-orbit splitting. The first contribution is related to Ti (0) and Ti-C, for the reference at 454.1 eV (Ti 2p3/2) and 460.3 eV (Ti 2p1/2), while the Ti_polished samples present the same contribution at 453.5 eV (Ti 2p1/2) and 459.7 eV (Ti 2p1/2). The second contribution is related to Ti (II) and Ti-N at 455.4 eV and 461.6 eV for Ti_ref, while Ti_polished are at 454.7 eV and 461.1 eV, respectively. The third contribution is related to Ti (III) at 457.5 eV and 463.7 eV, and at 456.9 eV and 432.5 eV respectively for the reference and Ti_5. The fourth contribution is related to Ti (IV) and is found at 459.1 eV and 465.0 eV on the reference, and at 458.5 eV and 464.3 eV on Ti_polished samples. The fifth contribution is related to titanium surface plasmons and is found at 471.7 eV for the reference and at 470.9 eV on Ti_5 samples. For Ti_1 to Ti_4 samples, the same contributions were used, giving five peaks displaying similar bonding energies for all these samples. The first contribution is associated to Ti (III) aroundv457.5 eV (Ti 2p3/2) and around 463.0 eV (Ti 2p1/2). The second contribution is associated to Ti (IV) around 458.6 eV (Ti 2p3/2) and around 464.4 eV (Ti 2p1/2) [291–293]. The third and last contribution is associated to titanium surface plasmons around 471.4 eV.

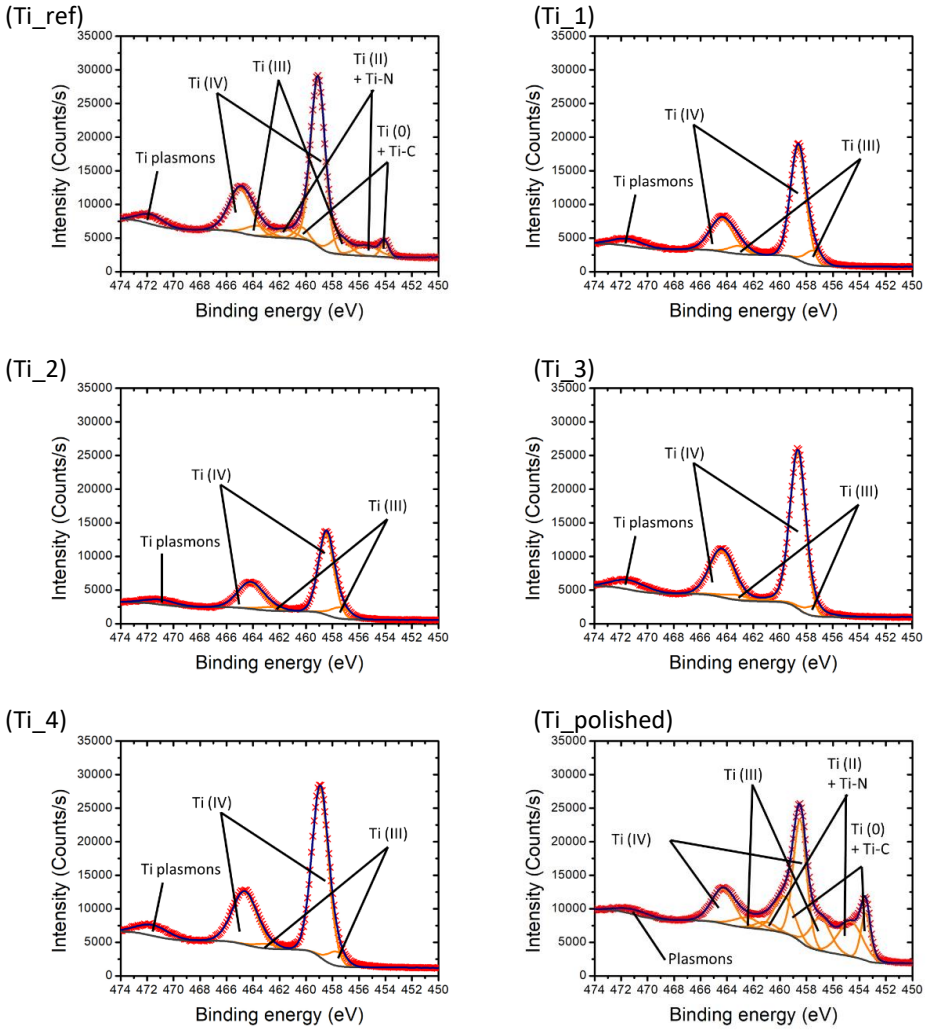

Figure 76: XPS high resolution spectra of the Ti 2p region (pretreatment attributes are indicated in Table 19, §5.4)

Ti_ref and Ti_polished were interpreted using three peaks: one around 530.1 eV related to titanium oxide, and the two others around 531.4 eV and 532.5 eV respectively associated to organic compounds (adventitious carbon), and oxidized aluminum and vanadium. On Ti_1, to Ti_4, only two peaks were used to fit this region: one around 530.2 eV associated to titanium oxide, and one associated to organic compounds as well as oxidized aluminum and vanadium around 532.1 eV.

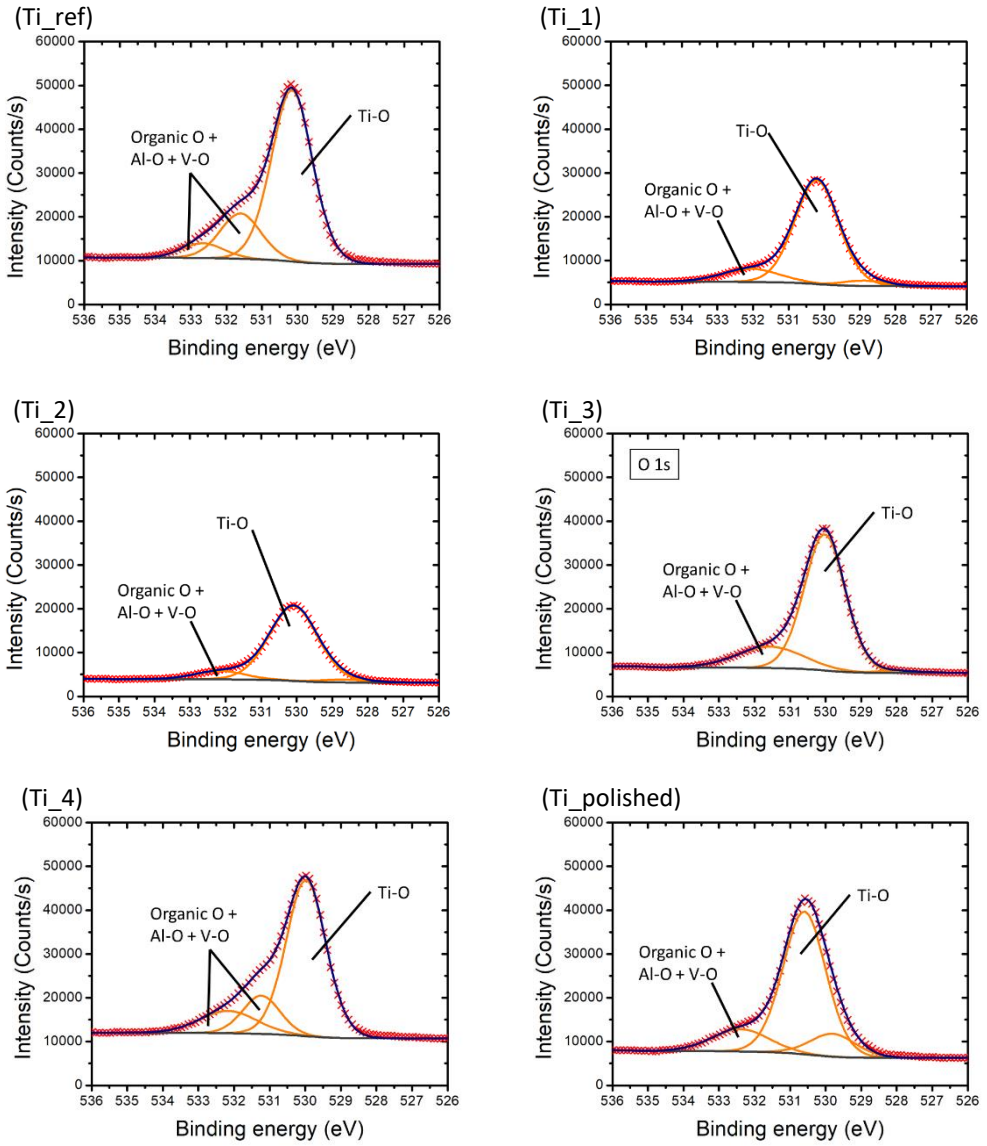

Figure 77: XPS high resolution spectra of the O 1s region (pretreatment attributes are indicated in Table 19, §5.4)

Publication extracts

Excerpts and illustrations in this work were published in the articles mentioned below:

Al-Sayyad, A., Lama, P., Bardon, J., Hirchenhahn, P., Vaudémont, R., Houssiau, L., & Plapper, P. (2020). Laser joining of titanium alloy to polyamide: influence of process parameters on the joint strength and quality. International Journal of Advanced Manufacturing Technology, 107, 2917–2925.

Al-Sayyad, A., Lama, P., Bardon, J., Hirchenhahn, P., Vaudémont, R., Houssiau, L., & Plapper, P. (2020). Laser Welding of Titanium Alloy Ti64 to Polyamide 6.6: Effects of Welding Parameters on Temperature Profile Evolution. International Journal of Materials and Metallurgical Engineering, 14(4), 113-116.

Al-Sayyad, A., Bardon, J., Hirchenhahn, P., Vaudémont, R., Houssiau, L., & Plapper, P. (2019). Influence of Aluminum Laser Ablation on Interfacial Thermal Transfer and Joint Quality of Laser Welded Aluminum–Polyamide Assemblies. Coatings, 9(11), 768.

Al-Sayyad, A., Bardon, J., Hirchenhahn, P., Santos, K., Houssiau, L., & Plapper, P. (2018). Aluminum pretreatment by a laser ablation process: influence of processing parameters on the joint strength of laser welded aluminum–polyamide assemblies. Procedia CIRP, 74, 495-499.

Al Sayyad, A., Bardon, J., Hirchenhahn, P., Mertz, G., Haouari, C., Laurent, H., & Plapper, P. (2017). Influence of laser ablation and plasma surface treatment on the joint strength of laser welded aluminum-polyamide assemblies. Proceedings of the JNPLI 2017, Strasbourg, France, 13–14 September 2017.

List of figures

List of tables

List of equations

List of abbreviations

LFA	Laser Flash Analysis
TCR	Thermal Contact Resistance
CMY	Cooper–Mikic–Yovanovich
PPP	Peak Pulse Power
OL	Overlap ratio
CW	Continues Wave
LAMP	Laser assisted metal – polymer joining
OFAT	One Factor at A Time
DoE	Design of Experiments
CCD	Central Composite Design
FCD	Face Centered Design
ANOVA	Analysis of Varience
RSM	Response Surface Method
SEM	Scanning Electron Microscope
EDX	Energy Dispersive X-ray spectrometer
XPS	X-ray photoelectron spectroscopy
ToF-SIMS	Time-of-Flight Secondary Ion Mass Spectrometry
PCA	Principle Components Analysis
DSC	Differential scanning calorimetry
DBD	Dielectric Barrier Discharge
OWRK	Owens–Wendt–Rabel–Kaelble
SE	Surface Energy
IR	Infrared
Al1050	Aluminum 1050
Ti64	Titanium-6% aluminum-4% vanadium
PA6.6	Polyamide 6.6
OM	Optical Microscopy
MI	Macroscopic Investigations

List of symbols

σ_{sg}	surface free energy (mN/m)
σ_{sl}	interfacial tension (mN/m)
σ_{lg}	liquid surface tension (N/m)
θ	contact angle (°)
σ	effective root mean square roughness (μm)
m	effective mean asperity slope
k_h	harmonic mean thermal conductivity (W/mK)
H	hardness of the softer material (MPa)
P	applied pressure (MPa)
P_{peak}	peak power (W)
P_{avg}	average power (W)
T_p	pulse modulation time (s)
$f_p = 1/T$	pulse modulation frequency (Hz)
a	wobble amplitude (mm)
a	CCD coded distance from design center to axial star
λ	wobble distance parameter
f	wobble frequency (Hz)
v_f	feed rate (mm/s)
P_{avg}	average power (W)
T_{pulse}	pulse duration (s)
f_p	pulse frequency (Hz)
V	beam speed (mm/s)
$\emptyset$	beam diameter (mm)
f_p	pulse frequency (Hz)
σ_{sg}^{d}	dispersive part of solid surface energy (mN/m)
σ_{lg}^{d}	dispersive part of liquid surface energy (mN/m)
σ_{sg}^{p}	polar part of solid surface energy (mN/m)
σ_{lg}^{p}	polar part of liquid surface energy (mN/m)
a_{diff}	thermal diffusivity (m^2/s)
d	sample thickness (m)

$t_{1/2}$	half time (s)
λ_{cond}	thermal conductivity (W/m·K)
a_{diff}	thermal diffusivity (m^2/s)
c_P	specific heat (J/kg·K)
ρ	density (kg/m^3)
P	laser power (W)
f	focal position (mm)
V	Beam speed (mm/s)
Al	aluminum plasma pretreatment time (s)
PA	polyamide plasma pretreatment time (s)